Downloaded from orbit.dtu.dk on: May 05, 2023

DTU Library

On Practical Sampling of Bidirectional Reflectance

Nielsen, Jannik Boll

Publication date:
2016

Document Version
Publisher's PDF, also known as Version of record

Link back to DTU Orbit

Citation (APA):
Nielsen, J. B. (2016). *On Practical Sampling of Bidirectional Reflectance*. Technical University of Denmark. DTU Compute PHD-2016 No. 435

General rights
Copyright and moral rights for the publications made accessible in the public portal are retained by the authors and/or other copyright owners and it is a condition of accessing publications that users recognise and abide by the legal requirements associated with these rights.

- Users may download and print one copy of any publication from the public portal for the purpose of private study or research.
- You may not further distribute the material or use it for any profit-making activity or commercial gain
- You may freely distribute the URL identifying the publication in the public portal

If you believe that this document breaches copyright please contact us providing details, and we will remove access to the work immediately and investigate your claim.

On Practical Sampling of Bidirectional Reflectance

Jannik Boll Nielsen

Kongens Lyngby 2016
PhD-2016-435

Technical University of Denmark
Department of Applied Mathematics and Computer Science
Richard Petersens Plads, building 324,
2800 Kongens Lyngby, Denmark
Phone +45 4525 3031
compute@compute.dtu.dk
www.compute.dtu.dk

PhD-2016-435
ISSN: 0909-3192

Summary (English)

Accurate material models are a key part in producing convincing, photo-realistic, images in computer graphics. Elaborate analytical models exist, allowing graphics designers to manually *design* material appearance. However, given the complex nature and wide variability of material appearance, *measuring* this from the real world is an impractical and time-consuming process. Having a practical way of measuring material appearance will not only be of great value to the graphics community, but also open up for a wide range of new application areas, including industrial production quality control, digital prototyping and manufacturing, and interactive real-time product visualization.

In this thesis, the challenge of making material appearance measurements practical is addressed. Specifically, the Bidirectional Reflectance Distribution Function (BRDF), which is the quantity describing material appearance, is thoroughly analysed using both optimisation tools and multivariate statistics, in search of making BRDFs more accessible.

The work demonstrated includes an insight into the challenges of fitting analytical models to measured data and on the compromises one is bound to make when simplifying the real world with a parametric BRDF model. Specifically we identify what error measures work well for obtaining perceputally good results and how a simple BRDF model may be modified to better match real world data. With an offset in this, a linear, data-driven, BRDF model is proposed and a framework for reconstructing full and accurate BRDFs from only a few measurements is presented. It is here demonstrated that with as little as 20 point-samples, a BRDF can accurately be reconstructed. Furthermore utilising the field of view of a camera, this may be reduced to as little as two images. With

this, the thesis demonstrates how BRDF measurements can be made practical, and it exemplifies this with a range of datasets intended for various purposes, each including high quality measured BRDFs.

Where the classical approach to BRDF capture may take weeks in measurement time, we here successfully demonstrate that is can in fact be reduced to no more than minutes or even seconds using our framework.

Summary (Danish)

Nøjagtige materialemodeller er et vigtigt led i at kunne producere overbevisende og fotorealistiske billeder med computer grafik. Omfattende analytiske modeller eksisterer, som giver grafiske designere mulighed for at *designe* materiale udseende. Desværre, givet materialeudseenders komplekse natur og store variation, er det derimod i dag både en upraktisk og langsommelig proces at *måle* disse. Kunne man finde en praktisk måde at måle materiale udseende på ville dette have stor værdi, ikke alene for grafikere, men det vil også åbne op for en lang række af nye anvendelsesområder, heriblandt kvalitetskontrol i industriel produktion, digital prototyping og manufacturing, samt real-time produkt visualisering.

I denne afhandling adresseres udfordringen i at lave måling af materiale udseende praktisk. Specifikt analyseres "the Bidirectional Reflectance Distribution Function" (BRDF'en), som er den størrelse der beskriver materialeudseende, ved brug af optimeringsværktøjer og multivariat statistik, i håb om at gøre BRDF'er mere tilgængelige.

Det præsenterede arbejde inkluderer en indsigt i udfordringerne i at fitte analytiske modeller til målte data og i de kompromiser man er tvunget til at indgå når den virkelige verden simplificeres ved en parametrisk model. Specifikt identificerer vi hvilke fejlmål der virker godt til at opnå perceptuelt gode resultater and hvordan man kan modificere en simpel BRDF model til bedre at matche virkelige data. Med dette som udgangspunkt præsenterer vi en lineær, datadrevet, BRDF model, samt et framework til at rekonstruere fulde og nøjagtige BRDF'er fra et meget lille antal målinger. I denne sammenhæng demonstrerer vi at så lidt som 20 punktmålinger er nok til at en BRDF kan blive korrekt rekonstrueret. Ydermere demonstrerer vi at hvis et kameras fulde synsfelt udnyttes kan

antallet af målinger reduceres til så lidt som 2 billeder. Hermed demonstrerer afhandlingen hvordan BRDF målinger kan gøres praktiske og dette eksemplificeres med en række datasæt tiltænkt forskellige formål, hvert indeholdende målte BRDF'er af høj kvalitet.

Hvor den klassiske tilgang til måling af BRDF'er kan tage uger i måletid, demonstreres her succesfuldt at denne måletid faktisk kan reduceres til så lidt som minutter eller endda sekunder via vores framework.

Preface

This thesis was prepared at the Image Analysis and Computer Graphics Section at Department of Applied Mathematics and Computer Science at the Technical University of Denmark (DTU). It was done in fulfilment of the requirements for obtaining a doctor of philosophy degree (Ph.D.) within the topic of computer graphics.

The work presented in this thesis was funded by DTU Compute.

The thesis presents research on the challenge of accurately measuring material appearance in practice. Given the practical nature of this challenge, a substantial amount of experimental work has laid the foundation of the primarily theoretical results presented in this thesis. A range of publications was made during the course of this project, summarised on page xiii. From these, 6 have been attached in appendices A-F. In addition to the papers closely connected to the topic of this project, a handful of additional publications were made touching upon more or less unrelated topics. We annually have a technology showcase day in the Image Analysis & Computer Graphics section at the Technical University of Denmark, and leading up to this day we usually have a "Hackathon" where Ph.D. students get together and produce a technology demonstrator. We have made it into a tradition to make publications out of these demonstrators and the contributions not included in this thesis are a result of this.

The project has been supervised by Associate Professor Henrik Aanæs and co-supervised by Associate Professor Jeppe Revall Frisvad and Professor Knut Conradsen. The research has been carried out at DTU, but external research was conducted under supervision of Professors Ravi Ramamoorthi and Henrik Wann Jensen at the Computer Graphics Lab in the Department of Computer Science

and Engineering at the University of California, San Diego.

Lyngby, 06-October-2016

Jannik Boll Nielsen

Acknowledgements

First of all I would like to thank my three supervisors, Henrik Aanæs, Jeppe Revall Frisvad, and Knut Conradsen, who have each contributed in their very own way with valuable and motivational guidance during the course of this project. Specifically I would like to thank Henrik for our long strategical talks, Jeppe for our deep technical discussions, and Knut for our motivational discussions both within and beyond relevant topics. Moreover, I would like to thank my collaborators in the Computer Graphics Lab at UCSD, Ravi Ramamoorthi and Henrik Wann Jensen for their hospitality and interest in my research.

I would also like to thank DTU Compute for sponsoring my work with their scholarship, and in relation to that, thank Rasmus Paulsen for coming up with a year full of research-projects while waiting for the scholarship.

Of course a great thanks goes to my partners in crime and office mates, Eythor Runar Eirikson, Jonathan Dyssel Stets, and Jakob Wilm. Thanks for all our fruitful discussions, our coffee runs, our goofing around, and of course your continuous support. Likewise, a big thanks to the rest of the coffee crew and Ph.D. colleagues, both old and new. It is always a pleasure to share thoughts and ideas with you.

Finally, a big thanks to my loving family, without whom this thesis would have been done a quarter of a year earlier.

Contents

List of Contributions

Peer reviewed

Contribution C.I: ..... **Jannik Boll Nielsen**, Jeppe Revall Frisvad, Knut Conradsen, and Henrik Aanæs. Addressing grazing angle reflections in Phong models. In *SIGGRAPH Asia 2014 Posters*, page 43. ACM, 2014. [NFCA14]

Contribution C.II: ..... **Jannik Boll Nielsen**, Eythor Runar Eiriksson, Rasmus Lynbgy Kristensen, Jakob Wilm, Jeppe Revall Frisvad, Knut Conradsen, and Henrik Aanæs. Quality assurance based on descriptive and parsimonious appearance models. In *Proceedings of the Third Workshop on Material Appearance Modeling: Issues and Acquisition*, MAM '15, pages 21–24. Eurographics Association, 2015. [NEK+15]

Contribution C.III: .... Henrik Aanæs, Knut Conradsen, Alessandro Dal Corso, Anders Bjorholm Dahl, Alessio Del Bue, Mads Doest, Jeppe Revall Frisvad, Sebastian Hoppe Nesgaard Jensen, **Jannik Boll Nielsen**, and Jonathan Dyssel Stets. Our 3D vision data-sets in the making. In *The Future of Datasets in Vision 2015*, *CVPR 2015 Workshop*, 2015. [ACDC+15]

Contribution C.IV: .... **Jannik Boll Nielsen**, Henrik Wann Jensen, and Ravi Ramamoorthi. On optimal, minimal BRDF sampling for reflectance acquisition. *ACM Transactions on Graphics (Proceedings of SIGGRAPH Asia 2015)*, 34(6):186, 2015. [NJR15]

Contribution C.V: ..... Rasmus Ramsbøl Jensen, **Jannik Boll Nielsen**, Rasmus Larsen, and Rasmus Paulsen. Anatomically correct surface recovery: A statistical approach. In *Scandinavian Conference on Image Analysis*, pages 212–223. Springer International Publishing, 2015. [JNLP15]

Contribution C.VI: .... Zexiang Xu, **Jannik Boll Nielsen**, Jiyang Yu, Henrik Wann Jensen, and Ravi Ramamoorthi. Minimal BRDF sampling for two-shot near-field reflectance acquisition. *ACM Transactions on Graphics (Proceedings of SIGGRAPH Asia 2016)*, 35(6), 2016. To appear. [XNY+16]

Publications not included in this thesis:

Contribution C.VII: ... Morten Nobel-Jørgensen, **Jannik Boll Nielsen**, Anders Boesen Lindbo Larsen, Mikkel Damgaard Olsen, Jeppe Revall Frisvad, and J. Andreas Bærentzen. Pond of illusion: interacting through mixed reality. In *SIGGRAPH Asia 2013 Posters*, page 26. ACM, 2013. [NJNL+13]

Contribution C.VIII: .. Alessandro Dal Corso, Mikkel Damgaard Olsen, Kasper Hornbak Steenstrup, Jakob Wilm, Sebastian Jensen, Rasmus Reinhold Paulsen, Eythor Eiríksson, **Jannik Boll Nielsen**, Jeppe Revall Frisvad, Gudmundur Einarsson, and Hans Martin Kjer. Virtualtable: a projection augmented reality game. In *SIGGRAPH Asia 2015 Posters*, page 40. ACM, 2015. [DCOS+15]

Contribution C.IX: .... Rasmus Ramsbøl Jensen and **Jannik Boll Nielsen**. Atomic stretch: Optimally bounded real-time stretching and beyond. *In SIGGRAPH Asia 2016 Posters*. ACM, 2016. To appear. [JN16]

Publications under preparation

Contribution C.X: ..... Jonathan Dyssel Stets, Alessandro Dal Corso, **Jannik Boll Nielsen**, Rasmus Ahrenkiel Lyngby, Sebastian Hoppe Nesgaard Jensen, Jakob Wilm, Mads Emil Brix Doest, Carsten Gundlach, Eythor Runar Eiriksson, Knut Conradsen, Anders Bjorholm Dahl, Jakob Andreas Bærentzen, Jeppe Revall Frisvad, and Henrik Aanæs. Digitizing scenes with glass objects. *Peer reviewed journal TBA*, 2016. Not yet published. [SCN+16]

List of Symbols

Symbol	[Unit]	Description.
Φ	$[W]$	Radiant flux.
I	$[\frac{W}{sr}]$	Radiant intensity.
E	$[\frac{W}{m^2}]$	Irradiance.
L	$[\frac{W}{m^2 \cdot sr}]$	Radiance.
ω	$[sr]$	Solid angle.
$\boldsymbol{\omega}$	$[1]$	A direction vector in 3D space.
$\boldsymbol{n}$	$[1]$	Normal vector.
$\boldsymbol{h}$	$[1]$	Half vector.
θ	[rad]	Polar/inclination angle.
ϕ	[rad]	Azimuthal angle.
ρ	$[1]$	Reflectance, directional.
f_r	$[sr^{-1}]$	Bidirectional Reflectance Distribution Function (BRDF).

Chapter 1

Introduction

1.1 Scope

This thesis focuses on finding a methodology for developing new low parameter models for the radiometric appearance of physical objects that better correspond to the real world. The goal is to enable practical measurement of reflectance by reducing the number of measurements needed for accurate data-fitting. Contributing to solving these challenges, enables new industrially very relevant applications of computer graphics within e.g.

- Digital prototyping & manufacturing
- Interactive real-time product visualisation
- Film & gaming industry
- Industrial quality control

As there is quite a gap between the art of measuring reflectance, including building the equipment to do so, and modelling reflectance mathematically, this project has indeed had a multidisciplinary nature. Primarily the scientific contributions included here focus on the theoretical and mathematical parts of our

Figure 1.1: Computer graphics are capable of producing impressive photorealistic content. Unfortunately the cost makes it prohibitive for all but the most high profile applications. *Images courtesy of Walt Disney Pictures, Arnaud Servouze, and 20th Century Fox.*

work, and only between the lines is the practical work mentioned. In truth, a major part of the work carried out in this thesis has revolved around creating a laboratory facility at DTU Compute capable of accurately measuring material reflectance and in particular Bidirectional Reflectance Distribution functions (BRDFs). This work is not directly mentioned and only appendices G-H include technical notes on the equipment created, however, these have not been published elsewhere. As such it is worth acknowledging an important part that is often forgotten, namely that most often it takes more time to experimentally validate your models than it took to derive them in the first place.

Before continuing, let us make a note on our nomenclature. In this thesis, we use the terms "BRDF" and "appearance" interchangeably since the BRDF, although not solely, contributes to a major part of how materials appear to the human eye. Also, when we talk about "sampling a BRDF" in this thesis we talk about making individual measurements of the 4D manifold constituting a BRDF. This should not be confused with "importance sampling a BRDF" in rendering, where a probability distribution linked to the BRDF is used to randomly pick a ray direction in a path tracing.

1.2 Motivation

Today the realism of digitally simulated films and computer games is awe inspiring, to the degree that it is difficult to distinguish from reality. This is in part possible due to very elaborate computer models of the content displayed, such as people, furniture, trees, and cars. Producing such content is today mostly a manual process, which makes the cost prohibitive for all but the most high profile applications, see figure 1.1. A main reason for this cost is the man-

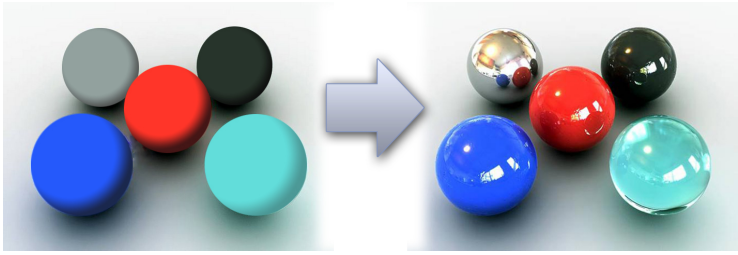

Figure 1.2: The difference between simple (left) and complex (right) radiometric models. Today, only simple radiometric features are modeled from measurements of real life objects. In order to obtain more realistic digital representations (right), better statistical methods of parameterizing the radiometric properties must be invented.

ual modelling of the radiometric properties, whereas good methods exist for automatically generating the geometric models, e.g. via structured light scanners [Aan03, ADSP12]. Off the shelf full appearance digitalization pipelines, capturing both geometry and radiometry, limit themselves to very simple radiometric models. Often these are simply Lambertian or at most simple isotropic Phong or Ward models. As conceptualised in figure 1.2, we wish to improve this by pushing the practical models closer to the photorealistic models used in the high-profile applications.

In this project, we seek to automate the radiometric modelling by applying advanced statistical methods to images of real world objects. The goal is to enable digital artists to sample the true radiometric properties of real word objects and transfer these to the already existing highly detailed geometric models of the respective objects. The automatic sampling of the visual behaviour, i.e. the radiometric properties, will thus finalise the automatic pipeline between real world objects and photorealistic digital representations of these. A tool much needed within the advancing field of digital prototyping. The intended impact of this project is to bring down the cost of photorealistic computer graphics to a point where even small productions will be able to use it and hereby bring such modelling work back to Denmark from low wage countries. Just as important, it will also allow for the proliferation of these techniques beyond the film and gaming industry. Finally, and most importantly, practical material appearance acquisition is an important step in the current trend of automation and data exchange in manufacturing technologies (Industry 4.0). If we are to realise cyber-physical systems with virtual copies of real-world objects, there is no way around capturing appearance in a practical way.

To motivate the project further, we will in the following present three concrete

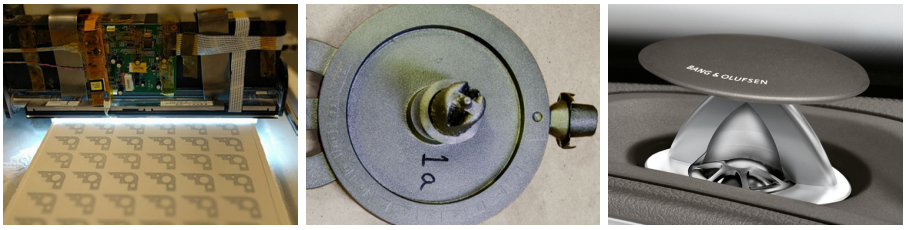

(a) 3D printing **(b)** Production **(c)** Prototyping

Figure 1.3: Left: Additive manufacturing process (3D printing) using a powder-based system, *image from [PEAH16]*. Center: Casting with surface roughness. Right: Prototyping of Bang & Olufsen treble, *image courtesy of B&O*.

industrial areas where current methods fail to suffice and more practical radiometric models are in demand. The cases presented here are only a few examples of a broad range of application areas that we have identified. Additional areas are pointed out in publication C.II, and beyond that, even more, have become apparent to us via industrial collaborations carried out in the duration of this project and some still ongoing.

Case 1: Additive Manufacturing

An area where this project has a significant relevance is within the field of additive manufacturing, i.e. the physical realisation of digital 3D models. First of all, by providing better techniques for acquiring reflectance properties of printing materials. These measured properties can be applied to an arbitrary geometry and lighting configuration thereby enabling appearance prediction for the given materials. This is in itself a valuable asset as it can still take several hours to fully print a 3D model. Currently, only the processed CAD model is visualised as a prediction of print result and only very recently has work been made in estimating the colour transformations occurring during the printing process [EPA15]. Secondly, the process of 3D printing is a delicate process often relying on heating or curing. The radiometric properties of the printed surface are one mean of identifying failures during printing such as color-changes due to overheating or surface-normal changes due to structural collapses, see figure 1.3a. Potentially, automatic radiometric inspection could be added as a feedback loop to provide a new kind of control of 3D printers. This would to a great extent aid in avoiding failed 3D prints, that due to the slow print-speed can be a costly affair. For printing aimed at industrial use, a thorough CT-like radiometric inspection of the inside structure of a printed subject will further be

able to contribute as quality assurance. This is achievable by capturing every single layer during the print process and is as such a modality unique to 3D printing and may serve as another layer of quality documentation.

Case 2: Classical Production

As with additive manufacturing, quality control in more classical kinds of production is of great importance, where a consistent quality over enormous batches has to be ensured. Such quality control is mainly done through visual inspection by manual labour today, making it a costly affair and for grand scale productions impossible to perform on a per item level.
Within injection moulding, there is a range of factors affecting the result. Depending on e.g. pressure/injection speed, heating, or material purity, moulding defects such as blisters, burn marks or colour streaks may occur, generally resulting in full batches being discarded. These effects are all linked to the (spatially varying) radiometric properties of the material, making automated rapid reflectance acquisition highly relevant. Likewise, the field of metal casting deals with castings where their surface roughness is dependent on a range of factors involved in the casting process such as e.g. temperature and material composition, see figure 1.3b. In many cases surface roughness causes a need for post-machining of said surfaces making it an unattractive feature and often a direct quality measure. This roughness also affects the visual appearance of a surface, and being able to quantify it automatically using radiometry is therefore of great interest in the casting industry. In both scenarios, rapid appearance acquisition thus has the potential of automating quality control, which is currently a very labour intensive process.

Case 3: Digital Prototyping

Finally, a third major impact of accurate practical radiometric models are their predictive powers of future products in a digital manufacturing pipeline, i.e. visualising how a product will look before it is produced. Resource efficient product design is extremely important in Denmark due to high wages, meaning that new means of accurately digitising materials are required. Examples of applications where this will be relevant include the digital prototyping of LEGO products, predicting the appearance of a metallic finish of B&O Hi-Fi systems (figure 1.3c), and faithfully modelling of dentures by 3Shape. As for the latter case, it is today impossible to realistically reproduce how a given patient's teeth will look with different types of dentures installed. This makes it challenging for the dentist to choose the best material tone for a bridge or a

crown when weighing price against appearance together with the customer. As for the two former, the current iterative design-process is both costly and slow, since a range of prototypes has to be produced during development. Especially in luxury products, the visual aspect is important, and in order to transfer to this design-process to a simulated environment, with digital prototypes, very accurate radiometric material models are required. In addition, by practical acquisition of reflectance functions for the different materials that a designer can typically choose between, the digital design process becomes more efficient. One could instantiate a feedback loop where designers ask for specific reflectance properties and surface engineers try to develop it and measure the new BRDF for every iteration.

1.3 Methodolgy

The way we have approached this problem is by utilising our unique image capturing experimental facility, built around a six-axis industrial robot, to capture vast images of relevant real world objects [ADSP12]. This utility provides us with a unique possibility to acquire a data set of sufficient size, diversity, and quality. Ensuring a practical focus of the project, we primarily focused on materials used in industrial production, such as plastics and metallic finishing. These materials span the problem well, and will allow us to address specific problems in digital manufacturing. The project has been designed to follow a two-stage approach, where we will first investigate a model fitting pipeline for fitting the commonly used radiometric models to captured data, i.e. images. This allows us to do an automatic radiometric modelling, giving an initial solution to the problem.
The second and main stage of the project is the investigation into construction of new radiometric models. The radiometric models mostly used for photorealistic computer graphics, model the scattering of light beneath the surface of the material. The paths of light through a scattering material are typically represented as manifolds in high dimensional spaces [FCJ07, FCJ12, JM12]. This implies that these models are computationally complex and therefore impractical to estimate due to the very large number of observations that would be required. Here, we propose capturing the radiometric properties of materials, via our lab equipment, and subsequently, fit low-dimensional approximations to them. This will enable radiometry acquisition based on a few high-quality images.
The work in the proposed project requires efforts within the fields of computer vision, computer graphics, optimisation, and statistical model selection and fitting. Hence, we are dealing with a very multidisciplinary challenge.

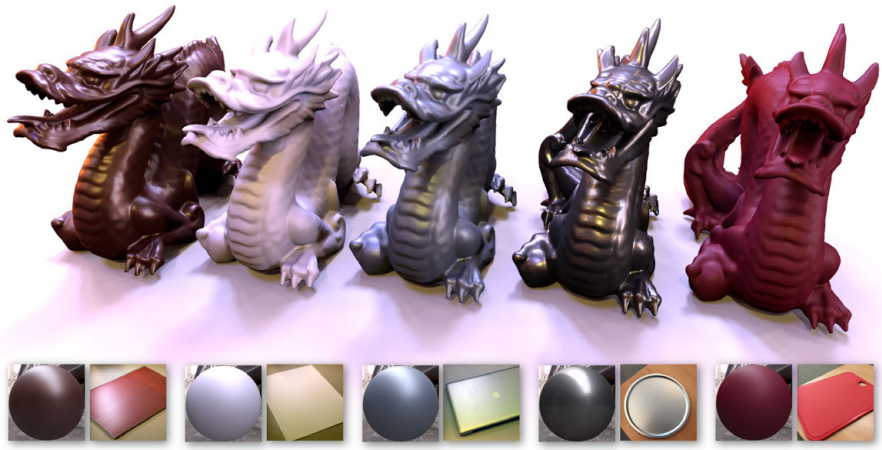

Figure 1.4: Achieved goal of this thesis: Devising a practical BRDF model allowing fast appearance acquisition and digitisation of new materials.

1.4 Thesis Outcome

The research carried out during the 3 years of this Ph.D. study has granted a great insight into the realm of material appearance and computer graphics. Specifically, it has resulted in the development of a lab-facility capable of densely measuring BRDFs and produced the know-how associated with such a facility. We believe this is the first of its kind in Denmark and as such provides Danish industry with a tool in high demand.

From an academic point of view, this thesis has resulted in a range of publications. These publications are listed on page xiii. The contributions most relevant have been included in the appendices. These publications revolve around the challenge of practically measuring BRDFs and follow the methodology outlined above. In particular, papers C.IV and C.VI to a great extent succeed in achieving this by demonstrating a practical model and a minimal sampling scheme, allowing fast and precise radiometric measurements. Figure 1.4 shows a few examples of the results obtained in these papers.

1.5 Thesis Outline

The thesis has been divided into 3 major chapters, Chapter 2: Background, Chapter 3: Related Work, and Chapter 4: Contributions.
In Chapter 2, we set the stage by presenting our use of notation and defining necessary quantities related to radiometry and material appearance. In the sake of brevity, this chapter will not repeat theory presented in the attached publications. Nor will common mathematical or statistical tools be derived.
In chapter 3, we cover related work that has set the base of this thesis. In addition, we elaborate on what alternative approaches to our methods have been proposed, and finally, we touch upon what recent advances have been made while the work in this thesis was carried out.
Finally and most importantly, chapter 4 presents and explains the contributions made in this thesis.

In addition to formal chapters, a range of appendices have too been included in this thesis. These appendices include relevant publications as well as a set of technical notes made during the project, addressing a range of relevant problems.

Chapter 2

Background

The Bidirectional Reflectance Distribution Function, or BRDF, characterises what we humans would describe as "surface appearance" or simply, a "material". I.e. it is the function that describes objects' colours and appearance characteristics such as highlights or lack thereof. This function is of paramount importance when digitally reproducing the world through computer graphics, and without, the world of computer graphics would indeed be a dull world! To humans it gives an indication of surface characteristics: before even touching an object, through the BRDF, we predict the smooth surface of a brushed silvery MacBook, the hard feel of a ceramic cup, or the slimy surface of a wet fish. Evidently, the BRDF holds a great amount of information, and as such, having the ability to both quantize and decipher a BRDF is an important tool in understanding our world.
Formally the BRDF relates the physical units of emitted and received light. We will return to its precise definition later in this chapter, but before this, we will set the stage and define relevant quantities and relations. With the definition of the BRDF, we will further touch upon relevant topics related to the BRDF, such as popular existing analytical BRDF models and how to measure BRDFs. To this extent, this chapter seeks to cover, not all, but the relevant theory related to the topic of this thesis, namely *practical sampling of bidirectional reflectance*.

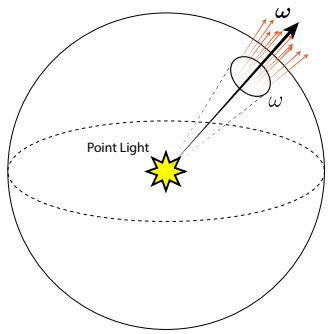

Figure 2.1: Point light source radiating energy uniformly in a sphere. For a given direction, $\boldsymbol{\omega}$, The amount of radiant flux traveling through the infinitesimal solid angle ω, per unit solid angle, equals the radiant intensity.

2.1 Radiometry

As a starting point, we will consider in an ideal point light source, i.e. an infinitesimal point radiating electromagnetic energy uniformly in all directions. The power emanating from this is called the *radiant flux*, or *radiant power*, Φ, and is measured in Watts $[W]$, i.e. Joules per second.
By definition, the energy of a point light source emanates equally in all directions. But because we usually deal with objects in *relation* to a light source, and we usually deal with light sources that are not ideal point sources, it makes sense to describe the amount of energy going in a certain direction. In this case, we define the *radiant intensity* as the amount of radiant flux moving through an infinitesimal solid angle, ω, spanned around a given direction, that is, radiant flux per solid angle:

$$I = \frac{d\Phi}{d\omega} \quad \left[\frac{W}{sr}\right] \tag{2.1}$$

We visualize this in figure 2.1, where the direction is denoted by $\boldsymbol{\omega}$.

2.1.1 Irradiance and Radiance

Alternatively, rather than following the light along a specific ray, we may instead observe a surface illuminated by the point light source. In this scenario, the term characterising the flux incident on the surface is called the *irradiance*, E, and is

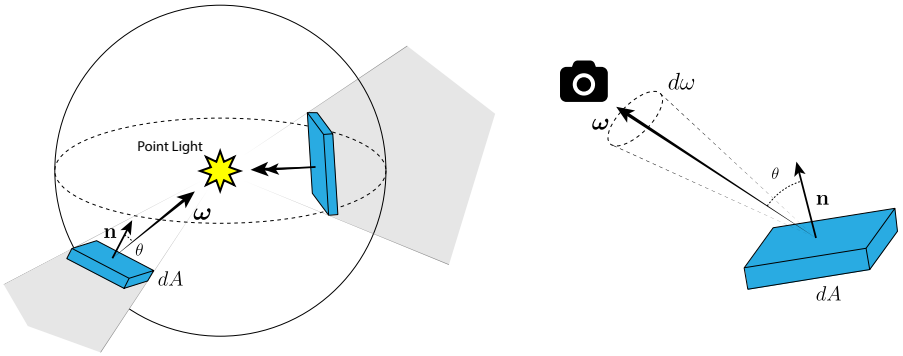

Figure 2.2: Left: Geometries concerning irradiance. Position and orientation of a surface affects the amount of radiant power received by the surface. Right: Geometries concerning radiance. Here, variabilities like distance and incidence angle are being compensated for.

defined as flux per unit area:

$$E = \frac{d\Phi}{dA} \quad \left[\frac{W}{m^2}\right] \tag{2.2}$$

Suppose we consider an isotropic point light. At the distance r from the source, the flux emitted by the source will be distributed across a spherical surface area with radius r. As a result, irradiance due to a point source is inversely proportional to the square of the distance to the source. Tilting a surface away from the light source means that the flux will be distributed over an even larger surface area. Thus, irradiance is in general proportional to the cosine between surface normal and light direction. We illustrate this in the left part of figure 2.2 where two different surfaces receive different amounts of power from the light source due to their distance and orientation relative to the light.

Conversely, we may look at the light leaving a surface. This phenomenon is described by the quantity *radiance*, L. Taking the observer of a surface as the point of reference, the radiance is defined as the flux received per solid angle, per projected surface area:

$$L = \frac{d^2\Phi}{dA_{proj}\, d\omega} = \frac{d^2\Phi}{dA \cos\theta \; d\omega} \quad \left[\frac{W}{m^2 \cdot sr}\right] \tag{2.3}$$

where θ is the angle between the surface normal and direction to the observer. This definition makes good sense considering the radiant flux received by a camera imaging a surface: First, the received power should be normalised by the solid angle covered by the aperture of the camera (ω). The greater the aperture, the higher the power, but a measurement should not be affected by

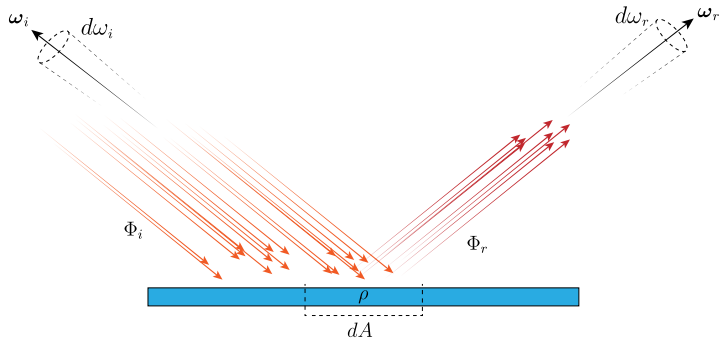

Figure 2.3: Directional reflectance, ρ, determines the fraction of flux reflected off a surface.

the choice of aperture or how close it is to the sample. Secondly, depending on whether you observe a surface from an oblique angle or from a grazing angle, an element on the surface will cover more or less of your view, neither should the measurement be affected by the choice of perspective. Hence, even though the area you integrate over is A, it only takes up its projected area which is reduced by a factor of $\cos\theta$. The geometry related to this definition is illustrated in the right part of figure 2.2.

2.1.2 Reflectance

All materials absorb some of the radiant power hitting them. Some materials absorb very little, like mirrors, other absorb very much of it, like charcoal or solar cells. In addition, some materials only absorb certain wavelengths, like green leaves, causing them to have colour. *Reflectance* is the quantity describing the amount of power being absorbed by a surface. There exist multiple variants of reflectance, like e.g. the hemispherical reflectance, describing the total amount of power leaving a surface relative to the total amount entering, or the spectral reflectance focusing on the ratio at a specified wavelength. Here we deal with the *directional* reflectance, which is the fraction of power from a direction of incidence reflected in another direction. It is defined as:

$$\rho = \frac{d\Phi_r}{d\Phi_i} \tag{2.4}$$

where $d\Phi_r$ is the reflected flux and $d\Phi_i$ is flux incident on the surface. To ensure conservation of energy, the reflected element of flux due to an element of incident flux from one direction must be in $[0, 1]$. This implies that for any passive material (i.e. having no power being added), $d\Phi_i \geq d\Phi_r \geq 0$, such that

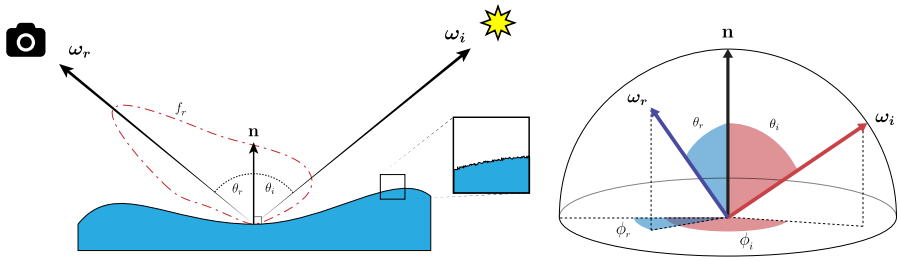

Figure 2.4: The BRDF (f_r) relates the amount of radiance leaving a surface in a specific direction, $\boldsymbol{\omega}_r$ relative to the amount of irradiance hitting the surface from a direction $\boldsymbol{\omega}_i$. The red curve illustrates the value of f_r for varying observation directions (varying $\boldsymbol{\omega}_r$).

$\rho \in [0, 1]$. In figure 2.3 the concept of reflectance is illustrated, where part of the flux incident on a surface is absorbed and the remainder is reflected.

Although we commonly do not deal with spectral reflectance on a per wavelength level when working with computer graphics and BRDFs, it should be mentioned that it is customary, and also applied here, to split reflectance into the 3 colour bands R, G, and B, in order to preserve colour information.

2.2 The Bidirectional Reflectance Distribution Function

Using the above quantities we will now present the precise definition of the BRDF, which was originally coined by Nicodemus [Nic65]. It is formulated as:

$$f_r(\boldsymbol{\omega}_i, \boldsymbol{\omega}_r) = f_r(\theta_i, \phi_i, \theta_r, \phi_r) = \frac{dL_r(\boldsymbol{\omega}_r)}{dE_i(\boldsymbol{\omega}_i)} = \frac{dL_r(\boldsymbol{\omega}_r)}{L_i(\boldsymbol{\omega}_i)\ \cos\theta_i\ d\omega_i} \quad \left[sr^{-1}\right] \quad (2.5)$$

and describes the ratio between the radiance reflected off a surface in a specific direction and the irradiance hitting the surface from another specific direction. In essence, it describes how a surface reflects light. The BRDF depends on the two directions, $\boldsymbol{\omega}_i$ and $\boldsymbol{\omega}_r$, sometimes expanded to $(\theta_i, \phi_i, \theta_r, \phi_r)$, pointing in the directions of the light source and observer respectively. Hence, the BRDF is a 4-dimensional quantity. We visualize this configuration in figure 2.4. With the red dashed line, the figure also illustrates how the BRDF, f_r, may take values for varying observation directions (varying $\boldsymbol{\omega}_r$).

Given a scene containing various light contributions scattered over the hemisphere and shining onto a point on a surface, the observed reflected radiance L_o, e.g. by a camera, at a direction $\boldsymbol{\omega}_r$ can be calculated by plugging the surface-BRDF into the so-called rendering equation [Kaj86]:

$$L_o(\boldsymbol{\omega}_r) = L_e(\boldsymbol{\omega}_r) + L_r(\boldsymbol{\omega}_r) \tag{2.6}$$

$$= L_e(\boldsymbol{\omega}_r) + \int_\Omega f_r(\boldsymbol{\omega}_i, \boldsymbol{\omega}_r) L_i(\boldsymbol{\omega}_i) \cos\theta_i \, d\omega_i \tag{2.7}$$

The term L_e describes the radiance emitted by the surface, and for passive materials, as are the focus of this project, the term can be ignored. In this case, eq. 2.7 is referred to as the reflected radiance equation, and $L_o = L_r$. To keep a consistent notation with r-subscripts we will use L_r rather than L_o in the remainder of this chapter. Equation 2.7 states that the observed radiance is found by integrating all cosine-weighted radiance contributions over the hemisphere, modulated by the BRDF. It may be recognized that this is in fact a 2D convolution between all lights over the hemisphere ($\mathrm{D}E_i$) and the 2D BRDF slice ($f_r(\boldsymbol{\omega}_r)$):

$$L_r(\boldsymbol{\omega}_r) = f_r(\boldsymbol{\omega}_r) \otimes \mathrm{D}E_i \tag{2.8}$$

Here D denotes the derivative [MN+95]. This formulation gives rise to an interesting insight, namely that under a point illumination, which corresponds to a Dirac delta function over the hemisphere, the observed radiance is in fact a sample of the BRDF itself (since $f_r \otimes \delta = f_r$). Symmetrically, the BRDF of an ideal mirror corresponds also to a Dirac delta function, which implies, more intuitively, that the radiance observation of a perfect mirror corresponds to an irradiance sample of a specific position on the hemisphere.

The BRDF is typically formulated in terms of tangent space direction vectors (or angles) as these ensure invariance towards macroscopic effects such as surface curvature, while still being able to model the distribution of microscopic surface variations. It is these variations that are integrated in a resolution cell, like e.g. a pixel, and give rise to material appearance, as illustrated in the zoom-up in figure 2.4. There is no clear border between the micro- and macroscopic realm since it is a matter of choice what curvature should be integrated in the BRDF and what should not. An extreme example is the BRDF of the moon measured from space versus measured from a rock sample in a lab. In the former, surface variations affecting a single resolution cell may constitute mountains, while in the latter we may deal with surface variations in the micron scale.

A range of extensions to the BRDF exists, each of them seeking to encompass additional nuances of appearance that the BRDF itself does not capture. The smallest addition to the BRDF, which is often implicit, is the addition of wavelength dependency: $f_r(\boldsymbol{\omega}_i, \boldsymbol{\omega}_r, \lambda)$, making the function 5D. In practice, this is often only implemented for the R, G, and B, channels to capture the visual part

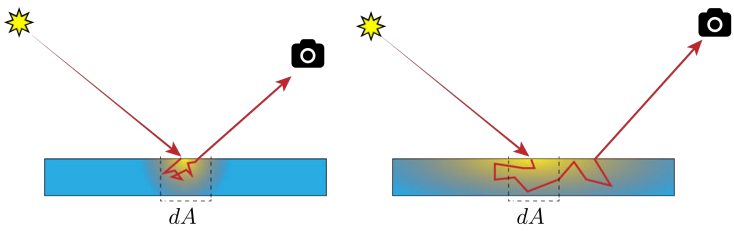

Figure 2.5: Subsurface scattering effects. In scenarios where the re-emitted ray is within a resolution cell (left) the effects can be captured by a standard BRDF. In scenarios where it moves significantly further (right) a subsurface scattering model, BSSRDF, is required.

of the BRDF, but both models and measurements treating this 5th dimension as a continuous variable have been presented [CT82, Foo97].
Spatial variance is a popular extension to the BRDF for inhomogeneous materials. In this case, it is called the *Spatially Varying Bidirectional Reflectance Distribution Function* (SVBRDF) and has the addition of two extra parameters, surface coordinates (x, y), resulting in the 6D function $f_r(\boldsymbol{\omega}_i, \boldsymbol{\omega}_r, x, y)$. This allows modelling materials that vary spatially over a surface. The full 6D function is often impractical to work with, and in practice, SVBRDFs are implemented using texture maps holding model parameter values or weights for linear combinations of a smaller set of BRDFs.
Finally the *Bidirectional Scattering-Surface Reflectance Distribution Function* (BSSRDF) includes subsurface scattering which is not captured by a traditional BRDF. The diffuse component of materials is caused by very local surface and subsurface scattering effects that are contained within the area of a single resolution cell, dA, as depicted in the left part of figure 2.5. When this is not the case and the position of the re-emitted ray cannot be assumed to leave the surface at the same place it entered, a BSSRDF is required. This is depicted in the right of figure 2.5. The BSSRDF adds 2 additional parameters, indicating the location on the surface at which the light leaves. This makes the BSSRDF an 8D function: $f_r(\boldsymbol{\omega}_i, \boldsymbol{\omega}_r, x_{in}, y_{in}, x_{out}, y_{out})$. Probably the most famous work with this model is that of Jensen et al. [JMLH01] that also resulted in an Academy Award in 2004 for its use in the movie industry.

2.2.1 Properties

In contrast to the reflectance, ρ, defined in eq. 2.4, the BRDF is the ratio of quantities with different units and may therefore take values greater than 1. Instead, energy conservation states that when integrating over all possible

directions of observation, the BRDF should total to no more than 1:

$$\forall \boldsymbol{\omega}_i : \quad 0 \leq \int_\Omega f_r(\boldsymbol{\omega}_i, \boldsymbol{\omega}_r) \cos\theta_r \, d\omega_r \leq 1 \tag{2.9}$$

In fact, as mentioned above, the BRDF of a perfect mirror is a Dirac delta function, being infinitely large when the observation direction coincides with the reflected direction of the light, and zero everywhere else. And in contrast, a perfect diffuse surface with no absorption will have a constant BRDF of $f_r = \frac{1}{\pi}$ (since the integral of the cosine over the hemisphere equals π). This property also becomes clearer with the relationship between the two quantities defined:

$$f_r = \frac{dL_r}{dE_i} = \frac{d\left(d^2\Phi_r / \left(\cos\theta_r \, dA \, d\omega_r\right)\right)}{d\left(d\Phi_i / dA\right)} = \frac{d\rho}{\cos\theta_r \, d\omega_r} \tag{2.10}$$

Another important property of the BRDF is that it obeys Helmholtz reciprocity:

$$f_r(\boldsymbol{\omega}_i, \boldsymbol{\omega}_r) = f_r(\boldsymbol{\omega}_r, \boldsymbol{\omega}_i) \tag{2.11}$$

stating that a ray of light's path is reversible, meaning that the position of sensor and light-source may be swapped freely without it affecting the amount of light measured. In computer graphics, this property is utilized in e.g. raytracing where rays are shot from the eye, in contrast to bidirectional path tracing or photon mapping where rays are shot from the light sources. This property is also very convenient in a measurement scheme since $f_r(\theta_i, \phi_i, \theta_r, \phi_r) = f_r(\theta_i, \phi_i + \pi, \theta_r, \phi_r + \pi)$, implying that only half the hemisphere needs to be covered: $\theta \in \left[0, \frac{\pi}{2}\right]$ and $\phi \in [0, \pi]$.

For a large group of materials, rotating the surface around its normal will not affect the amount of reflected light in any given light/view configuration. Materials holding this property are called isotropic and materials not holding it are called anisotropic. Most everyday materials are isotropic and to give a better understanding of the difference between to two types, it therefore makes more sense to give examples of anisotropy. Brushed metal, fabric, and hair are all well known anisotropic materials. Microstructures in the surfaces (brush strokes, weaving) cause them to have preferred directions of reflection, making them vary with rotation. Generally, anisotropic materials are hard to find in nature and are usually a result of some sort of processing.
As stated, isotropy implies that the BRDF is invariant with respect to rotations around the surface normal, i.e.

$$f_r(\theta_i, \phi_i, \theta_r, \phi_r) = f_r(\theta_i, \phi_i + \alpha, \theta_r, \phi_r + \alpha) \quad \forall \quad \alpha \in \mathbb{R} \tag{2.12}$$

meaning that it is, in fact, possible to represent an isotropic BRDF using only 3 parameters by introducing the relative azimuthal angle, $\phi_{\text{diff}} = (\phi_i - \phi_r)$:

$$f_r^{iso}(\theta_i, \phi_i, \theta_r, \phi_r) = f_r^{iso}(\theta_i, \theta_r, \phi_{\text{diff}}) \quad \in \mathbb{R}^3 \tag{2.13}$$

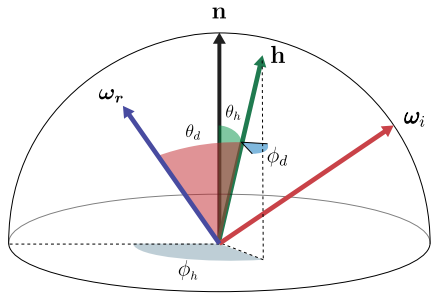

Figure 2.6: The Rusinkiewicz half-vector parametrization. Angles are measured relative to the half-vector, the unit-length average between light- and observer-directions.

Hence, the isotropic BRDF is a more compact, 3-dimensional, version of the full BRDF.
In this thesis, only isotropic materials are dealt with. Although this is a limitation, the group of isotropic materials still constitutes a very large fraction of common material appearance.

We will later touch upon a selection of analytical BRDF models. Models obeying the law of energy conservation and the Helmholtz reciprocity are, depending on how they were derived, deemed either physically based or physically plausible. Models not having these properties are called non-physical. Furthermore, some of these models are capable of explaining anisotropy, while others are not. This is linked to the complexity of the models and what material domains they were targeted for.

2.2.2 Coordinate Frames

As has been used until now, a common coordinate frame used when discussing BRDFs is the spherical coordinate system (r, θ, ϕ) depicted in the right of figure 2.4. Since it is directions that are dealt with, the radial distance, r, is usually disregarded, resulting in a 2D parametrisation of direction. This is both a compact and very intuitive representation, making it easy to work with.
An alternative and very interesting representation is the Rusinkiewicz half-vector parametrization $(\theta_h, \phi_h, \theta_d, \phi_d)$ that is centred around the specular highlight [Rus98]. We visualise this representation in figure 2.6. In contrast to spherical coordinates, where angles are measured relative to the surface normal, the Rusinkiewicz parametrization describes coordinates relative to the half-vector,

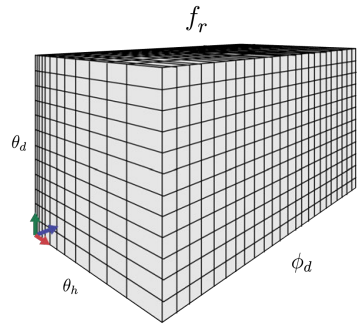

Figure 2.7: The MERL BRDF representation, using the isotropic Rusinkiewicz parametrization with a non-linear θ_h mapping. Data is packed into a grid consisting of $90 \times 90 \times 180$ samples.

$\boldsymbol{h} = \frac{\boldsymbol{\omega}_r + \boldsymbol{\omega}_i}{\|\boldsymbol{\omega}_r + \boldsymbol{\omega}_i\|}$. It is centred around the specular highlight as this is located at $\theta_h = 0$. From a physics point of view, models based on the half-vector are deemed more physically plausible. Finally, isotropy is easily achieved by discarding ϕ_h, which describes the entire configuration's rotation around the surface normal.
The Rusinkiewicz parametrization is advantageous in analytical models that seek symmetry around the specular highlight, but especially also in data-driven models where it is of interest to pack data densely around the highlight to achieve a high resolution representation of reflections. The MERL format [MPBM03a] is a very relevant example of where this parametrization is utilised. In this isotropic 3D representation $(\theta_h, \theta_d, \phi_d)$ BRDFs measured from images of spheres [MPBM03b] are packed into a $90 \times 90 \times 180$ grid. In order to achieve a high fidelity highlight, which is perceptually a very important part of the BRDF, the first axis θ_h is mapped nonlinearly in this grid. With this non-linear grid-representation, observations closer to $\theta_h = 0$ are sampled more densely than samples further away. We visualize this representation in figure 2.7

2.2.3 Visualization

As a 4D or 3D quantity, visualising a BRDF, i.e. mapping it to a 2D representation, can be done in multiple ways and produces very different results. Depending on what information is sought extracted or conveyed some methods may be preferred over others. We here present 3 common approaches to visualising a BRDF.

A traditional and very fast approach to visualising a BRDF is by applying it

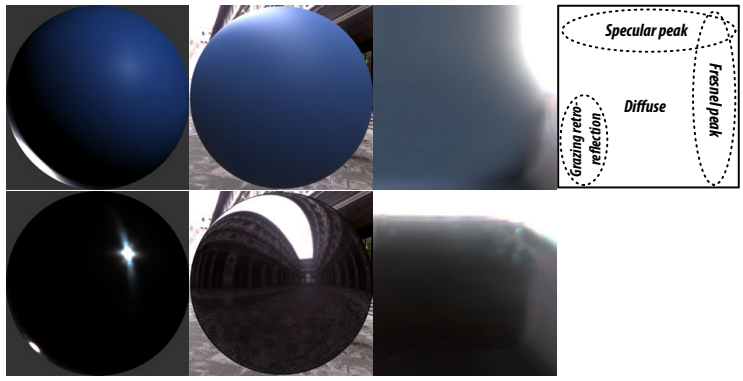

Figure 2.8: Visualizations of 2 BRDFs (rows) using different visualization methods. 1st. column: 2 point light-sources. 2nd column: Ray-traced rendering under environment lighting (physically based render). 3rd column: A normalized slice through the BRDF volume at $\phi_d = 90°$. 4th column (top row) a reference for BRDF slice interpretation.

to a smooth geometry and rendering it under a point light-source using the rendering equation (eq. 2.7). Commonly, simple geometry such as spheres or Stanford dragons are used, and also additional point lights may be added. In the first column of figure 2.8, we demonstrate this approach where two point lights, an oblique front light and a grazing back light, are used. As mentioned earlier, point lights give direct insight into the values of the BRDF but are perceptually somewhat weak. Alternatively, using a physically based rendering system, the BRDFs may be rendered in a physical environment [Deb98] as shown in the second column of figure 2.8. Perceptually this visualisation is very rich on information to humans, but the integration over the hemisphere washes out many finer details in BRDFs weakening numerical comparisons. Finally, slices made through the isotropic BRDF volume shown in figure 2.7, at $\phi_d = 90°$, have been proposed by Burley et al. [Bur12]. Such slices are shown in the third column of figure 2.8. These give direct insight into the behaviour of isotropic BRDFs and are able to, in a single image, give an intuition of diffuse, specular, Fresnel, and retro-reflection components. A reference to the interpretation of BRDF slices is shown in the 4th column of figure 2.8. In BRDF-model-fitting, to ease the computational burden, BRDF slices have been used rather than the full BRDFs, allowing for speeding up computations considerably.

2.2.4 BRDF Models

By far, the most compact way of representing the 4D BRDF manifold is through analytical models and hence they are the most commonly used. A wide range of analytical models exist and it is beyond the scope of this thesis to cover them all in detail. In this section, a selection of popular BRDF models will be introduced to give the reader an impression of the main design patterns behind analytical BRDF models. Afterwards, we will touch upon existing data-driven models.

Disregarding the diffuse BRDF, which under rendering is simply a constant, the first and probably still most used model is the Phong model [Pho75], adding specular highlights to a rendering. The model is given by:

$$I = k_d \cos\theta_i + k_s \cos\theta_{ro}^{\alpha} \tag{2.14}$$

where I is the observed intensity of a pixel, θ_i is the inclination of the light-source and θ_{ro} is the angle between the observer and the reflected light-ray. The parameters k_d and k_s specify the diffuse and specular intensities respectively, and α indicates the specularity of the material. As presented in eq. 2.14, the Phong model is not an actual BRDF model as it includes the geometrical factor, $\cos\theta_i$, in the formulation. It can be reformulated as a BRDF with $f_r = k_d + k_s \cos\theta_{ro}^{\alpha} / \cos\theta_i$, this however leads to a problem with energy conservation as the BRDF goes to infinity as grazing angles go to the tangential direction [Lew94]. With that said, it is still a perceptually fine model, which is easy and fast to compute and holds only 3 parameters (7 for RGB), making it the most compact model beyond the diffuse.

A re-iteration of the Phong model is the Blinn-Phong model [Bli77], addressing the major drawbacks. This model draws on the half-vector representation in the specular component, making it physically plausible using the correct parameters. In its orignal form, it only replaces θ_{ro} with θ_h:

$$I = k_d \cos\theta_i + k_s \cos\theta_h^{\alpha} \tag{2.15}$$

which still has the issue of going to infinity, but it can be modified slightly to be a physically plausible BRDF for all values [AMHH08]:

$$f_r^{BP} = \frac{\rho_d}{\pi} + \frac{\alpha + 8}{8\pi} \rho_s \cos\theta_h^{\alpha} \tag{2.16}$$

which is the variant we used in our work.

Microfacet models are models that assume a surface to consist of a distribution of microscopic, randomly oriented, and perfectly reflecting facets as visualised in figure 2.4. The spread and shape of the distribution determines the specular

reflection of the surface and for very broad distributions the surface appears rough, and for narrow distributions, it appears shiny.
The modified Blinn-Phong model (eq. 2.16) can be seen as a microfacet model with the facets distributed according to a cosine-distribution. Alternatively, the microfacets may be normally distributed which is the case of the Ward BRDF model [War92], that in addition to modelling using a different distribution also introduces anisotropy:

$$f_r^{\text{Ward}} = \frac{\rho_d}{\pi} + \frac{\rho_s}{4\pi\ \alpha_x\alpha_y\ \sqrt{\cos\theta_i \cos\theta_r}}\ e^{-\tan^2\theta_h\left(\frac{\cos^2\phi_h}{\alpha_x^2}+\frac{\sin^2\phi_h}{\alpha_y^2}\right)} \tag{2.17}$$

Setting $\alpha_x = \alpha_y$ will, of course, lead to an isotropic BRDF with the same number of parameters as the Phong and Blinn-Phong models.

The models presented above all have in common that they rely on a single distribution/lobe modelling a material. Most often nature is not easily explained using a single parameter distribution. BRDFs are no exception and empirical studies show that simple models, as presented above, often fail to accurately model what is measured. Much like Gaussian Mixture Models, the Lafortune [LFTG97] model seeks to better model measurements by using a linear combination of cosine-lobes under the constraints of being reciprocal and energy-conserving:

$$f_r(\boldsymbol{\omega}_i, \boldsymbol{\omega}_r) = \sum_{l=1}^{n} \rho_s \left[\boldsymbol{\omega}_i^T \boldsymbol{M}_l \boldsymbol{\omega}_r\right]^{\alpha_l} \tag{2.18}$$

Here any number of lobes, n, can be used in linear combination to model appearance. Each lobe has a scaled rotation matrix $\boldsymbol{M}_l$ and a specularity term α_l associated with it.

While Phong, Blinn-Phong, Ward, and Lafortune models are all empirically based, another important branch is the theoretical models based on physical theory. Such models are generally more flexible and more accurate, but at the cost of having many tunable parameters. No physical models were used in this thesis and we will thus only mention a single one briefly, namely the Torrance-Sparrow model [TS67, Bli77, CT82].
The Torrance-Sparrow model is based on microfacet theory and separates the distribution of microfacets into 3 components, D, F, and G:

$$f_r^{\text{CT}} = \frac{\rho_d}{\pi} + \frac{DFG}{4\cos\theta_r \cos\theta_i} \tag{2.19}$$

The first component is the distribution factor, which is based on the Beckmann distribution of microfacets [BS63]:

$$D = \frac{\exp\left(\frac{-\tan^2\theta_h}{m^2}\right)}{\pi m^2 \cos^4\theta_h} \tag{2.20}$$

where m is the root mean squared slope of surface microfacets, i.e. a roughness term.
The second component is the Fresnel factor, F, modeling the amount of reflected v.s. transmitted light. Usually Schlick's approximation [Sch94] is used:

$$F = f_0 + (1 - f_0)(1 - \cos\theta_i)^5 \quad \text{where} \quad f_0 = \left(\frac{1-n}{1+n}\right)^2 \tag{2.21}$$

with n being the material's refractive index.
Finally, G models the geometrical attenuation caused by selfshadowing effects in the microfacets:

$$G = \min\left(1, \frac{2\cos\theta_h \cos\theta_i}{\cos\theta_d}, \frac{2\cos\theta_h \cos\theta_r}{\cos\theta_d}\right), \tag{2.22}$$

using the Rusinkewicz parametrization from figure. 2.6. In this model, we thus have two parameters affecting the specular component, n and m, and since n may be wavelength dependent, the number of parameters for an RGB variant totals 7. Although comparable to the previous models parameter-wise, this model is computationally heavier to work with.

The models presented above all focus on proper modelling of the specular highlight. It is from this apparent that the main challenge in faithfully capturing and modelling appearance lies in getting the highlight right. And from the span of suggested methods to the pure number of proposed models, it is apparent that a one-size-fits-all model has not yet been found.

2.2.4.1 Measured BRDFs

One obvious way of getting around the issue of determining a proper analytical BRDF model is to simply measure the BRDF itself. Obviously, this is not possible in many cases and even if so the slow acquisition speed when densely sampling BRDFs is prohibitive. Nonetheless, a span of measured BRDFs exists, acquired to yield insight into the variability of material appearance. As will be touched upon in the next section, measuring full BRDFs is a time-consuming process, which has resulted in most datasets being small and often of low resolution.

The philosophy behind measured BRDFs is to have a lookup table (LUT) of BRDF values, such that while rendering one would simply look up the value associated with a given light- and view-direction. The advantage of LUTs compared to analytical models is particularly that they are ground truth and not approximations, but also that they are extremely fast to compute since they

require only a memory lookup. The downside is that they are memory-wise heavy to deal with, and in scenes consisting of many materials the memory consumption quickly exceeds what is available on a graphics card. Also, measured BRDFs are usually sampled in a somewhat coarse grid, giving rise to the need for interpolating values when a light/view configuration is not contained in the LUT. Although interpolation can be performed extremely fast on graphics cards it still introduces synthetic values to the rendering which may contaminate results. Furthermore, the BRDFs may not be parameterised in a regular grid, making such interpolation non-trivial.

Commonly, there are two different representations of measured BRDFs: Regularly sampled, and irregularly sampled. For example, the MERL representation [MPBM03a] depicted in figure 2.7 is an example of a regularly sampled BRDF. Reflectance values are stored in a regular grid, making looking up and interpolating values extremely easy. The MERL format is based on the Rusinkiewicz parametrization, but one could just as well use standard spherical coordinates for this.
Irregularly sampled BRDFs are often represented as lists of observations with no immediate order. An example is the Cornell BRDF format [Foo97]. Often they are to some extent uniformly distributed, but may lack observations where e.g. view and illumination coincide (or is close to), or they may have extra observations around regions of interest such as specular highlights. It is a bit more tricky to use these formats as LUTs since they involve a (k-) nearest neighbour search. This can be achieved rather fast through e.g. KD-Trees, but is nonetheless an overhead compared to regularly sampled BRDFs.

2.2.5 Measuring Reflectance and BRDFs

Measuring a BRDF is in many senses a straightforward task: For every angle of view and illumination, illuminate a material sample and measure the amount of received light. This allows calculating the fraction of reflected light compared to the incident light for all light-/view-configurations which is basically the definition of the BRDF. We visualise this concept in figure 2.9 where a device moves a light source and a detector over the entire hemisphere while measuring the reflectance of a sample. Such a device is called a gonioreflectometer. As the BRDF is a 4D quantity it is apparent that the process of measuring a full 4D BRDF is indeed very time-consuming. To acquire a full 4D BRDF in 1° resolution requires $90 \times 180 \times 90 \times 180 \approx 2.6 \cdot 10^8$ samples. Could this be achieved with 1 sample per second it would amount to a measurement of a little more than 8 years! Thus people often compromise on resolution or stick to isotropic materials or even the inplane-BRDF (a sweep of θ_r, with θ_i fixed and $\phi_r = \pi - \phi_i$).

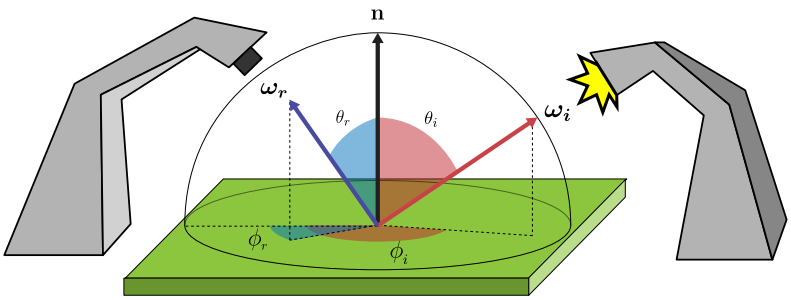

Figure 2.9: Concept of sampling a BRDF. All configurations of $(\theta_i, \phi_i, \theta_r, \phi_r)$ should be covered. This requires both a movable light source and a movable detector.

How in practice to achieve the BRDF sampling varies. Gonioreflectometers may be implemented in different ways. Two different variants that were used in this Ph.D. project are depicted in figure 2.10. To the left, the UCSD spherical gantry is shown. This is a classical gantry setup consisting of two arcs holding light and detector respectively. Each arc is capable of covering the full hemisphere, allowing full coverage of the BRDF domain. To the right, the DTU robot system is shown. This setup is based on a multipurpose robot arm holding the detector, while an arc of LEDs constitutes the variable light. Per default this only allows 3D isotropic BRDFs to be sampled, but in conjunction with a rotation table below the target sample, the full 4D BRDF can be sampled. Also, the θ_i resolution is constrained to the increments of the LEDs, being 7.5°. In both setups, the detectors used are CCD cameras. In such cases, in order to convert from pixel intensities to radiometric units, proper calibration is needed. This procedure is described by Debevec in [Deb98].

The canonical approach described above is slow and one obvious mean of speeding up the sampling process is by utilising the parallelism of a camera's CCD sensor to acquire multiple reflectance observations per image. This may be achieved by e.g. taking images of materials shaped as spheres, as was done by Matusik et al. [MPBM03b], or using curved mirrors to observe a sample from multiple directions at the same time, like in the work of Ward [War92]. In C.VI we demonstrate that parallel sampling may also be done by simply moving a camera very close to the sample, thus taking advantage of the camera's field of view.

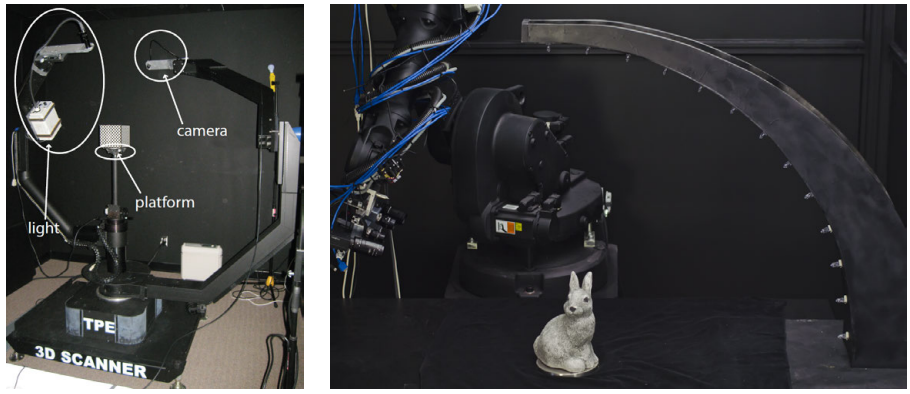

Figure 2.10: Two different gonioreflectometers. Left: the UCSD Spherical Gantry based on two motor-controlled arcs holding a directional light-source and CCD camera respectively. Right: the DTU robot system based on a multipurpose robot arm moving the camera, in conjunction with an arc of LED lights.

Chapter 3

Related Work

Recall that the aim of this thesis is to acquire BRDFs using few measurements and to represent BRDFs using a practical model. This chapter covers work that is relevant towards this endeavour. It mainly falls into two major categories: related work concerning *appearance modelling*, and work concerning *appearance acquisition*. The works [HF13] and [WK15] are excellent surveys on these topics. The field of appearance modelling is concerned with creating BRDF models that faithfully capture material behaviour. The field of appearance acquisition deals with accurately measuring BRDFs from real-world objects. Although separated here, the two topics are often intertwined with e.g. data-driven appearance models based on measured BRDF data, or BRDF measurement procedures estimating analytical model parameters rather than a full 4D quantity.

Much of the work that is dealt with here was to a large extent pioneered by Nicodemus and his group in their work on optical radiation. A great part of this is summarised in the self-study manual [Nic77]. Specifically, he is to be credited for the derivation of the BRDF [Nic65], which is the very foundation of not only this thesis but all the related work mentioned in this chapter. Also, noteworthy, the concepts of radiance and irradiance were coined in his works [Nic63], and just as importantly, his guidelines on how to measure these quantities.

3.1 Appearance Modelling

As described in chapter 2, when modelling appearance, i.e. creating BRDF models, there are typically two ways to approach this. Either one tries to define a mathematical model, perhaps based on physical theories or empirical studies, or one tries to represent the BRDF through measurements (a data-driven model). While the former has the advantage of being compact, it often oversimplifies the world. The latter, on the other hand, can be exact but is often impractical to work with or to obtain.

3.1.1 Analytical Models

Driven by especially the computer graphics industry, the span of analytical BRDF models is quite large. For the sake of brevity, this section narrows its focus to analytical models having a connection to the theme of this thesis, namely practicality. It thus focuses primarily on models designed for matching real world measurements and considerations on how to fit them.

The Phong model [Pho75] was the first to formulate a plausible model for specular highlights in the pipeline of early rendering frameworks, taking the first step towards a better modelling of the real world. This overly simplified model is neither reciprocal nor energy conserving, making it highly implausible. Blinn addresses this partly in the Blinn-Phong model [Bli77] in search of being better at modelling measurements, by making a correction to the positioning of the specular lobe. This allows for a more physically plausible behaviour of the specular lobe, matching real world materials better. Much like the Blinn-Phong model, the Ward model [War92] suggests a specular lobe centred around the half-vector, but the falloff is here modelled by a Gaussian rather than a cosine power. In addition, it allows shaping the specular peak to simulate anisotropy. These models seek to capture material appearance using a single specular lobe. Although the models are compact and thus good for data-fitting it is well known that they generally fail in accurately modelling the full appearance of real materials [NDM05]. An obvious flaw in these models is the lack of Fresnel effect, i.e. a strong specular lobe at grazing angles. In addition to this we generally observe the shape of the specular peak, i.e. its falloff, does not follow observations properly and either decays too fast or too slow.

Derived in the optics community, the Torrance-Sparrow model [TS67] describes the interaction between a ray of light and a rough microfacet surface. This model was later adopted in the computer graphics field by Cook [CT82] and Blinn [Bli77], addressing many of the shortcomings of the simpler models men-

tioned above, including the missing Fresnel effect. The nature of the microfacet model, with the specular component being factored into Distribution, Fresnel, and Geometry (D,F, and G in eq. 2.19), allows for a broad range of modifications to be made to it. Specifically, the distribution term D, that in many senses dominates the shape of the specular lobe, has received a lot of attention. In search of more accurately modelling real world measurements, alternative variants have been proposed. Walter et al. propose a distribution of microfacets called GGX [WMLT07] rather than the Beckmann distribution [BS63], providing a wider tail to the specular peak. This distribution is, in fact, equivalent to the Trowbridge-Reitz distribution [TR75] which Disney also uses in a generalised form called GTR [Bur12]. Likewise, Ashikhmin and Promože [AP07] suggest a normalised Phong distribution and are able to deduce measurement strategies for obtaining the model-parameters from new materials. Adding a second parameter to D in order to capture the appearance of measured materials even better, Bagher et al. propose the shifted gamma distribution [BSH12] giving more flexibility to the falloff, and even adding a third parameter pushing it to the limit of models suitable for data-fitting, Löw et al. propose a distribution based on the ABC density model [LKYU12]. Clearly, there is a lot of flexibility inherent in the microfacet model. Above, only suggestions to modification of the distribution parameter D have been mentioned. Likewise, modifications to the Fresnel term F (the standard Schlick approximation [Sch94] is a computationally advantageous modification), and to the geometrical term G have been proposed [HTSG91, WMLT07]. Brady et al. [BLPW14] propose a creative approach based on genetic programming by letting the microfacet model "evolve" into a format that fits measurements better, modifying all components. Based on this they present a selection of new parametric models capable of matching measurements particularly well. An interesting insight the models give is that a two-parameter D distribution is generally needed.
To this extent, the span of microfacet-based models is vast. Even so, none of the models have proven to provide consistently good fits to measured data. As the number of parameters added to the models steadily increases, we move towards a point where we may need to rethink our strategies if we wish to have our models remain practical. Recent micro-flake models, with an origin in the microfacet model, produce impressive and realistic surface effects but at a cost of an even greater complexity, making them for artistic purposes only [JAM+10, HDCD15].

Attacking the problem at hand from another angle, a range of alternative approaches have been proposed. Focusing on accurately modelling the specular peak, rather than trying to capture its falloff curve in one single complex parametric distribution, it may be modelled by a combination of simpler distributions or lobes. The most generalised approach to this is by modelling the entire 3D or 4D BRDF space by a set of basis functions. Methods based on spherical harmonics [SAWG91, WAT92], wavelets [SS95, LF97, MPBM03b], and function decompositions [KM99] have been proposed. All are theoretically capable of

modelling any BRDF perfectly, but in practice, they require too many coefficients to approximate data accurately in order to be practical [WLT04]. Lafortune et al [LFTG97] employs a more controlled strategy to accurately match a broad range of measured materials. The method is based on a generalisation of the cosine lobe model and allows an arbitrary number of linearly combined cosine lobes to capture the highlight. The model yields superior results to most single lobe models such as Ward, Phong and Blinn-Phong. Unfortunately, what should have been the strength, using multiple lobes tends to make the fitting process to real data unstable, making it impractical in data-fitting [NDM05]. Finally, layered microfacet models have been proposed, modelling BRDFs as superpositions of multiple semi-transparent microfacet layers [WW07, JdJM14]. These models achieve convincing results, but again, realising that these models were designed for artistic purposes, we move towards a complexity too high for the models to be practical in BRDF estimation and data-fitting.

From the above, it is apparent that a broad range of flexible BRDF models exists and that a massive effort has been devoted into accurately modelling appearance. Even so, although BRDF models have moved a long way from their earliest variants, Blinn-Phong, Ward, & Torrance-Sparrow, it is striking that it is still those very models we see applied in practical settings today. Most likely this is caused by a combination of computational complexity (we want real-time visualisation), and the complexity of the optimisation problem (we don't want local minima fits). It argues that we are still in need of a practical model with the simplicity of early models, but with broader coverage of materials.

3.1.2 Data-driven Models

Realising the limitations of analytical models, a completely different strategy is to simply drive appearance models via real world data, either partially or fully. The major challenges here are to obtain sufficient and accurate data, and from these data, to extract the general trends and features constituting real world BRDFs.

Much work has been devoted into accurately measuring BRDFs from real world materials. Unfortunately, due to the complexity of the BRDF, the datasets are few and small. One of the first publicly available datasets is the Cornell database [Foo97]. It contains irregularly sampled BRDFs of industrial materials such as paints, ceramics, and metals. One of the major strengths of this dataset is the multispectral observations, ranging from 400nm to 700nm. Another early dataset is the Columbia-Utrecht Reflectance and Texture Database [DVGNK99] consisting of approximately 60 BRDFs coarsely sampled using 205 samples spanning the full 4D BRDF domain. It contains a broad range of materials with

features including: isotropy, anisotropy, microscopic roughness and macroscopic roughness. Due to its coarse sampling it, unfortunately, fails in fully capturing the material appearances. Probably the most famous dataset is the MERL database by Matusik et al. [MPBM03a]. It consists of a hundred densely measured isotropic BRDFs stored in a $90 \times 90 \times 180$ grid. Due to the acquisition approach, based on images of spheres, the database spans a category of materials that was able to be shaped into spheres. This span is good, but some wrapping artefacts etc. are present in some materials. In continuation of Matusik's work, Ngan et al. [NDM05] present the MIT anisotropic database, consisting of 4 densely sampled anisotropic BRDFs in a 2°-increment regular grid. To our knowledge, these measurements are the most comprehensive ones done that are publicly available. Finally, a recent 4D dataset has been published by Filip et al. [FV14]. This dataset holds no less than 150 materials, each sampled by approximately 7000 measurements and interpolated into a regular grid of 80.000 directions. Although not as dense as the measurements by Ngan, the breadth and relatively high density of this dataset is noteworthy.

McCool et al. [MAA01] are among the first to demonstrate that both complex analytical BRDF models and measured BRDFs can advantageously be represented as products of 2D texture maps on a graphics card, i.e. a data-driven model, providing an at that time so far unachievable real-time performance compared to the complexity of the data. Later, a data-driven reflectance model based on the MERL database is suggested by Matusik et al. [MPBM03b]. In this approach, new materials are modelled purely as linear combinations of measured BRDFs. Furthermore, Matusik et al. conclude that approximately 800 samples of a BRDF may be sufficient to accurately reconstruct its full appearance from the linear basis. Two alternate strategies for decomposing BRDFs are also proposed based on Principal Component Analysis (PCA) [Hot33] and a nonlinear dimensionality reduction (NLDR) of the MERL database [MPBM03a]. These decompositions result in dimensionality reductions to 30-40 and 10 parameters respectively, making them relevant for practical use.
Much like Matusik's work, Weyrich uses the MERL database to model human skin through a decomposition based on non-negative matrix factorization [WMP+05]. In their results, as little as 6-8 components are sufficient, making them comparable to many analytical models. Finally, Hullin et al. [HHA+10] use the same strategy as Matusik to model fluorescence in re-radiation reflectance functions (bispectral BRRDFs) on data from their own image-based system.

While the methods proposed above seek to capture every facet of the BRDFs through data, i.e. learn the entire 4D manifold of BRDFs from data, also hybrid approaches have been proposed. These methods seek to reduce the amount of data required by using analytical models for well-described phenomena and only data for effects that are difficult to model.

The Torrance-Sparrow model [TS67] (eq. 2.19) constitutes a nice framework for this philosophy as it is by definition composed of three separate terms. Although often approximated, the Fresnel term, F, is a well-modelled quantity. In contrast, the geometrical factor G, and *especially* the distribution factor D have proven difficult to model analytically as the span of proposed distributions above suggest. Ashikmin et al. [APS00] propose a framework for taking a tabulated microfacet orientation distribution and automatically produce D and G such that the resulting BRDF is both energy conserving and reciprocal. Ngan et al. [NDM05] employ this framework to model anisotropic BRDFs with good results compared to ground truth, Wang et al. [WZT+08] apply it to spatially varying BRDFs, and finally, Ghosh et al. [GHP+08] use it in conjunction with subsurface-scattering models to reproduce human face appearance. Related, Bagher et al. [BSN16] propose tabulating all three factors of the Torrance-Sparrow model, and device an optimisation scheme capable of robustly estimating 1D vectors associated with D, F, and G producing superior results to previous work.

In the overlap between measured and analytical BRDFs, the problem of model fitting arises. Before finishing this section we will briefly touch upon what considerations have been made on this. Realising that parametric models are only a simplification of the real world, a choice on what features to value higher than others must be made. Mostly this is linked to what features are visually most important. In the optimisation pipeline, this basically boils down to the choice of objective function. Due to the high dynamic range of the BRDF values, McCool suggests working in a log-domain [MAA01] rather than using the classical root mean squared (RMS) error. Likewise, Fores et al [FFG12] conclude that the cube root has a perceptually better weight. Instead of working on the actual BRDF values, derived quantities such as renderings under environment lighting have also been proposed as they by nature mimic how we perceive materials [FDA03]. Unfortunately, the computational cost of producing such renderings is high compared to the former metrics and furthermore, one still has to decide on a pixel-error metric afterwards which has been investigated by e.g. Rushmeier et al. [RWP+95] and more recently by Pereira et al. [PR12]. Finally Havran et al. [HFM16] have recently demonstrated a 3D scene with optimised geometry, view, and illumination for maximising difference between anisotropic materials.
The general notion in model-fitting is that fitting to the top of the specular peak, like the L^2 norm does, produces poor results. Although a range of alternative variants have been proposed that seek a better highlight-compromise, none stand out particularly better than the others.

Previous work has generally shown that data-driven BRDF models are capable of producing results superior to those of analytical models. On the other hand, for material categories that the models have not been trained on, perfor-

mance may be strikingly poor where even the simplest analytical models can outperform the data-driven. This issue illustrates the major weakness of the data-driven BRDF models, namely their dependency on large amounts of training data. The work of Matusik et al. [MPBM03a] has to a large extent enabled the first generation of data-driven BRDF models to come into existence, but even this dataset is limited in many ways. In order to cover a broader range of BRDFs, or even cover the full 4D manifold, more data is inevitably needed. This problem leads to the challenge of effectively acquiring BRDFs.

3.2 Appearance Acquisition

Just as there has been considerate efforts in accurately *modelling* reflectance, much work has been placed into *capturing* reflectance. Especially, given the comprehensiveness of the BRDF, efforts have been made in speeding up the acquisition process with the goal of making BRDF-capture and data-driven models *practical*. The main contributions presented in this thesis primarily lie in this category, dealing with finding practical data-driven models and practical BRDF capture techniques.

3.2.1 Traditional and Image-Based BRDF Measurement

The simplest approach to measuring a BRDF is, of course, the canonical approach of covering all light/view configurations for a flat material sample using a gonioreflectometer, as done by e.g. White et al. [WSB+98]. Although the simplicity of the setup makes it appealing, the approach is slow and impractical for densely sampled BRDFs. This has spawned a range of modifications to the original setup with the aim of speeding up the acquisition process.

Perhaps the simplest modification is that of Marschner et al. [MWL+00], that utilises the parallelism of a camera CCD chip by acquiring images of homogeneous materials shaped as spheres from a 1D set of light directions. This allows them to, relatively fast, capture an isotropic 3D BRDF and it is indeed this approach that was used by Matusik et al. [MPBM03a] to acquire the MERL database. Related, Ngan et al. [NDM05] use cylinders in a similar setup to capture 4D anisotropic BRDFs. Both methods are relatively fast compared to the canonical acquisition approach but suffer from being limited to materials that can be wrapped around, or shaped into, spheres and cylinders.

Rather than modifying the material sample, a range of methods have been pro-

posed that utilise mirrors in various configurations to acquire multiple BRDF samples with a camera. In his "imaging gonioreflectometer" [War92], Ward utilises a half-sphere mirror and a fisheye-lens to capture 2 of the 4 dimensions of a BRDF in parallel. Likewise, Dana and Wang [DW04] utilize the focusing property of a concave parabolic mirror to obtain multiple view directions of a SVBRDF in parallel, and in a similar configuration based on two opposing parabolic mirrors, Ghosh et al. are also able to speed up BRDF acquisition of isotropic materials to just a few minutes [GAHO07]. Related, Ihrke et al. [IRM+12] employ a kaleidoscopic mirror-setup to likewise acquire samples in parallel. Finally, complex setups consisting of full light domes and movable cameras have been proposed [NSKR13, SSW+14].

The methods presented above all reduce acquisition time considerably and are in theory all fairly simple. Furthermore, most of them produce "authentic" measurements of the material that have not been affected by any data-prior. Unfortunately reproducing these setups in practical settings is generally costly, making it prohibitive to the majority of users.

The method that we propose has the advantage of being very flexible in that the user may choose any light/view configuration, be that an e.g. complex robot-based setup or a simple static experiment with a few cameras and lights, and obtain good results. The result, however, is biased towards the underlying data-driven model [NJR15].

3.2.2 Adaptive and Efficient Sampling

As opposed to blindly measuring the full BRDF in a dense grid, Fuchs et al. [FBLS07] identify that due to the low-frequency nature in large parts of the BRDF, not all regions of the BRDF domain require the same amount of attention. Based on how well a neighbourhood of observations is capable of modelling an observation, an adaptive sampling scheme is devised, seeking to refine only regions that are in need of additional observations. In a similar approach, Lensch et al. [LLSpS03] fit a parametric BRDF model to measurements and based on an uncertainty measure of the fitted parameters, new measurement positions are calculated. In contrast to Fuchs et al, this approach relies on an analytical model and as a result, the BRDF features measurable by the method are dictated by the choice of analytical model.

Both of the above approaches combine nicely with many of the proposed hardware improvements mentioned in the previous subsection, this could potentially speed up the acquisition process further and is a potential area for future research.

In our optimal sampling framework, we provide the user with a list of tabulated optimum sampling configurations, generated for any predefined number of measurements. This list is based on how BRDFs generally behave, but the framework also allows for creating new lists based on specific material categories.

3.2.3 Complex Environment Lighting

Drawing on the convolutional nature of the rendering equation pinpointed by Ramamoorthi [RH01], a range of BRDF inference approaches has also been proposed utilising environment illumination.

In a controlled lighting environment, Ghosh et al. [GAHO07] illuminate a material sample using a set of orthonormal Zonal Basis functions and based on these are able to infer BRDFs. An advantage of this setup is that it requires no moving parts. Similarly, although with a rotating light-arc to reduce cost and complexity, Tunwattanapong et al. [TFG+13] are capable of inferring both surface normals and reflectance of highly specular objects using Spherical Harmonics illumination. Finally Aittala et al. [AWL13] demonstrate that these concepts may be implemented using standard lab equipment such as an LCD screen and a DSLR camera, allowing capturing full spatially varying BRDFs by producing parameter maps for a 2-lobe analytical model. With this approach, we see a very practical solution to BRDF measurements.

Instead of relying on a controlled lighting environments as the approaches above, a branch of methods for inferring BRDFs under uncontrolled lighting has also been proposed. Romeiro et al. [RVZ08] are capable of estimating a data-driven (bivariate) BRDF model from a known curved surface using only a mirror light probe as a reference for the environment-lighting. Continuing their work, Romeiro and Zickler [RZ10], inspired by image-deblurring, furthermore, demonstrate that under a strong statistical prior the need for a mirror probe can be removed.

Attacking the problem at hand from a slightly different approach, Wu et al. [WZ15] use a handheld Microsoft Kinect (RGB-D) sensor in conjunction with a mirror-sphere to estimate both geometry and reflectance of everyday objects. This addresses the issue of Romeiro's work, depending on known geometry in the scene. Although the approach only produces the parameters of a simple isotropic Ward BRDF model, it proposes a very practical solution to the challenge of sampling BRDFs. In a very recent publication, Wu et al. [WWZ16] improves their approach by removing the need for a mirror-sphere and refine their position estimation. Here they optimise BRDF slices from a discrete set of observation directions and use a von Mises-Fisher (vMF) distribution fitted to Ward models

to obtain Ward model parameters. The result is an RGB-D-sensor based framework allowing full characterization of appearance, including both geometry and reflectance. Although limited to a discretized Ward-model, this approach is one way of approaching the goal of this PhD project, namely making BRDF measurements practical.

The mentioned methods produce impressive results given their relatively simple infrastructure and low acquisition time. In contrast, the mechanics behind are far from simple and most of the methods rely on delicate non-linear optimisation and require strong regularisation. As such the methods are susceptible to fall into local minima or simply fail. Furthermore, they are all based on simplified BRDFs in some sense, e.g. through a bivariate representation or an analytical model, meaning that neither of them obtain true measurements. Depending on the application, these downsides may or may not be prohibitive.

In the framework we present in this thesis, the underlying model is a linear model learned from training data. The linear model guarantees a global minimum fit and is very fast to compute (sub-seconds). Additionally, the complexity of the model scales with the amount of observations fed to it, allowing for a complexity far beyond that of analytical models.

3.2.4 Rapid Reflectomerty

A final branch of BRDF acquisition approaches that is worth mentioning is a collection of methods based on what we choose to call "rapid reflectometry". These methods are designed towards estimating BRDFs instantaneously or through a few strategical snapshots. Especially within industrial settings, these methods are applicable, where elaborate mechanical or optical infrastructures are not possible. Indeed this is the category that the major contribution of this thesis falls into, with the papers C.IV and C.VI on minimal BRDF sampling.

Hertzmann and Seitz [HS03] propose a method that both estimates shape and reflectance from 14 images with varying illumination and fixed camera. The method uses a user-defined range of synthetic reference objects and materials to match observed intensities with surface-normal and -material and are capable of achieving decent results. Related, Ren et al. [RWS+11] use a physical reference checkerboard of tiles with known reflectance. Using a video camera and a moving handheld light-source, both a surface normal map and an SVBRDF is reconstructed. Much like Hertzmann and Seitz's synthetic case, the BRDF is here represented as a linear combination of the reference materials used in the checkerboard.

Recently Aittala et al. have presented two approaches for rapidly capturing SVBRDFs using nothing more than a standard consumer mobile phone that is equipped with a camera and a flash. By capturing two near-field images with flash on and off, Aittala et al. [AWL15] are capable of estimating surface normals and the spatially varying parameters of one of the recent models proposed in [BLPW14]. In their second work [AAL16], using a convolutional neural network based texture descriptor and simplifying the reflectance model to a Blinn-Phong, Aittala et al. are able to reduce the requirement to only a single flash-lit image. Both approaches are based on recognising periodicity in texture to obtain multiple BRDF samples of every material class.
The 1- and 2-shot approaches presented by Aittala et al. also address the fundamental problem raised in this thesis, making BRDF measurements practical. They are both good solutions that each to a large extent solves the problem. As with the environment-lighting based methods, these too rely on some non-linear optimisation and strong regularisation. Currently, computation time and the risk of optimizers failing may be prohibitive, but the methods are nonetheless highly relevant.

In contrast to the approaches presented here, our framework revolves around a well posed optimization problem involving solving a linear system. As stated earlier, this formulation makes it extremely fast to compute the BRDF reconstructions and guarantees that an optimum solution is found. Furthermore, where some of the above methods rely on a reference board consisting of a small number of material samples, our method uses the entire span of the MERL database as a reference.

To sum up, it is clear that a substantial effort has been put into simplifying the task of capturing the BRDF and that there are many strategies for doing so. It is especially pleasing to observe that while this Ph.D. project was under way (in the years 2013-2016) similar research has been conducted elsewhere and competing solutions proposed. This underlines that we are indeed still dealing with a relevant field of research and that a general solution to our problem has not yet been found.

Chapter 4

Contributions

In this chapter, relevant publications made during the studies, and the contributions associated with these will be described in relation to one another. The individual publications in their entirety may be found in appendices A-F, where they are presented in their original formatting. For the sake of brevity we will not elaborate on the technical details of the publications but rather elevate and discuss primarily the contributions made and the motivation behind.

4.1 Motivation

Although chapter 3 only scratches the surface of what efforts have been put into modelling and capturing appearance, it is already apparent that this effort has indeed been vast and is driven by a large community of researchers. Even so, there is still a broad range of challenges to be solved. In the positional paper C.II [NEK+15] we take the industry's point of view and identify a range of the most pressing challenges within production that are related to appearance modelling. The common denominator found here is quality assurance and automation hereof. A great part of production quality control consists of manual visual inspection of produced parts and reflectance is often a good way of identifying surface defects. Already, as covered in chapters 2 and 3, an extensive palette of elaborate radiometric models exists, most of them very

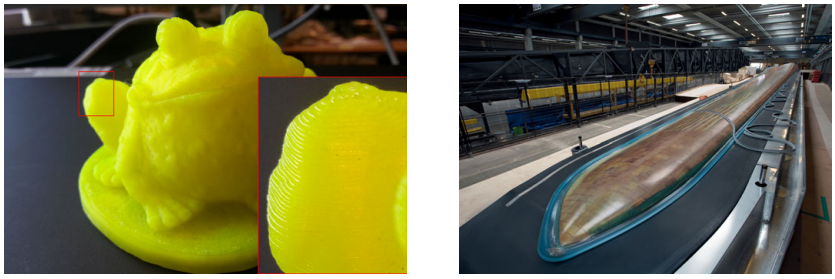

Figure 4.1: Examples of industrial fields where practical reflactance models may be applied for automatic quality assurance. Left: Additive manufacturing (3D printing) where a real-time print-quality feedback can improve overall quality. Right: Identification of surface defects in massive objects like wind turbine blades.

accurate in predicting appearance for whatever category of materials they are designed for. Their accuracy, however, comes at a cost in that their many parameters make them difficult and often impossible to fit to measured data. Without accurate low-parameter models, the task of covering the complete 4-dimensional BRDF manifold becomes impractical from an industrial point of view, wherefore C.II argues that there is an urgent need for low-parameter, or *parsimonious*, reflectance models designed for data-fitting using only a few observations. Applications of such models include e.g. real-time quality feedback in additive manufacturing (3D printing), and identification of structural defects in massive objects like wind turbine blades, both illustrated in figure 4.1. The paper C.II thus contributes by setting the tone for the future research in practical reflectance modelling and as a consequence is in many ways the foundation and motivation of the work carried out in the following.

4.2 Preliminary Investigation

As an initial explorative study, we investigated the famous MERL [MPBM03a] BRDF database. Our primary goal was here to get an understanding of how well commonly used BRDF models are able to represent measured materials, and especially where they fail. It was thus a continuation of the previous work by Ngan et al. [NDM05]. This investigation led to a number of interesting insights, one relating to the challenge of choosing a proper visualisation of the BRDFs, another relating to the choice of error-measure in the fitting process, and a third revealing unexpected material-properties for a range of the MERL materials. This initial work was published in C.I [NFCA14]. The following will

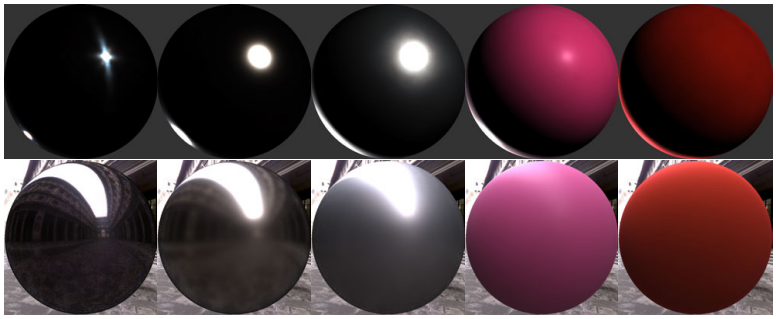

Figure 4.2: Renderings of MERL materials: chrome-steel, nickel, two-layer-silver, violet-rubber, and red-fabric2. Top row is rendered under two point-lights: an oblique front-light ($\omega_i = [1, 1, 1]$) and a grazing back-light ($\omega_i = [-1, -1, -3]$). Bottom row is rendered using ray-tracing under environment illumination using the HDR Uffizi scene [Deb98].

briefly touch upon the primary contributions from this publication.

A cornerstone in BRDF analysis is *appropriately* visualising the BRDF. Although this may sound like a trivial task (since BRDFs are usually what we plug into the rendering-pipeline), it is difficult to find a visualisation that captures all or most the nuances of a BRDF.
In essence, rendering a BRDF under a point-light corresponds to convolving it with a Dirac delta function, i.e. the image you see is, in fact, a subpart of the BRDF itself, governed by the normals of the rendered geometry. This representation is, however, unnatural for the human eye to interpret, and in addition, it is highly dependent upon the position of the light-source.
On the other hand, rendering a BRDF under environment lighting gives a visualisation that is highly interpretable to the human eye, but the convolution between environment and BRDF smoothes out any finer details of the BRDF, and thus easily hides small differences between BRDFs. In figure 4.2, the difference of these two visualisation methods is shown. In the top row, renderings are done using two point lights: a front-light at an oblique angle ($\omega_i = [1, 1, 1]$), and a back-light at a grazing angle ($\omega_i = [-1, -1, -3]$). In the bottom row, the renderings are done using ray-tracing under an HDR environment.

In C.I, we settled on using point light sources for BRDF visualisation, and it was in this context we came up with the oblique/grazing light-configuration, shown in figure 4.2, that allows visualisation of both primary- and Fresnel-highlights without the two interfering. This configuration has later proven to be a significant contribution in that while being very quickly computed it still

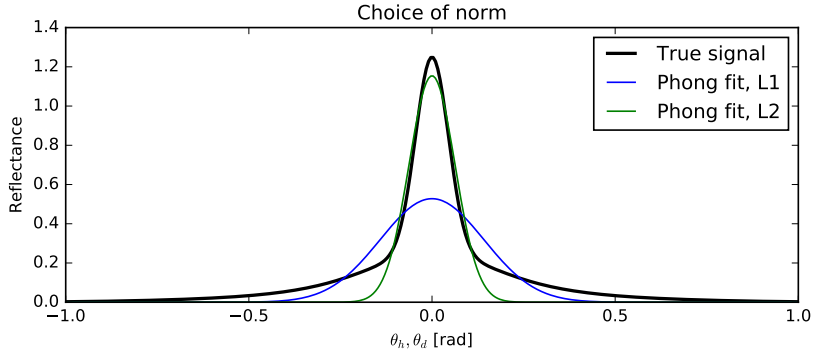

Figure 4.3: Fitting of Phong BRDF model to a fictional BRDF (black), minimizing either L^1-norm (blue) or L^2-norm (green).

gives a great insight into the shape and intensity of the two primary lobes of the BRDF. Now in relation to this contribution, we found that adding a grazing back-light reveals, surprisingly, that some materials exhibit Phong-like grazing angle reflections, while more expectedly other materials exhibit a Blinn-Phong-like behaviour which is connected to the micro-facet theory [NDM05, AMHH08]. Although we did not pursue this further, we suspect that the fact that some materials behave Phong-like is related to subsurface scattering effects. This contribution motivates for a new type of BRDF model that breaks with micro-facet-theory for grazing angles, and to open the field we introduced a compact model that allows interpolation between the Phong and Blinn-Phong models.
A final facet of the study done in C.I is the insight in the choice of error-measure when fitting analytical BRDFs to measured data. A classical choice of measure is the L^2-norm. In practice, however, where models cannot fully capture the data, the measure seems to favour the peak of the specular highlight and disregard its base which numerically is much smaller. Instead, we found that the L^1-norm does, in fact, produce a *visually* better compromise, sacrificing the peak of the highlight for a better fit to its base. A dummy example that illustrates this is shown in figure 4.3, where the Phong BRDF model is fitted to a fictional BRDF minimising either the L^1- or the L^2-norm. The contribution here lies in giving a notion of how this choice of norm affects the visual results of model-fittings.

4.3 Experimental Work

It was deemed a strategical advantage to develop in-house BRDF capture know-how and facilities, especially in relation to result validation, but also to some

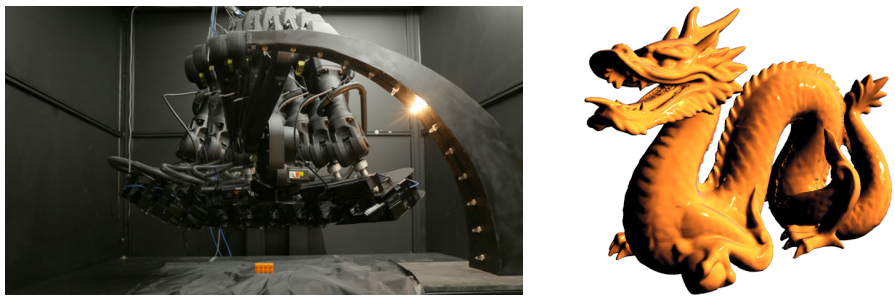

Figure 4.4: Left: Superposition of images of multiple robot poses in the DTU BRDF capture system. The surface of an orange LEGO brick is here densely sampled. Right: A rendering of the measured BRDF applied to the Stanford dragon under point light illumination.

extent to supply potential collaborators from Danish industry with precise reflectance capture capabilities. Thus, in parallel to analysing existing measured BRDF data, extensive laboratory work was carried out to build a flexible gonioreflectometer. The gonioreflectometer system revolves around a multipurpose 6-axis industrial robot. In conjunction with an illumination-arc and a turntable, the system allows automated dense sampling of BRDFs. The left image in figure 4.4 illustrates this facility where the BRDF of an orange LEGO brick is being captured, and to the right, a rendering of the resulting BRDF is shown. Further details on the system may be found in appendix G.

Only a few fully functional gonioreflectometers exist in the world. The development of this measurement system has thus contributed by supplying academia and industry with a new BRDF capture capacity. This is especially an important step for the Danish research community where we believe we are the first in Denmark capable of capturing the full 3D isotropic BRDF (and in conjunction with a turntable, even the full 4D BRDF).

The experimental work carried out has had a large role in the execution of this PhD project and has required a lot of time. Specifically we estimate that approximately half a man-year has been put into the effort by the author. Even so, as pointed out in the introduction, this effort is only indirectly credited through the validations and data captures carried out in the various publications.

4.4 A Practical BRDF Model

Paper C.V [JNLP15] is a study not related to the topic of this thesis. It was carried out in the early stages of the PhD project in collaboration with the Danish company 3-Shape and deals with 3D surface reconstruction of anatomical surfaces (ear canals) with missing data. The paper proposes a statistical reconstruction model using a prior learned from training data. The company 3-Shape produces 3D scanners for custom hearing aid fitting, where personally customised hearing aids can be 3D printed based on a 3D scan of the ear canal using their scanner. However, due to the curvature of the ear and ear canal, occlusions often occur during the optical 3D scanning, resulting in partial geometries with missing information. By learning the shape variability of the ear canal from a large training set of scanned ear canal impressions, we show in C.V that the missing information can be statistically inferred based on what known information exists. Rather than performing a smooth, e.g. Poisson-based, hole-closing, we demonstrate how a data-driven reconstruction-model can produce more anatomically correct surface reconstructions allowing better fits of the customised hearing aids.
Although the field of custom hearing aid fitting seems tangential to the work in this thesis, we have chosen to include it since it holds inspirational value by being what inspired the ideas proposed in one of our main contributions, namely the paper C.IV [NJR15].

Much like a 3D surface can be represented as a hyper-dimensional point belonging to a hyper-dimensional distribution, a densely sampled 3D BRDF can likewise be seen as a quantity in a hyper-dimensional space. Given a sufficient amount of training-data and under the assumption of normality, the hyper-dimensional distribution constituting the phenomena of BRDFs may be estimated. Hence, through covariance, given one part of a BRDF, another part may be predicted or reconstructed.
In C.IV, we demonstrate a framework for reconstructing full BRDFs from only a few measurements. The goal of this paper was to achieve a better alternative to interpolation when only a sparse set of BRDF measurements are available. The BRDF itself is a continuous manifold in 4D space, but must be quantized in some fixed number of cells in order to be digitally represented. Most often, the BRDF is sampled uniformly in a fixed grid of angles, say e.g. 5° steps, and the limit to this resolution seems today to be that of the MERL database being approximately 1°. Measurements, and especially gonioreflectometric measurements, beyond this resolution, seem infeasible. Hence, the MERL format [MPBM03a] is an appealing way of representing a BRDF, but the problem of how to best fill empty cells given a set of measurements from a coarser grid is an open question. Obviously, there is a high correlation between the bins of a discretized BRDF since it is a continuous and most often very smooth function. When we as hu-

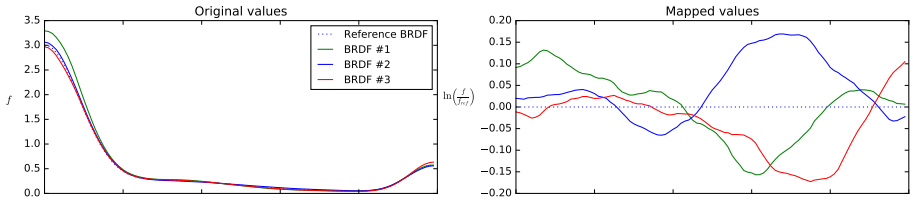

Figure 4.5: Conceptual illustration of log-relative mapping. Left are three fictional BRDFs presented together with a reference BRDF. Numerically, the dominating variation occurs around the specular highlight. To the right, the BRDFs have been mapped using the log-relative mapping, i.e. relative to the reference BRDF. Here, a lot of new variation is revealed because the general high-dynamic nature of BRDFs has been compensated for.

mans observe a material we only need a very small set of observations for us to get a clear impression of the BRDF, due to us having a lot of prior knowledge on how materials *generally* behave under varying view- and illumination-angles. It is *this* knowledge we seek to mimic in the reconstruction framework of C.IV when populating the MERL format.

An important contribution in C.IV is the use of a log-relative mapping. The BRDF has a very high dynamic range behaviour, with specular peaks being orders of magnitude larger than the diffuse components. A covariance analysis on non-mapped BRDFs [MPBM03a], will yield little insight since the vast majority of all numerical variation is contained in the specular highlights. By looking at the variation of BRDFs *relative* to some reference BRDF, a broad range of before unseen nuances appear, such as the diffuse component, Fresnel effects, and even retro-reflections. In figure 4.5, this concept is visualised by a fictional example, where hidden variation is only revealed by transforming to a log-relative domain. Performing such a preprocessing step on the MERL database before analysing variance, gives, as mentioned, a lot of new insight to the data and in addition conforms well with regions in the BRDF-domain pointed out by Burley having high significance [Bur12]. We visualise this in figure 4.6 where the first 4 principal components of the MERL database are visualised as BRDF slices [Bur12], both with and without the proposed mapping applied. As may be seen from the figure, the mapping in conjunction with principal component analysis (PCA) allows for decomposing the data into interpretable components. We find this highly interesting and see it as an important contribution.

Through the log-relative mapping and PCA a practical, linear, reflectance model has been proposed based on Tikhonov regularised least squares. This model addresses one of the primary motivators of this PhD project, namely finding a

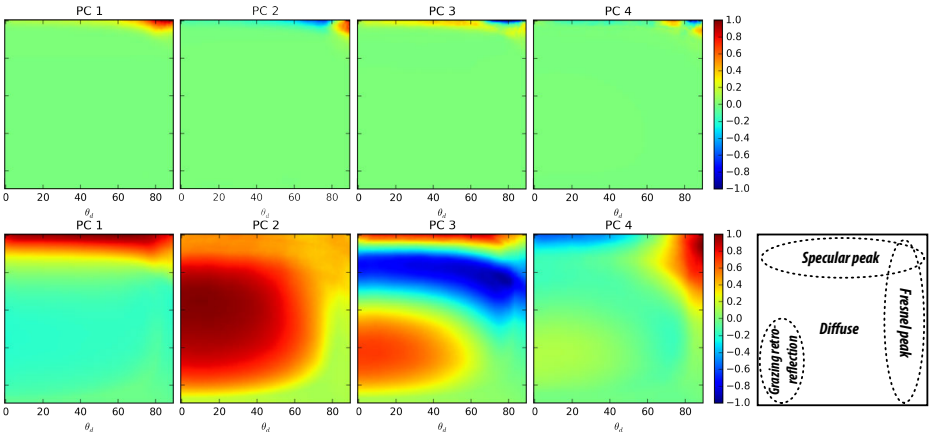

Figure 4.6: First 4 principal components of the MERL database. Top row shows the principal components of the data using no mapping. All numerical variation is seen to be contained in the specular peaks. In the bottom row the principal components of the mapped data are shown. Here it is seen that the data has been decomposed into interpretable components. An interpretation reference for the BRDF slices is presented in the bottom far right [Bur12].

practical and robust reflectance-model that is fast to compute and capable of handling sparse input data. The model takes any number of measurements and based on these synthesises the most likely BRDF they originate from.
With a well-defined engine driving the reconstruction framework, we further pursue in C.IV to determine the optimum conditions for reconstruction, i.e. what sets of light-/view-configurations combine to construct the best possible foundation for BRDF reconstruction. This analysis concludes by presenting tabulated results for the optimum configurations of light and camera for any number of reflectance samples, a great tool for practitioners. Furthermore, we make the conclusion that for most materials as little as 20 samples are in fact adequate to accurately predict the BRDF of an unknown material. With this contribution, we have demonstrated that with even a few measurements we are able to achieve a very precise representation of material appearance, much like we humans are capable of.
With the results from C.IV, designers of industrial applications may settle on any number of samples meeting their requirements (e.g. real-time processing or cost), lookup the optimum configuration for their setup, and using this configuration, obtain the best possible appearance estimate of a target. Where BRDF capture was before a slow process taking from hours to weeks, we have successfully demonstrated that it can be accurately achieved in seconds.

Pushing the results of C.IV to its limits, the paper C.VI investigates how the full CCD information may be utilised to further reduce the number of samples required to accurately capture a BRDF using our model. Most often, even though modern cameras are used, BRDFs are measured using point-measurements. I.e. a single pixel, or the mean of a small group of pixels, constitutes a radiance estimate, and the remaining information in the image is often simply discarded. Under the assumption of a flat material sample, and known extrinsic and intrinsic camera parameters, we demonstrate how the full field of view of a digital camera may be utilised to capture thousands of (highly correlated) reflectance measurements in parallel. With this, we are able to reduce the number of measurements required to faithfully capture the appearance of a sample to as little as two images. We call this approach "Near Field Capture" since it requires placing a camera so close that most of its field of view is covered by the material sample. This may be prohibitive in some applications wherefore the method is slightly less general, but we nonetheless deem it a valuable contribution to the field of practical BRDF capture.
Due to the parallelism of the Near Field Capture approach, it also allows for the capture of spatially varying BRDFs. We demonstrate a simple example of how to achieve this in C.VI, but it is indeed a vast research area in itself, requiring much further research. This further broadens the applicability of our model, and especially within industry and quality assurance, it is important to have methods capable of measuring beyond homogeneous material samples.

4.5 Applying a Practical Model

The tools described above have contributed to enabling us to effectively capture material appearance. These capabilities have been applied in a broad range of research projects. In C.III [ACDC+15] we summarise 3 ongoing projects at our lab facility, aiming to produce new high-quality datasets. The projects concern non-rigid structure from motion, multi-view stereo with known BRDF, and reproduction of scenes containing glass objects. One important facet of these datasets is the ground truth reflectance data accompanied with them. We achieve this through our robot-system in conjunction with the reconstruction framework presented above. This allows densely sampled high-quality BRDFs that are crucial for accurate appearance modelling. The need for correct radiometric reproduction is especially important in the work [SCN+16], which elaborates on one of the topics from C.III, where complex scenes containing glass objects are digitised and reproduced on a per-pixel level. In figure 4.7 we illustrate 3 examples of BRDFs captured in our facility. The materials are measured from LEGO bricks being blue, green and orange.

Figure 4.7: Rendering of 3 different LEGO materials: Blue, Green and Orange. That BRDFs were captured by of capturing system and refined through our reconstruction method.

4.6 Discussion

It is, by all means, fair to conclude that this PhD project succeeded in completing the task it set out to do, namely formulating a practical BRDF modelling framework. A contribution that was validated through several application studies. The work has pushed us to a place now where the next step is to put the methods into industrial settings. Along with the limitations already identified, this will inevitably uncover a broad range of new challenges, like e.g. robustness to variations in surface normals or light-contamination, which will be discussed in the following in the form of suggestions for future work. The proposed future work primarily revolves around our data-driven reconstruction framework and how to improve it, as this is where we see the greatest potential.

Practical testing The work done in the thesis has pushed us to a place now where one obvious next step is to put the methods into practice. This will inevitably uncover a long range of new challenges, like e.g. robustness to variations in surface normals or light-contamination. We are currently taking the first steps towards this with multiple industrial collaborators and it will be an active field of research in our section for the coming years.

Additional data Clearly, the major disadvantage of the proposed reconstruction framework is its dependency on a large set of training data. Although the MERL database covers a broad range of material samples it definitely does not cover the entire span of material appearance. Also, the framework currently only models isotropic materials and the entire category of anisotropic materials is yet to be incorporated into the framework. Although very difficult to acquire, the current model needs more training data in order to capture a wider span of appearance. One shortcut may be to simulate additional training data using ad-

vanced parametric models with randomly chosen parameters, the cost, however, will be that the model becomes biased towards synthetic observations.

Model reiteration Although the linear model and data-mapping used in the reconstruction framework have proven to work well, there may be better models or mappings for the task. A clear disadvantage of the current method is its dependency on training data. If possible, a parsimonious analytical BRDF model - perhaps linear under e.g. a log-relative mapping - would be preferred over the data-driven. Future research could look into such modifications.

Integration into 3D estimation frameworks Extending existing 3D estimation frameworks to also estimate a BRDF is also of great interest, as the current state of the art relies on very simple BRDF models. An example could be a structured light scanner where the projector/camera configuration causes a fixed θ_d, but model geometry causes variations in the surface normal, creating multiple samples across the θ_h, ϕ_d plane. A challenge is here to be robust towards noisy normal estimates and be able to handle spatial variance in the BRDF. We are currently investigating the possibilities of this in our lab.

Interfacing The parameters of the linear BRDF model corresponds to weights of the principal components of the dataset. These weights are a very compact representation, but not usable in standard 3D content creation tools. Creating plugins allowing the use of either manually defined or measured weights in standard software would make our results much more useful to practitioners.

Model parameter Estimation Alternatively to implementing the data-driven model in standard 3D content creation tools, an investigation could be done in how to convert PC-weights into parameters used by the standard analytical BRDF models. As is identified in C.IV, the individual components are linked to different parts of the BRDF, e.g. diffuse, specular, Fresnel, etc. Devising a mapping from PC-weights to e.g. Torrance-Sparrow model parameters would be very interesting and could either be used as is or as an initial guess to a refined model-fitting.

Chapter 5

Conclusions

This thesis has presented the research carried out during the past 3 years' Ph.D. studies, targeted at making appearance modelling practical. This has high relevance in many fields, including e.g. computer graphics, product visualisation, and production quality inspection. In this effort, a range of scientific contributions have been proposed, addressing various aspects of the challenge at hand.

The research carried out has to a large extent been governed by an explorative approach, themed on bringing practicality to the field concerning material appearance. As such, the path travelled has not been laid out in advance but is a direct consequence of the findings we did under way. It is to this extent pleasing to find that a common thread indeed is running through the publications made.

The world needs practical BRDF models. The full 4D BRDF manifold is simply too vast to work with practically. We see this need in multiple very different fields and in paper C.II we bring 4 concrete and diverse examples that illustrate a need for parsimonious, applicable, BRDF models in industry.
We set forth a quest to address this, taking offset in an investigation of where analytical models come short when comparing to real, measured, data. This was dealt with in C.I. In parallel, we started developing a laboratory facility, revolving around our industrial robot, making us capable of measuring our own BRDFs . In appendices G-H technical notes regarding our system are presented and in C.III we utilize our facilities to capture novel datasets. This effort in

itself has been a huge task that has given an invaluable insight and the resulting facility will be a pivot in much of our future research.

In the search for a flexible low-parameter model, and inspired by our research on mesh-surface reconstruction presented in C.V, we came up with a data-driven BRDF model based on the MERL database. The paper C.IV presents this model, and an important contribution in this publication is the use of a log-relative domain in which the data-driven model is both linear and compact. The model further inspired the analysis of, and conclusion on, which measurement-directions are in fact the optimum in practical systems where the number of samples is limited. Pushing this approach to its limit, we demonstrated in C.VI that using the full spatial information from a camera placed close to a sample, we call it the near-field, allows for reconstructions of materials using as little as two images, i.e. it enables practical real-time appearance acquisition.

The tools developed have contributed to enabling us to produce new datasets of BRDFs. In addition to the ones presented in C.III, an additional unique dataset of transparent objects accompanied with ground truth geometry and material properties for full scenes has been created for [SCN+16].

The above-mentioned publications have all given new insights to their respective areas of interest. In the following, we would like to summarise what we see as the most important highlights of the project:

- Explored the challenges regarding fitting existing models to measured data (C.I).
- Proposed a simple extension to the Phong/Blinn-Phong model, allowing for better modelling of Fresnel effects (C.I).
- Identified and initiated a dialogue in the scientific community regarding the need for parsimonious BRDF models (C.II).
- Developed a statistical reconstruction framework for BRDFs (C.IV).
- Derived optimal sampling directions of BRDFs (C.IV).
- Demonstrated that BRDFs can be captured quickly using only a few measurements (C.IV & C.VI).
- Demonstrated that spatial information can be utilised to reduce the required amount of samples even further (C.VI).
- Employed our findings to produce novel datasets (C.III & [SCN+16]).
- Developed a laboratory facility for accurately measuring BRDFs.

Based on the above, we are happy to conclude that we to a great extent achieved the task set out to do, namely devising a low-parameter data-driven BRDF model, and using this, making appearance acquisition more practical.

Appendix A

Contribution C.I: Addressing Grazing Angle Reflections in Phong Models

Addressing Grazing Angle Reflections in Phong Models

Jannik Boll Nielsen Jeppe Revall Frisvad Knut Conradsen Henrik Aanæs
Technical University of Denmark

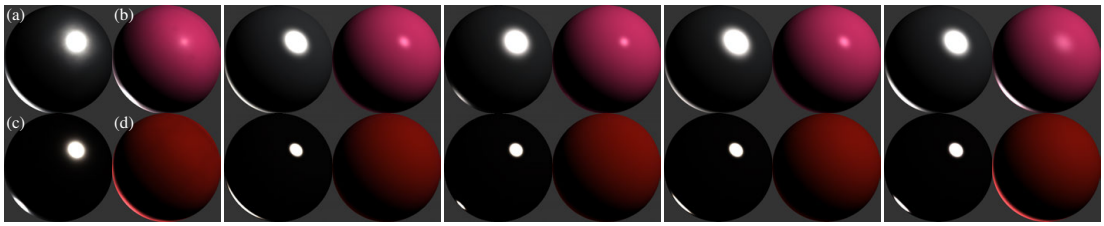

Figure 1: *Measured and fitted BRDFs of the materials: (a) two-layer-silver, (b) violet-rubber, (c) nickel, and (d) red-fabric2. We illuminate the rendered spheres by a directional light at glancing incidence (NE hemisphere) and one at grazing incidence (SW hemisphere). Our new Phong model variant is a combination of the Phong and Blinn-Phong variants, which achieves a better fit of the measured BRDFs at grazing angles. Note that the reflectance at grazing angles is Phong-like for some materials (a) and Blinn-Phong-like for others (c).*

The Phong illumination model is used extensively as it is simple with few parameters. It is however often challenging to fit such a single lobed model to the bidirectional reflectance distribution function (BRDF) of a real material, especially at grazing angles (Fig. 1). The fitting issues are in shortcomings of the model, in choosing error function, and in initial guess sensitivity [Matusik et al. 2003]. In previous work [Ngan et al. 2005], these issues were bypassed by using two specular lobes, by ignoring very grazing angles ($>80^\circ$), and, in cases of unsatisfactory fitting quality, by manually restarting the fitting procedure with a different initial guess. In this work, we also fit Phong models to the BRDFs measured by Matusik et al. [2003], but we focus on the difficult grazing angles. Our result is a new Phong variant that fits better to a broader range of materials, and, for this model, we address the above-mentioned fitting issues.

Common Phong Model Variants. Our model is a mixture of the modified Phong model (f_r^{P}) and the modified Blinn-Phong model (f_r^{BP}). These are defined by [Akenine-Möller et al. 2008]

$$f_r^{\mathrm{P}}(\vec{\omega}_i,\vec{\omega}_o) = \frac{\rho_d}{\pi}+\rho_s\frac{s+2}{2\pi}(\vec{\omega}_r\cdot\vec{\omega}_o)^s \quad (1)$$

$$f_r^{\mathrm{BP}}(\vec{\omega}_i,\vec{\omega}_o) = \frac{\rho_d}{\pi}+\rho_s\frac{s+8}{8\pi}(\vec{\omega}_h\cdot\vec{n})^s\ , \quad (2)$$

where ρ_d and ρ_s are diffuse and specular reflectance parameters and s is a shininess parameter, $\vec{\omega}_i$ is the direction toward the light source, $\vec{\omega}_o$ is the direction toward the viewer, $\vec{\omega}_r = 2(\vec{\omega}_i\cdot\vec{n})\vec{n}-\vec{\omega}_i$ is the direction of the light reflected perfectly around the surface normal $\vec{n}$, and $\vec{\omega}_h = (\vec{\omega}_i+\vec{\omega}_o)/|\vec{\omega}_i+\vec{\omega}_o|$ is the half-vector. The specular highlights produced by the two variants (1–2) are different, especially at grazing angles (Fig. 1).

Comparison to Measured BRDFs. When we fit the Phong models (1–2) to measured BRDFs using nonlinear optimization, we find examples where the Blinn-Phong variant (2) has the smallest error (Fig. 1c), but also examples where the Phong variant (1) has the smallest error (Fig. 1a). While the Blinn-Phong-like reflectance is probably due to surface microfacets [Ngan et al. 2005], we believe that the Phong-like reflectance is probably due to subsurface scattering. Thus, although the modified Phong model in theory might seem physically inappropriate, it does seem to mimic the grazing angle reflectance of some real materials.

As in previous work [Ngan et al. 2005], we observe that it is important to multiply the specular reflectance ρ_s by the Fresnel reflectance $R_F(\vec{\omega}_i\cdot\vec{\omega}_h,\eta)$ [Akenine-Möller et al. 2008], where η is the refractive index of the material. This is necessary to model the effect that the reflectance in general is significantly stronger at grazing angles than at glancing angles (Fig. 1).

Our Phong Model Variant. The existence of both Phong-like, Blinn-Phong-like, and mixed reflectance behaviour in real-world materials suggests that a combination could be useful. We thus propose a model with interpolation of the two different cosines:

$$f_r^{\mathrm{new}}(\vec{\omega}_i,\vec{\omega}_o) = \frac{\rho_d}{\pi}+k_s\big((1-\alpha)(\vec{\omega}_r\cdot\vec{\omega}_o)+\alpha(\vec{\omega}_h\cdot\vec{n})^4\big)^s\ , \quad (3)$$

where $\alpha\in[0,1]$ is the interpolation parameter. For simplicity, the specular coefficient k_s replaces the specular reflectance ρ_s multiplied by the energy conservation term $\frac{s+x}{x\pi}$. We multiply k_s by R_F to include Fresnel reflectance. The Blinn-Phong cosine is raised to the 4th power, as the Phong exponent is roughly 4 times stronger than the Blinn-Phong exponent [Akenine-Möller et al. 2008].

Effectively, this model enables us to control and shape the reflectance at grazing angles of incidence. We can thus approximately accommodate both grazing angle reflectance due to subsurface scattering and due to microfacets in a simple Phong model.

Fitting Results and Observations. The Euclidean norm (L^2) is not a good error function as it primarily fits the cosine lobe to the tops of the specular highlights. We solve this issue by using the L^1 norm as it roughly results in a fitting to the base of the specular highlights. Visually, we find the L^1 results more reasonable. We use consecutive optimizations to obtain a fitting procedure which is not initial guess sensitive. Our procedure is: (i) optimize only ρ_d and k_s, (ii) optimize only s and α (and η), and (iii) optimize s, α, and k_s (and η). This gives robust convergence for all the BRDFs measured by Matusik et al. [2003]. We present four examples of such fits in Fig. 1.

References

AKENINE-MÖLLER, T., HAINES, E., AND HOFFMAN, N. 2008. *Real-Time Rendering*, third ed. A K Peters, Natick, MA.

MATUSIK, W., PFISTER, H., BRAND, M., AND MCMILLAN, L. 2003. A data-driven reflectance model. *ACM Transactions on Graphics (Proc. of ACM SIGGRAPH 2003) 22*, 3, 759–769.

NGAN, A., DURAND, F., AND MATUSIK, W. 2005. Experimental analysis of BRDF models. In *Rendering Techniques 2005 (Proc. of Eurographics Symposium on Rendering)*, 117–126.

Permission to make digital or hard copies of part or all of this work for personal or classroom use is granted without fee provided that copies are not made or distributed for profit or commercial advantage and that copies bear this notice and the full citation on the first page. Copyrights for third-party components of this work must be honored. For all other uses, contact the Owner/Author.
Copyright is held by the owner/author(s).
SA'14 Poster, Dec 03-06 2014, Shenzhen, China
ACM 978-1-4503-2792-3/14/12.
http://dx.doi.org/10.1145/2668975.2668979

DTU Compute
Department of Applied Mathematics and Computer Science

Addressing Grazing Angle Reflections in Phong Models

Jannik Boll Nielsen, Jeppe Revall Frisvad, Knut Conradsen, Henrik Aanæs

Technical University of Denmark

Bidirectional Reflectance Distribution Functions

In this work, we fit Phong models to the BRDFs measured by Matusik et al. [2], but in contrast to previous work we focus on the difficult grazing angles. Our result is a new Phong variant that fits better to a broader range of materials.

- Reflection vector, $\vec{\omega}_r = 2(\vec{\omega}_i \cdot \vec{n})\vec{n} - \vec{\omega}_i$
- Half vector, $\vec{\omega}_h = (\vec{\omega}_i + \vec{\omega}_o)/|\vec{\omega}_i + \vec{\omega}_o|$
- Surface normal, $\vec{n}$
- Illumination direction, $\vec{\omega}_i$
- Observer direction, $\vec{\omega}_o$

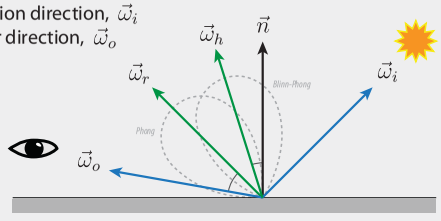

Observations from the MERL database

Inspecting the MERL database of measured BRDFs reveals that some materials exhibit Phong-like and others Blinn-Phong-like behaviour, alhough only Blinn-Phong is assumed physically plausible.

Phong-like Behavior:

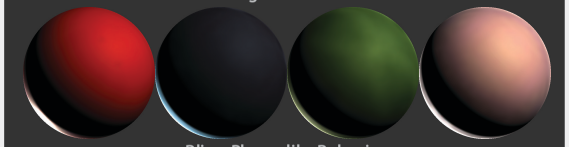

Blinn-Phong-like Behavior:

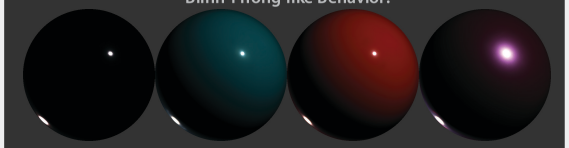

We suspect the Phong-like behavior is caused by sub-surface scattering in the materials.

Fresnel Coefficient

Compared to many MERL-BRDFs, the intensity of grazing angle reflectance in Phong-models is way too low. In order to boost the intensity at grazing angles, the Fresnel reflectance coefficient, $R_F(\vec{\omega}_i \cdot \vec{\omega}_h, \eta)$ [1], may be used.

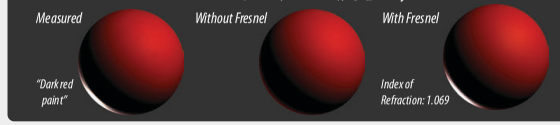

Fitting to MERL

Fitting analytical models to densely sampled BRDFs is not trivial [3]. We have found that the following procedure results in good convergences for all materials in the MERL database.

1) Optimize only ρ_d and k_s
2) Optimize only s and α (and η)
3) Optimize s, α and k_s (and η)

Vi minimize the L¹-norm as this corresponds to fitting to the base of the specular peaks.

Phong Model [1]

$$f_r^{\mathrm{P}}(\vec{\omega}_i, \vec{\omega}_o) = \frac{\rho_d}{\pi} + \rho_s \frac{s+2}{2\pi}(\vec{\omega}_r \cdot \vec{\omega}_o)^s$$

- Elongated highlight at glancing angles
- Wide highlight at grazing angles
- Claimed non-physical

Blinn-Phong Model [1]

$$f_r^{\mathrm{BP}}(\vec{\omega}_i, \vec{\omega}_o) = \frac{\rho_d}{\pi} + \rho_s \frac{s+8}{8\pi}(\vec{\omega}_h \cdot \vec{n})^s$$

- Circular highlight at glancing angles
- Condenced highlight at grazing angles
- Supported by microfacet theory

Combining Phong and Blinn-Phong

In order to obtain a BRDF-model capable of producing both broad and narrow grazing angle reflections, we propose an interpolation of the two simple BRDF models:

$$f_r^{\mathrm{new}}(\vec{\omega}_i, \vec{\omega}_o) = \frac{\rho_d}{\pi} + k_s\big((1-\alpha)(\vec{\omega}_r \cdot \vec{\omega}_o) + \alpha(\vec{\omega}_h \cdot \vec{n})^4\big)^s$$

With α being an interpolation coeficient, interpolating between the Phong and Blinn-Phong cosines. Effectively this allows shaping of the grazing angle reflections:

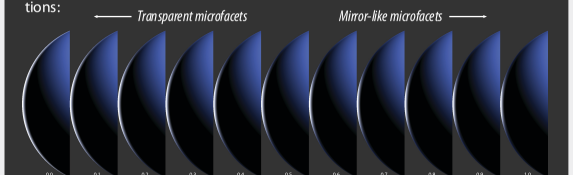

Results

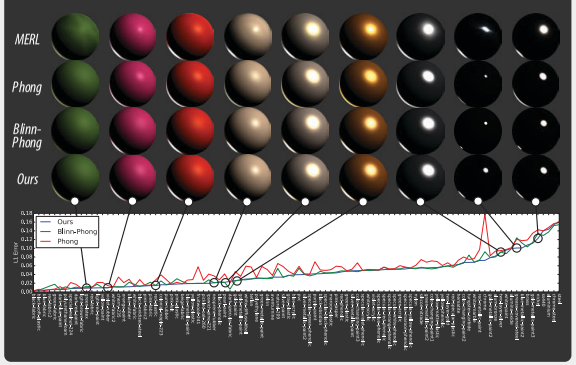

[1] AKENINE-MÖLLER, T., HAINES, E., AND HOFFMAN, N. 2008. *Real-Time Rendering*, third ed. A K Peters, Natick, MA.

[2] MATUSIK, W., PFISTER, H., BRAND, M., AND MCMILLAN, L. 2003. A data-driven reflectance model. *ACM Transactions on Graphics (Proc. of ACM SIGGRAPH 2003)* 22, 3, 759–769.

[3] NGAN, A., DURAND, F., AND MATUSIK, W. 2005. Experimental analysis of BRDF models. *In Rendering Techniques 2005 (Proc. of Eurographics Symposium on Rendering)*, 117–126.

Appendix B

Contribution C.II: Quality Assurance Based on Descriptive and Parsimonious Appearance Models

Material Appearance Modeling Workshop (2015), pp. 1–4
Holly Rushmeier and Reinhard Klein (Editors)

Quality Assurance Based on Descriptive and Parsimonious Appearance Models

J. B. Nielsen, E. R. Eiriksson, R. L. Kristensen, J. Wilm, J. R. Frisvad, K. Conradsen, H. Aanæs

Technical University of Denmark

Abstract

In this positional paper, we discuss the potential benefits of using appearance models in additive manufacturing, metal casting, wind turbine blade production, and 3D content acquisition. Current state of the art in acquisition and rendering of appearance cannot easily be used for quality assurance in these areas. The common denominator is the need for descriptive and parsimonious appearance models. By 'parsimonious' we mean with few parameters *so that a model is useful both for fast acquisition, robust fitting, and fast rendering of appearance. The word 'descriptive' refers to the fact that a model should represent the main features of the acquired appearance data. The solution we propose is to reduce the degrees of freedom by greater use of multivariate statistics.*

Categories and Subject Descriptors (according to ACM CCS): I.4.1 [Image Processing and Computer Vision]: Digitization and Image Capture—Reflectance

1. Introduction

Much work has gone into formulating radiometric models of surface reflectance for believable photorealistic rendering of material appearance. This has led to a number of physically plausible models with intuitively meaningful parameters that are appropriate for direct manipulation [MHH*12]. In this positional paper, we discuss the use of appearance models in a different context, namely in quality assurance of physical and digital products. We argue that this area of application requires models with few parameters, or parsimonious models. Through our example use cases, we further argue that there is a significant need for such parsimonious models, and that effort should be put into their development.

The need for parsimonious radiometric models manifests itself when we need to estimate the radiometric properties of surfaces in practice, e.g. when doing industrial inspection to ensure that the products have the specified visual properties, or when we would like to acquire photorealistic models from images. In such cases, the number of measurements is limited, maybe 5 to 20 per surface patch. This should be seen in light of the number of measurements needed to reliably estimate a general bidirectional reflectance distribution function (BRDF). A BRDF is modeled by a 4D manifold and is typically measured using a spherical gantry (a gonioreflectometer). This means that a very large number of measurements is required, which in many cases is practically infeasible.

According to the philosophy associated with Occam's razor, the formulation of descriptive and parsimonious models will also force us to better model and understand the underlying radiometric phenomena. Thus, in the end, our models should hopefully lead to physically plausible models with few intuitively meaningful parameters as is needed for the more classical applications of appearance models. We believe that it is possible to make large advances in this direction, meaning that the task of formulating parsimonious models does not seem to be a frugal one.

2. Relating to existing models

Previous work has shown that the classical empirically and physically based computer graphics reflectance models cannot fit all measured reflectance data well [NDM05]. This has led to a quest for models that provide a better fit [BSH12, LKYU12]. The cost of a better fit is an increase in the number of model parameters, and the simplest model (the Phong model [Pho75]) already has two parameters per color band and one parameter to describe the material glossiness. As such, the simplest model requires at least seven measurements although ideally many more to robustly fit measured reflectance data. In applications of real-time reflectance acquisition, this quickly becomes infeasible.

The fitting of most parametric models is far from triv-

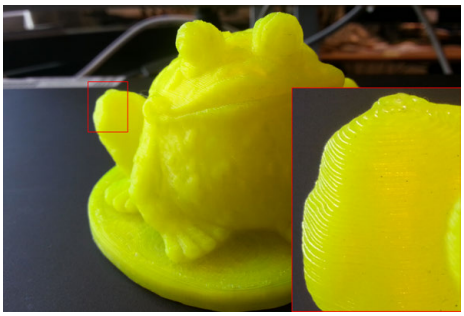

Figure 1: *Frog printed out of Polylactic acid (PLA) plastic using a Fused Deposition Modeling (FDM) printer.*

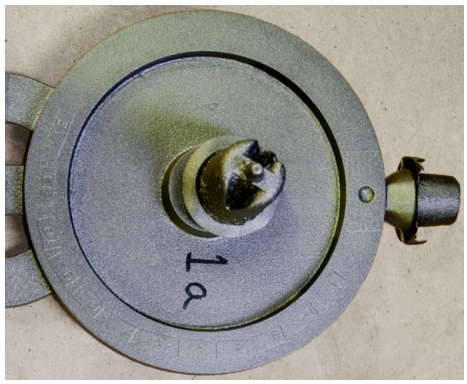

Figure 2: *Example of iron casting [VSRT15], where the mould has introduced a surface roughness affecting the visual appearance of the product. Image is courtesy of Nikolaj Kjelgaard Vedel-Smith.*

ial. Major challenges include determining what optimizers to use and what objective functions they should minimize. For the latter, various suggestions have been proposed including L_1 minimization [NFCA14] and log-transformation with cosine-weighting of observed data [NDM05]. To address the issues of non-linear model fitting, alternative approaches have been proposed where reflectance is modeled by linear combinations of basis functions. Suggestions to basis functions include spherical harmonics [WAT92], wavelets [SS95], and densely sampled reference reflectances [MPBM03]. The advantage here is that fitting models to observations becomes extremely easy as this corresponds to solving a linear system of equations. The challenge however, which is an unsolved problem, is identifying a *sparse* set of basis functions that model a wide variety of material appearances well. We need, as a community, to work on this.

3. Relevant Cases

To argue relevance, we now describe four cases where we have identified that the current radiometric models or acquisition methods simply do not suffice. The cases are (1) additive 3D printing, where the 3D microstructures caused by the printing process cannot be modeled well by standard reflectance models; (2) real-time monitoring of reflectance in metal production; (3) estimation of surface reflectance on massive objects (wind turbine blades); and (4) reflectance models to be used with 3D scanners to allow simultaneous acquisition of geometry and appearance. These are all problems that cannot be solved by conventional methods.

3.1. Additive Manufacturing

For the past decade, additive manufacturing (3D printing) has been an accepted production method. Today, it is possible to manufacture products in multiple materials ranging from soft polymers to metals [WC13]. A rapidly growing market of internet printing services is emerging (shapeways.com and i.materialise.com, for example) where users can upload their own 3D models for printing. Fast and realistic material rendering is of great interest to these types of services, allowing users to previsualize the printed outcome of their models prior to committing to purchase. However, accurately obtaining these radiometric models is a challenge. The layer-like nature of the printing process yields surface artifacts, the most prominent known as the 'staircase effect' which drastically alters material appearance for some materials. Visually, we observe this as a local anisotropy, often correlated with the surface curvature, see Figure 1. Thus the printing process itself must be considered when producing an accurate model of the printed appearance.

Radiometric model acquisition also has an application in the quality assurance aspect of additive manufacturing. So far, most effort has been placed on in-line geometric verification of parts [HNRP14, PH14] and color verification [EPA15]. These optical systems capture each and every layer during the print in order to verify its correctness. Combinations of such systems along with rapid radiometric acquisition could prove beneficial as slight deviations from the material optical properties could indicate failure due to e.g. overheating (color change) or structural collapses (surface normal orientation). In essence, we need to verify the quality of 3D prints, but practical constraints limit the number of measurements that it is possible to acquire.

3.2. Metal Casting

Metal casting is still an actively used production method. Casting allows for the creation of seamless and rigid structures in various materials. However, post machining of said

Figure 3: *Wind turbine blade right after molding.*

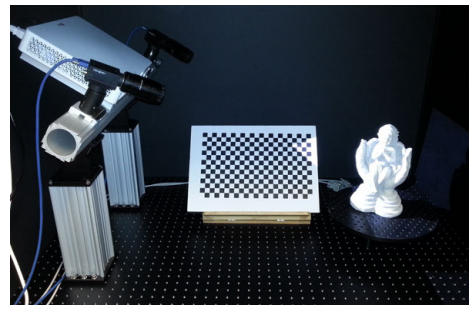

Figure 4: *Structured Light system scanning a statue.*

objects is in many cases required due to the rough surface texture resulting from the casting process, see Figure 2. Measurements of surface roughness parameters are useful for industry and academia in order to optimize the casting procedure as it is related to the overall cast quality. Obtaining surface roughness parameters from optical reflectance is thus of great interest and is an active field of research [NTH13]. As in the case of additive manufacturing, we see a scenario where practical constraints limit the feasible number of measurements, thus creating a demand for accurate parsimonious reflectance models that enable robust fitting.

3.3. Wind Turbine Blades

One of the most important steps in quality inspection of wind turbine blades is to find transverse folds in their longitudinal fiberglass mats. The longitudinal mats run all the way from the root of the blade to the tip and provide the blade with the bulk of its rigidity and strength. Multiple layers of longitudinal mats are needed to provide the necessary strength, and the load must be evenly distributed across the layers. If one layer has a fold, that layer will be tightened harder than the rest of the layers, thus carrying more load when the blade is being operated. Over time, this increased load will wear the fold-layer down to the point where it snaps and thereby compromises the entire structure of the blade. Usually, this sudden release of tension creates a force on the remaining layers so that these also snap. The result is a broken blade.

Before painting, wind turbine blades are translucent due to their composition of transparent epoxy resin and fiberglass (see Figure 3). A fold on a fiberglass mat will create a bulge beneath the surface which alters the optical properties of the material. Currently, specially trained quality engineers shine powerful light parallel to the surface and look for changes in the reflections. An accurate automated measure of surface BRDFs could increase the efficiency and accuracy of the quality assurance by transforming the fold inspection from a qualitative process into a quantitative process.

3.4. Creating 3D Content

Optical 3D scanners are actively used throughout various fields such as archaeology, biology, production, entertainment, medicine, and art. All aiming to capture high resolution 3D models in a relatively short amount of time. However, in order to produce realistic and applicable digitization of scanned objects, their radiometric properties must also be determined. Many commercial systems provide the ability to capture surface textures in order to provide more aesthetically pleasing models, but are often limited to assuming Lambertian behaviour or at most a simple parametric model, such as Phong [Pho75] or Ward [War92]. As indicated in Section 2, these models fail to fit the reflectance properties of many real-world materials. Trouble is that we cannot improve the fit by increasing the number of model parameters as we need to acquire reflectance properties at speeds comparable to the 3D scanning process. This underlines the need for descriptive and parsimonious appearance models.

An interesting property of structured light (SL) scanners is the fixed angle between observer (camera) and lightsource (SL projector). This is illustrated in Figure 4. Using only existing components of such a setup thus poses a constraint on the observable regions in the BRDF domain. Likewise, the geometry also dictates illumination and view directions relative to the surface normal. Hence, again we see a practical limitation on the available observations, which causes a demand for parsimonious models that enable robust fitting.

4. Discussion

From the above, it is evident that there are number of relevant cases where today's methods do not suffice. We believe that the problems in the mentioned cases can be solved, but that they require us to approach material appearance modeling from a new angle. Specifically, we believe that data analysis and multivariate statistics should be involved more than we see it today, and also that we should introduce stronger priors on the data. Such tools are necessary to considerably

reduce the degrees of freedom in the problems. A solution of this kind will greatly contribute to streamlining and automating the entire production pipeline, which is an essential part of agile product development.

Conclusively, we would like to reiterate that descriptive and parsimonious reflectance models seem indispensable if we are to use material appearance models in the context of quality assurance of printed, molded, and digitized products.

References

[BSH12] BAGHER M. M., SOLER C., HOLZSCHUCH N.: Accurate fitting of measured reflectances using a Shifted Gamma micro-facet distribution. *Computer Graphics Forum (Proceedings of EGSR 2012) 31*, 4 (June 2012), 1509–1518. 1

[EPA15] EIRIKSSON E., PEDERSEN D., AANAES H.: Predicting color output of additive manufactured parts. In *Proc. ASPE Spring Topical Meeting on Achieving Precision Tolerances in Additive Manufacturing (26-29 April 2015, Raleigh, North Carolina, USA)* (2015), pp. 95–99. 2

[HNRP14] HANSEN H., NIELSEN J., RASMUSSEN J., PEDERSEN D.: Performance verification of 3d printers. In *Proc. ASPE Spring Topical Meeting on Dimensional Accuracy and Surface Finish in Additive Manufacturing (13-16 April 2014, Berkeley, CA, USA) pp* (2014), pp. 104–107. 2

[LKYU12] LÖW J., KRONANDER J., YNNERMAN A., UNGER J.: BRDF models for accurate and efficient rendering of glossy surfaces. *ACM Transactions on Graphics 31*, 1 (January 2012), 9:1–9:14. 1

[MHH*12] MCAULEY S., HILL S., HOFFMAN N., GOTANDA Y., SMITS B., BURLEY B., MARTINEZ A.: Practical physically based shading in film and game production. In *ACM SIGGRAPH 2012 Courses* (2012), no. 10. 1

[MPBM03] MATUSIK W., PFISTER H., BRAND M., MCMILLAN L.: Efficient isotropic BRDF measurement. In *Rendering Techniques (Proceedings of EGSR 2003)* (June 2003), pp. 241–247. 2

[NDM05] NGAN A., DURAND F., MATUSIK W.: Experimental analysis of BRDF models. In *Rendering Techniques (Proceedings of EGSR 2005)* (2005), pp. 117–126. 1, 2

[NFCA14] NIELSEN J. B., FRISVAD J. R., CONRADSEN K., AANÆS H.: Addressing grazing angle reflections in phong models. In *SIGGRAPH Asia 2014 Posters* (2014), ACM, p. 43. 2

[NTH13] NWAOGU U. C., TIEDJE N. S., HANSEN H. N.: A non-contact 3d method to characterize the surface roughness of castings. *Journal of Materials Processing Technology 213*, 1 (2013), 59–68. 3

[PH14] PEDERSEN D., HANSEN H.: Comparability of the performance of in-line computer vision for geometrical verification of parts, produced by additive manufacturing. In *Proc. ASPE Spring Topical Meeting on Dimensional Accuracy and Surface Finish in Additive Manufacturing (13-16 April 2014, Berkeley, CA, USA) pp* (2014), pp. 179–183. 2

[Pho75] PHONG B. T.: Illumination for computer generated pictures. *Communications of the ACM 18*, 6 (1975), 311–317. 1, 3

[SS95] SCHRÖDER P., SWELDENS W.: Spherical wavelets: Efficiently representing functions on the sphere. In *Proceedings of the 22nd annual conference on Computer graphics and interactive techniques* (1995), ACM, pp. 161–172. 2

[VSRT15] VEDEL-SMITH N. K., RASMUSSEN J., TIEDJE N. S.: Thermal distortion of disc-shaped ductile iron castings in vertically parted moulds. *Journal of Materials Processing Technology* (2015), 262–271. 2

[War92] WARD G. J.: Measuring and modeling anisotropic reflection. In *SIGGRAPH 92* (1992), pp. 265–272. 3

[WAT92] WESTIN S. H., ARVO J. R., TORRANCE K. E.: Predicting reflectance functions from complex surfaces. *Computer Graphics (Proceedings of ACM SIGGRAPH 92) 26*, 2 (July 1992), 255–264. 2

[WC13] WOHLERS T., CAFFREY T.: Additive manufacturing and 3d printing state of the industry annual worldwide progress report. 2014. *Wohlers Associates* (2013). 2

Appendix C

Contribution C.III: Our 3D Vision Data-Sets in the Making

Our 3D Vision Data-Sets in the Making

H. Aanæs[1] K. Conradsen[1] A. Dal Corso[1] A. B. Dahl[1] A. Del Bue[2] M. Doest[1]
J. R. Frisvad[1] S. H. N. Jensen[1] J. B. Nielsen[1] J. D. Stets[1]
G. Vogiatzis[3]
[1] Technical University of Denmark [2] Istituto Italiano di Tecnologia [3] Aston University, UK

1. Introduction

Over the previous years, we have at the Section for Image Analysis and Computer Graphics at the Technical University of Denmark been working on generating high quality data sets for computer vision via our lab setup using a 6-axis industrial robot. This has provided a new data set aimed at feature matching [1, 4], and two data sets aimed at multiple view stereo [14, 16]. The resulting data sets are publicly available via `http://roboimagedata.compute.dtu.dk/`.

The evaluation of computer vision algorithms on these data sets has provided useful insights on realistic scenarios by setting a rigorous framework for evaluation. The results of these efforts have been well received by the community and the hardware and software platform associated with the robot is now well developed. We are currently in the process of making three new data sets aimed at 3D vision, with a special focus on the more challenging aspects, such as radiometry and the modelling of non-rigid objects. The construction of these data sets all leverage on our robotic setup's ability to produce ground truth camera and surface geometry, as briefly outlined in Section 2, and there is a great deal of commonality in the making of the data sets.

This abstract describes our current ongoing work on this data set construction for 3D vision. The data sets include:

1. A direct extension of our large multiple view stereo (MVS) data set [14], where we are now including transparent and semi transparent objects into the scenes, Section 3. A challenge in doing this is getting the ground truth geometry of the transparent objects.

2. A data set addressing the radiometric challenges in 3D vision as presented in Section 4 where we aim at extending our MVS data set by explicitly measure the bidirectional reflectance distribution function (BRDF) of the surfaces. This will have the additional feature to finally give a data set for evaluating photometric stereo with a ground truth.

3. An extension of our data set on feature matching to evaluate these algorithm with non-rigid objects, (Section 5) where we use actuators to make stop motion 3D data sets. This data set will also evaluate Non-rigid Structure from Motion (NRSfM) with realistic objects.

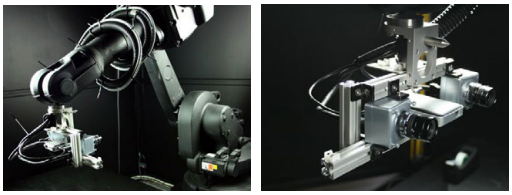

Figure 1. Photos of the 6-axis industrial robot mounted with two cameras and a projector. Cameras allow for MVS, and in conjunction with the projector SL provides ground truth point clouds.

2. Brief System Overview

Our experimental setup, cf. [1], is built around a 6-axis ABB IRB 1600 industrial robot, providing a flexible, precise, and highly repeatable camera pose. The robot is mounted with two Point Grey Grasshopper3 3376×2704 8-bit RGB cameras and a projector (for previously published datasets the cameras were 1600×1200 8-bit Point Grey Scorpion cameras). From each position ground truth surface point clouds are obtained using structured light (SL), and stereo images with a 32 cm baseline are captured with the camera pair. Five individually controlled 6500K LED tube lights allow for soft natural illumination of scenes from varying directions. Figure 1 shows the robot.

Previous evaluations of our system [14] have shown that the ground truth samples obtained through SL have good accuracy with a surface standard deviation of 0.14 mm. We expect similar or better performance in this data set. Positioning repeatability of the robot is very high, with a standard deviation of 0.0031 mm over two months.

Additional instruments used for generating the data include a CT (Computed Tomography) scanner for ground truth geometry of transparent objects (described in Section 3) and an illumination arch for controlled directional light-

Figure 2. Preliminary images from our data set. In the first row, three glass objects (sphere, bowl, teapot) with markers placed on. On the second row, three calibration and rendering tools part of the pipeline: a black and white checkerboard (coordinate estimation), an X-Rite ColorChecker® (color balance compensation) and a chrome sphere (environment light evaluation).

ing (described in Section 4).

3. Transparent Objects

Our goal is to extend our original MVS dataset to account for transparent objects where the focus is on reconstruction of geometry and appearance. Usually, the radiometric behavior of the objects used in 3D reconstructions is assumed diffuse and opaque. This leads to a number of simplifications that we cannot apply to transparent objects. In the case of transparent objects, refraction and reflection cause distortion effects that complicate reconstruction.

Previous methods acquire data sets useful for image-based rendering of a transparent object [18, 11]. However, these methods do not produce an actual triangle mesh and require special rendering techniques for reconstruction of the appearance of the transparent object. A survey on methods that do provide a triangle mesh is available [13]. In this survey, they note that CT scanning of refractive objects like glass is costly but straight forward. Thus, we use CT scanning to obtain ground truth geometry. Another way is to acquire shape and pose of a transparent object from motion [3]. In any case, there seems to be no data set, like the one we propose, which is useful for multiple view reconstruction of transparent objects.

3.1. Data

Our data set contains a set of multiple view HDR images of three glass objects with different radiometric properties (top row of Figure 2). We use a solid sphere, a bowl with lid (composed of two parts) and a teapot with multiple thin glass layers (composed of three parts). The walls of the bowl and the teapot have different thickness. A diffuse backdrop is provided for the objects. We have made this as a gradient checkerboard, so that one half of the squares varies in color from left to right, and the other half varies in color from top to bottom. In this way, we can see how light reflects, refracts and scatters through the objects. The refractive index of the glass objects will be estimated directly from the scanned images, or, if this is unsuccessful, by the use of a refractometer. We marked the objects with small black plastic spheres, in order to easily determine their position relative to the scene. In our data set, we also provide high-resolution triangle meshes generated from CT scans. We use these scans as ground truth for either geometrical reconstruction algorithms or physically based rendering algorithms for appearance modelling.

Our current data set creation procedure is as follows. First, we choose a sequence of camera positions and orientations for our industrial robot. The robot enables us to reproduce a given set of positions and orientations with a very high precision. Then, we capture a first set of images placing a black and white checkerboard in the scene. This is done to obtain the camera positions relative to the scanned objects and calculate camera parameters for the setup. Secondly, we scan a commercial color checker, which allows us to compensate for color channel alterations in the final images. Finally, we scan a chrome sphere to get an HDR environment map of the surroundings. We use the resulting map as a light source in our rendering algorithms [5], so we can simulate the resulting scene with high precision. After these three calibration steps, we can finally scan the glass objects using the same pre-defined path used for the calibration images.

Once compiled, we are planning to use this data set to verify that the radiometric models [9] properly describe the radiometric properties of the scene. To do this we plan to feed the ground truth of our data into a custom-built renderer based on the NVIDIA OptiX library [20], and see how well it reproduces the images. If successful, we have a validated computational model, which in principle we 'just' have to invert to do 3D reconstruction of transparent objects. Following this we plan at applying state of the art 3D reconstruction algorithms and quantify how far the state of the art has come toward solving this central 3D vision reconstruction problem.

4. BRDF measurements and Photometric Stereo

The radiometric behaviour of an object plays a crucial role in MVS. Often this behaviour has been ignored or at most assumed Lambertian. This allows for acceptable reconstructions of geometry, but often poor recovery of the reflectance. For more accurate MVS and reflectance capture, the BRDF of an object should be taken into account and this is a problem that receives a growing amount of

attention [24, 15]. Within the field of photometric stereo, the reflectance of an object is the key element in recovering surface normals and thereby indirectly the object's geometry. Also here, assumptions about reflectance are made, these include e.g. Lambertian behaviour [27] or isotropic BRDFs [12].

For both of the above areas, a multi-view data set having ground-truth reflectance behaviour would be of great value, and does, to our knowledge, not currently exist. We are therefore now working on a MVS data set where not only the ground-truth geometry is given, but also a densely sampled BRDF ground-truth for all materials in the scene. In the following, we will elaborate on the details of how this data set will be acquired and what it will include.

4.1. Concept

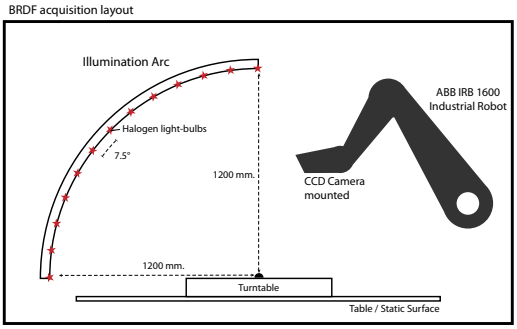

Figure 3. Schematic of BRDF capturing setup. Setup includes a 6-axis industrial robot holding a CCD (stereo) camera for view, and an arc in conjunction with a turntable for illumination.

Capturing the reflectance of a material generally requires four degrees of freedom: polar and azimuthal angle of illumination-direction, and polar and azimuthal angle of view-direction, $\rho(\omega_i, \phi_i, \omega_v, \phi_v)$. Utilizing our lab-facility's 6-axis industrial robot, mounted with a stereo-camera setup, all view directions (ω_v, ϕ_v) can effectively be captured. For illumination directions (ω_i, ϕ_i), we utilize an illumination arc and a rotation-table. The arc holds a range of halogen light-bulbs and is capable of covering the polar angle ϕ_i in 7.5° intervals. The rotation-table turns the target sample with a resolution of $< 1^\circ$, thus densely covering θ_i. Figure 3 shows a schematic of the BRDF capturing setup, and Figure 4 is a photo of an actual acquisition scene.

Using the above described setup, we intend to densely sample the BRDFs of a collection objects whose surfaces consist of one or a few, isotropic, BRDFs. The BRDFs of each material will be stored in the 3-dimensional Rusinkiewicz frame for isotropic BRDFs [21], as also done in the MERL database[17], although with a coarser resolution of 7.5° in each dimension. In conjunction with the densely sampled BRDFs, stereo images of scenes containing the sampled objects will be acquired for a wide range of directions. Objects will be of relatively low geometric complexity, and scenes will consist of one or more of the objects.

Figure 4. Capturing the BRDF of an object with known geometry. All illumination directions and view-directions are covered for each type material present on the object.

5. Non-Rigid Structure from Motion

Evaluating Non-rigid feature matching and NRSfM algorithms[1] in a quantitative manner has in the literature proven to be problematic. Deformations are inherently a dynamic process and subject to the physical properties of the objects in consideration. Thus, evaluating deformation modelling algorithms require a reasonable number of different objects and set of motions. Also, given the dynamic deformation objects might change their topology (e.g. stretching and tearing) and easily self-occluded some parts of the shape. For this reason, many approaches have provided several models that fit specific types of deformation, but that cannot comprise all of them. For this reason understanding the real performance of methods on realistic deformations is necessary to push forward advancements in this field.

The central problem of producing reference ground truth has been approached from many different angles. Several works compare their methods using synthetically generated images, as the true 3D geometry is readily available[26, 22, 19, 10]. Another popular approach is using MOCAP data, mainly human motion, for generating both test video sequence with 3D reference points [7, 26, 2, 10, 25]. Both falls short, as the former often lacks the complexity found in real-life scenes and the latter provides only a sparse set of reference points that are likely not to be possible to detect from images because of occlusions. As stated in [22, 8], there is a lack of and a need for a real-life NRSfM sequence with a dense 3D reference.

[1] A review on NRSfM methods, updated to 2010, can be found here: [23]

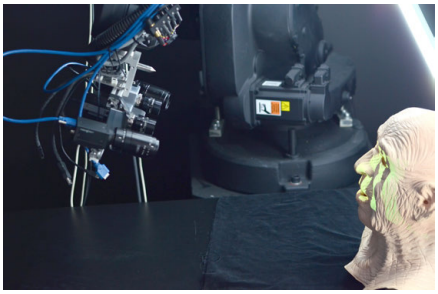

Figure 5. Robot arm carrying cameras for capturing stop motion frame and structured light data. A Gray code pattern is currently being projected onto the object.

We seek to remedy this situation by providing a video recording of real objects with dense 3D ground truth for each frame. It will be accomplished using a stop motion like animation techniques and structured light 3D scanning, combined in our unique recording setup.

5.1. Concept

We wish to simulate motion in a manner similar to stop motion animated films. Here a rigid object is moved into a certain pose, an image is taken, the object is slightly changed with a deformation, another image is taken etc. The result is a sequence that, when played at an interactive frame rate, provides the illusion of motion. We will apply the same principle here, in generating a benchmarking data set for NRSfM with ground truth.

Now one may ask, why not just record the motion using ordinary video format? After all, stop motion techniques does not properly reproduce motion blur artifacts that are present in standard recorded video sequences. Our approach has several significant advantages that greatly outweigh the loss of motion blur. Most importantly, we can obtain a 3D ground truth for each frame. After adjusting the object into its current frame position and acquiring an image for the stop motion sequence, we will perform a 3D scan using structured light. Utilizing gray code patterns we obtain a dense ground truth so obtaining both the image frame and a 3D reference for benchmarking and validation.

Another advantage is that we can obtain data from multiple views by acquiring images at different angles thus providing data for evaluating multi-view NRSfM (e.g. [6]). Furthermore, this procedure provides a great degree of control over both camera movement and object pose. As each frame is recorded independently, time in between becomes a non-issue.

Figure 6. Actuators for manipulating the geometry of the mask. The image of the mask has been superimposed on an image of the actuators, illustrating their functionality.

5.2. Implementation

Such data could be acquired by pure manual effort, however that would be extremely time consuming and error-prone. As such, a robotics solution is currently being developed with a the data acquisition procedure that is predictably and reproducibly implemented. In detail, a robotic arm move the camera and the projector needed for data acquisition and structured light scan. From this the view position can be determined with high precision and reproducibility. Figure 5 illustrates this setup.

Additionally, object deformation will also be automated and Figure 6 shows an example with an object where a mask resembling a human face is put on top of two actuators. Manipulating the actuators deforms the mask geometry, simulating facial movement. Similar results can be obtained with cloth, paper and other deformable materials.

6. Concluding Remarks

We have here presented our ongoing work on making high quality data sets for evaluating and developing methods for 3D vision. A motivation for doing this is that we see a need for this, especially with respect to making data sets that are large enough, so that it is possible to reasonably determine if differences in performance are a statistical fluke, or are in fact statistically significant.

By presenting our ongoing work in this forum, we hope to get valuable and constructive feedback on how these data sets in the making could be adapted to serve the needs of the computer vision communities as best possible.

References

[1] H. Aanæs, A. Dahl, and K. Steenstrup Pedersen. Interesting interest points. *International Journal of Computer Vision*, 97(1):18–35, 2012.

[2] I. Akhter, Y. Sheikh, S. Khan, and T. Kanade. Trajectory space: A dual representation for nonrigid structure from motion. *Pattern Analysis and Machine Intelligence, IEEE Transactions on*, 33(7):1442–1456, 2011.

[3] M. Ben-Ezra and S. Nayar. What does motion reveal about transparency? In *Proceedings of IEEE International Conference on Computer Vision (ICCV)*, pages 1025–1032, 2003.

[4] A. Dahl, H. Aanæs, and K. Pedersen. Finding the best feature detector-descriptor combination. In *International Conference on 3D Imaging, Modeling, Processing, Visualization and Transmission*, pages 318–325, 2011.

[5] P. Debevec. Rendering synthetic objects into real scenes: Bridging traditional and image-based graphics with global illumination and high dynamic range photography. In *Proceedings of ACM SIGGRAPH 98*, pages 189–198, 1998.

[6] A. Del Bue and L. Agapito. Stereo non-rigid factorization. *International Journal of Computer Vision*, 66(2):193–207, February 2006.

[7] J. Fayad, L. Agapito, and A. Del Bue. Piecewise quadratic reconstruction of non-rigid surfaces from monocular sequences. In K. Daniilidis, P. Maragos, and N. Paragios, editors, *Computer Vision – ECCV 2010*, volume 6314 of *Lecture Notes in Computer Science*, pages 297–310. Springer, 2010.

[8] K. Fragkiadaki, M. Salas, P. Arbelaez, and J. Malik. Grouping-based low-rank trajectory completion and 3D reconstruction. In Z. Ghahramani, M. Welling, C. Cortes, N. Lawrence, and K. Weinberger, editors, *Advances in Neural Information Processing Systems 27*, pages 55–63. Curran Associates, Inc., 2014.

[9] A. S. Glassner. Surface physics for ray tracing. In A. S. Glassner, editor, *An Introduction to Ray Tracing*, chapter 4, pages 121–160. Academic Press Ltd., London, UK, 1989.

[10] P. F. U. Gotardo and A. M. Martinez. Kernel non-rigid structure from motion. In *Proceedings of IEEE International Conference on Computer Vision (ICCV)*, pages 802–809. IEEE, 2011.

[11] T. Hawkins, P. Einarsson, and P. E. Debevec. A dual light stage. *Rendering Techniques 2005 (Proceedings of EGSR 2005)*, pages 91–98, 2005.

[12] M. Holroyd, J. Lawrence, G. Humphreys, and T. Zickler. A photometric approach for estimating normals and tangents. *ACM Transactions on Graphics (Proceedings of SIGGRAPH Asia 2008)*, 27(5):133, 2008.

[13] I. Ihrke, K. N. Kutulakos, H. Lensch, M. Magnor, and W. Heidrich. Transparent and specular object reconstruction. *Computer Graphics Forum*, 29(8):2400–2426, 2010.

[14] R. Jensen, A. Dahl, G. Vogiatzis, E. Tola, and H. Aanæs. Large scale multi-view stereopsis evaluation. In *Proceedings of the IEEE Conference on Computer Vision and Pattern Recognition (CVPR)*, pages 406–413, 2014.

[15] H. Jin, S. Soatto, and A. J. Yezzi. Multi-view stereo beyond Lambert. In *Proceedings of Computer Vision and Pattern Recognition (CVPR)*, volume 1, pages I:171–178. IEEE, 2003.

[16] S. Kim, H. Aanæs, A. Dahl, K. Conradsen, R. Jensen, and S. Kim. Multiple view stereo by reflectance modeling. In *International Conference on 3D Imaging, Modeling, Processing, Visualization and Transmission*, 2012.

[17] W. Matusik, H. Pfister, M. Brand, and L. McMillan. A data-driven reflectance model. *ACM Transactions on Graphics (Proceedings of SIGGRAPH 2003)*, 22(3):759–769, 2003.

[18] W. Matusik, H. Pfister, R. Ziegler, A. Ngan, and L. McMillan. Acquisition and rendering of transparent and refractive objects. pages 267–278, 2002.

[19] S. I. Olsen and A. Bartoli. Implicit non-rigid structure-from-motion with priors. *Journal of Mathematical Imaging and Vision*, 31(2-3):233–244, 2008.

[20] S. G. Parker, J. Bigler, A. Dietrich, H. Friedrich, J. Hoberock, D. Luebke, D. McAllister, M. McGuire, K. Morley, A. Robison, and M. Stich. OptiX: a general purpose ray tracing engine. *ACM Transactions on Graphics (Proceedings of SIGGRAPH 2010)*, 29(4):66:1–66:13, July 2010.

[21] S. Rusinkiewicz. A new change of variables for efficient BRDF representation. In *Rendering Techniques (Proceedings of EGWR 1998)*, June 1998.

[22] C. Russell, J. Fayad, and L. Agapito. Dense non-rigid structure from motion. In *Proceedings of 3DIMPVT 2012*, pages 509–516. IEEE, 2012.

[23] M. Salzmann and P. Fua. Deformable surface 3d reconstruction from monocular images. *Synthesis Lectures on Computer Vision*, 2(1):1–113, 2010.

[24] S. M. Seitz, B. Curless, J. Diebel, D. Scharstein, and R. Szeliski. A comparison and evaluation of multi-view stereo reconstruction algorithms. In *Proceedings of Computer Vision and Pattern Recognition (CVPR)*, volume 1, pages 519–528. IEEE, 2006.

[25] L. Tao and B. J. Matuszewski. Non-rigid structure from motion with diffusion maps prior. In *Proceedings of Computer Vision and Pattern Recognition (CVPR)*, pages 1530–1537. IEEE, 2013.

[26] J. Taylor, A. D. Jepson, and K. N. Kutulakos. Non-rigid structure from locally-rigid motion. *Proceedings of Computer Vision and Pattern Recognition (CVPR)*, pages 2761–2768, 2010.

[27] R. J. Woodham. Photometric method for determining surface orientation from multiple images. *Optical Engineering*, 19(1):191139, 1980.

Appendix D

Contribution C.IV: On Optimal, Minimal BRDF Sampling for Reflectance Acquisition

On Optimal, Minimal BRDF Sampling for Reflectance Acquisition

Jannik Boll Nielsen* Henrik Wann Jensen† Ravi Ramamoorthi‡
*Technical University of Denmark †‡University of California, San Diego

Abstract

The bidirectional reflectance distribution function (BRDF) is critical for rendering, and accurate material representation requires data-driven reflectance models. However, isotropic BRDFs are 3D functions, and measuring the reflectance of a flat sample can require a million incident and outgoing direction pairs, making the use of measured BRDFs impractical. In this paper, we address the problem of reconstructing a measured BRDF from a limited number of samples. We present a novel mapping of the BRDF space, allowing for extraction of descriptive principal components from measured databases, such as the MERL BRDF database. We optimize for the best sampling directions, and explicitly provide the optimal set of incident and outgoing directions in the Rusinkiewicz parameterization for $n = \{1, 2, 5, 10, 20\}$ samples. Based on the principal components, we describe a method for accurately reconstructing BRDF data from these limited sets of samples. We validate our results on the MERL BRDF database, including favorable comparisons to previous sets of industry-standard sampling directions, as well as with BRDF measurements of new flat material samples acquired with a gantry system. As an extension, we also demonstrate how this method can be used to find optimal sampling directions when imaging a sphere of a homogeneous material; in this case, only two images are often adequate for high accuracy.

CR Categories: I.4.1 [Image Processing and Computer Vision]: Digitization and Image Capture—Reflectance I.3.7 [Computer Graphics]: Three-Dimensional Graphics and Realism—Color, shading, shadowing, and texture;

Keywords: reflectance, BRDF, MERL, reconstruction

1 Introduction

The bi-directional reflectance distribution function or BRDF [Nicodemus et al. 1977] characterizes material appearance, representing the unique reflectance of paints, metals, plastics, or velvet. The BRDF is a 4D quantity, depending on incident and outgoing directions, and can be reduced to 3D under the common assumption of isotropic reflectance. Historically, parametric BRDF models such as Phong [1975], Cook-Torrance [1982] or Lafortune [1997] have been used. In the past two decades, as the need for more realistic appearance and reproduction of real-world materials has increased, measured or data-driven BRDF models have become more popular, and databases such as the MERL BRDF database [Matusik et al. 2003a] have been developed. In principle, it is easy to measure the BRDF using a gonioreflectometer (we achieve this in practice using a gantry system with a flat material sample). However, for a dense sampling of even 100 samples in each direction (critical for capturing sharp highlights), one would need a million samples or images over the full 3D isotropic BRDF. This is prohibitive in most applications, and considerably reduces the practicality of measured BRDFs.

Figure 1: *Rendering of isotropic BRDFs of unknown materials, reconstructed with our method from only 20 measurements captured at optimal sample locations (see Fig 10 for error plots).*

In this paper, we address the fundamental problem of where to sample an unknown BRDF when only a very limited number of samples can be acquired. Our goal is to make measured reflectance practical in computer graphics for product design, virtual reality, appearance fabrication and entertainment, as well as in industrial quality control, where appearance must often be monitored in real-time. The question is how best to orient n light-sources and n cameras, such that the best impression of the appearance (BRDF) is obtained. We base our analysis on the MERL isotropic BRDF database [Matusik et al. 2003a], assuming that this covers the majority of real world isotropic material variation. We demonstrate that we can reconstruct a data-driven BRDF from a very small set of (fewer than 20) measurements. Our specific contributions are as follows:

New BRDF Mapping: We introduce a new mapping of the BRDF (Sec. 3) that enables a linear approach, with principal components from the MERL BRDF database that are highly descriptive of reflectance phenomena like diffuse and specular reflection, Fresnel effects and retroreflection (Fig. 3).

Optimization for Sampling Directions: We identify regions of importance based on the condition number of subsets of rows from the principal component matrix of the data [Ipsen and Wentworth 2014] (Sec. 4). The condition number directly relates to the quality at which one can expect to reconstruct a BRDF, with a given set of samples known from it. Based on this, we obtain a pri-

*jbol@dtu.dk
†henrik@cs.ucsd.edu
‡ravir@cs.ucsd.edu

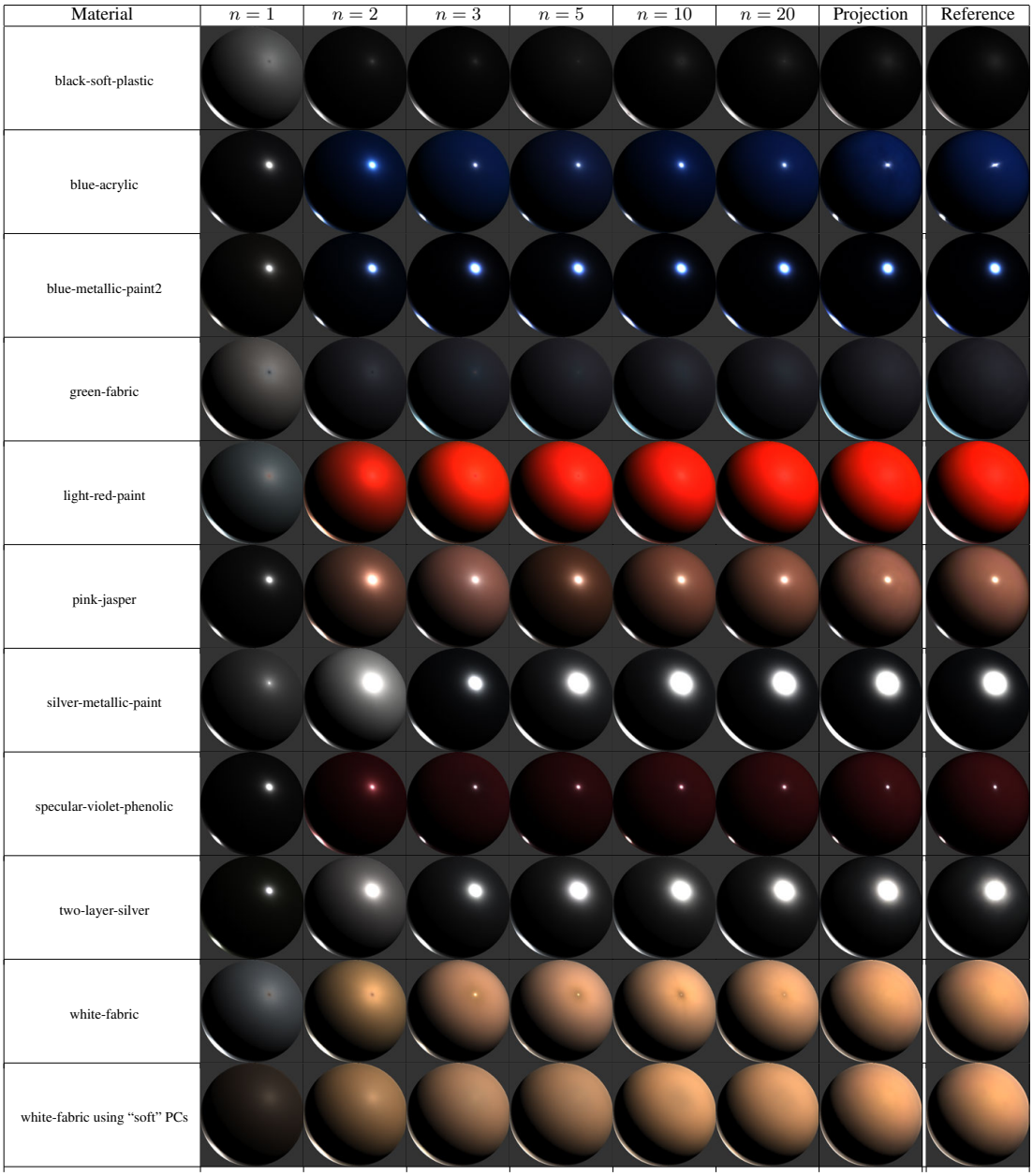

Figure 2: *Reconstructions of unknown samples (10 MERL BRDF samples not used at all for computing principal components (PCs) and sample directions). The BRDFs are rendered as spheres, illuminated by a front-light at a direction of* $[1, 1, 1]$*, and a back-light causing grazing angle reflections at* $[-1, -1, -3]$*. Reconstructions are made with* $n = \{1, 2, 3, 5, 10, 20\}$ *sampling points. In addition, reconstructions using all possible sampling points are shown. This corresponds to a projection of the data into PC-space and shows the best possible reconstruction. Finally, the far right column shows reference renderings of the true BRDFs. We see that generally 3-10 measurements are sufficient to capture the true appearance of a material. For some diffuse materials, more samples are needed to avoid ringing at the highlights. Alternatively, as mentioned in Sec. 8, a separate "soft" set of principal components can be used to avoid this ringing.*

oritized list of light/view direction pairs, which indicates the best directions to sample from in a point-sampling setup, when only n samples are to be acquired. The list does not, by far, cover all variability observable in BRDFs, but it does tell us where the strategically best places to sample are, ensuring that the maximum possible amount of unique information is captured with every sample. We differ from [Matusik et al. 2003b] in considering a very small number of measurements (10-20 instead of 800-1000), and we develop a novel optimization algorithm suited for our purpose. We provide the optimal set of incident and ougoing directions in the Rusinkiewicz [1998] half-difference parameterization for $n = \{1, 2, 5, 10, 20\}$ samples (Table 1 in Sec. 6), which can directly be used by practitioners.

BRDF Reconstruction and Validation: Inspired by the statistical reconstruction methods of [Blanz et al. 2004], we propose a similar ridge-regression based method to reconstruct full BRDFs from this sparse set of samples (Sec. 5). This method penalizes solutions that statistically deviate from the variability learned by the MERL database. We validate our directions and reconstruction method in two ways. First, we (randomly) leave out 10 materials in the MERL BRDF database, obtaining a slightly different set of principal components and sampling directions from the remaining 90. We then use these 10 materials as a validation set. Figure 2 shows the accuracy with increasing numbers of samples, demonstrating that 5-10 samples is often adequate, and 20 BRDF samples provides accurate results in all cases. Next, we consider flat samples of new real-world materials. We use $n = 20$ samples from five unknown materials, and compare the reconstructions with the densely measured in-plane reflectances of the materials (Sec. 7).

Extension to Image-Based BRDF Measurement: Our main contribution is for BRDFs acquired from a sparse set of measurements with a gonioreflectometer (in our case, a gantry setup with a flat material sample). We also demonstrate an extension to the popular image-based BRDF measurement method (Sec. 9), that takes 2D images of spheres of homogeneous materials rather than single measurements [Marschner et al. 2000] (and the approach used to acquire the database [Matusik et al. 2003a]). We demonstrate that two images are often adequate in this case (Table 2 and Fig. 12).

2 Related Work

The canonical approach to BRDF acquisition, considered here, is to sample individual light/view directions for a flat sample using a gonioreflectometer as done in e.g. [White et al. 1998]. As noted above, this is slow, and a variety of alternative setups and sampling strategies leveraging parallel acquisition of multiple BRDF samples with a CCD camera in conjunction with known curved geometry, mirror setups, and adaptive sampling schemes have been proposed.

Image-Based BRDF Measurement: Marschner et al. [2000] proposed a method where a sphere of homogeneous material is imaged (2D set of samples) from a 1D set of lighting drections, to obtain an isotropic 3D BRDF. Other, more complex setups, with curved mirrors etc. have also been proposed [Ward 1992; Dana and Wang 2004; Ghosh et al. 2007; Noll et al. 2013; Schwartz et al. 2014]. Indeed, the approach of Marschner et al. [2000] was used to acquire the MERL database [Matusik et al. 2003a]. However, this method is limited to spheres (or samples that can be painted/wrapped on a sphere). In this paper, we mainly address the canonical case of gonioreflectometric measurement for a flat sample, showing how a very sparse set of measurements suffices. We also demonstrate an extension to image-based BRDF measurement where two images is adequate, rather than full 1D lighting variation.

Adaptive Sampling: Fuchs et al. [2007] suggest an adaptive sampling scheme where the observed properties of the BRDF being measured are taken into account. Here, regions needing to be refined are detected by evaluating how well a sample is modeled by its neighboring samples. A major limitation of this method is that a somewhat dense grid of samples must be acquired before the refinement procedure converges well. In contrast, our method is non-adaptive, and we use a very sparse fixed set of (precomputed and tabulated) sampling directions for any material. Lensch et. al. [2003] suggest a different approach, where the next sampling direction is estimated based on an uncertainty measure of the fitted BRDF parameters. This approach allows for full control of the number of samples used, but in contrast to our method, it relies on fitting a parametric model, with the resulting limitations.

Complex Environment Lighting: Some recent work has explored acquisition of simpler 2D BRDF models under environment lighting [Romeiro et al. 2008] or even using a controlled environment [Ghosh et al. 2007; Tunwattanapong et al. 2013; Aittala et al. 2013]. These methods have shown convincing results, where different variants of convolutional theory are used to obtain homogeneous or spatially varying BRDFs. However, they require solving non-linear systems and regularization, while we focus on more direct measurement of BRDFs from individual samples. Alternative approaches where the environment is unknown but geometry is known have also been suggested [Romeiro and Zickler 2010]; however, the ambiguity between environment and BRDF can be difficult to resolve, requiring various heuristics for regularization.

Rapid Reflectometry: Ren et al. [2011] propose pocket reflectometry, where a reference checkerboard with known reflectance tiles is used in conjunction with a handheld lightsource and a fixed camera. Older work simply compares reference BRDFs to the target-BRDF [Hertzmann and Seitz 2003]. These are somewhat related to our proposed method in that they reconstruct appearance based on reference BRDFs, with the difference that they are limited by the relatively small number of reference BRDFs used and by the need of physically placing the references in the scene.

Efficient Sampling: Closest to our work is that of Matusik et al. [2003b], who mention that for $n = 800$ samples, an unknown BRDF can be modeled by a linear combination of other BRDF models from their dataset. Note that this is for measuring individual BRDF samples, as in our paper, rather than for image-based measurement. Their method is closely related to the optimum sampling directions in our work. However, they do not explicitly provide which directions these 800 samples correspond to, nor investigate how this quality converges. Weyrich et al. [2006] utilizes this method to reconstruct spatially varying BRDFs of human skin, and [Hullin et al. 2010] uses it to interpolate fluorescence measurements for BRRDFs.

We extend the work of Matusik et al. [2003a; 2003b] by introducing a novel BRDF mapping that makes linear modeling possible from fewer samples. Our mapping addresses the issues of non-physical and odd-looking reconstructions, including those having negative reflectance values. Critically, we focus on optimal *minimal* sampling with $n < 20$, rather than $n = 800$, showing that this much smaller set suffices. We develop an optimization method that quickly yields optimal sampling locations for small values of n, compared to the greedy approach [Matusik et al. 2003b]. We provide tables of the $n = 20$ optimal directions, that can be used directly. We also suggest a reconstruction approach that takes into account the statistical variability of BRDFs based on PCA, rather than linear combinations of raw measured BRDFs. Finally we discuss the extension to capturing images of spheres, rather than classical gonioreflectometric point-sampling.

Materials Standards: In the materials industry, various standards have been proposed, and are widely used, to characterize reflectance. For specular or glossy materials, the simplest is the method of Hunter and Judd [1939], who simply measured the reflectance at 60° perfect reflection. An extension to this is adding the near-normal and grazing-angle behavior by measuring the reflectance at 85° and 20° perfect reflection as well [Hunter 1987]. This is also known as the ASTM standard D523. Within the more complex types of materials, such as car-paint and pearlescent colors, additional information is required. Westlund and Meyer [2001] describe that the sets of aspecular angles $\{15^\circ, 45^\circ, 110^\circ\}$ and $\{25^\circ, 45^\circ, 75^\circ\}$, both with 45° incident light, have been suggested for characterizing these more complex materials. Westlund et al. themselves utilize all five angles ($\{15^\circ, 25^\circ, 45^\circ, 75^\circ, 110^\circ\}$) to obtain maximum information about the materials. We adapt these five directions in our comparison in Sec. 6, showing that our method provides significantly more accurate results with our five optimized directions.

Parametric Fits: Finally, considerable effort has been devoted to fit parametric BRDF models to real-world observations. These include both empirical ([Phong 1975; Blinn 1977; Ward 1992; Lafortune et al. 1997]) and physically-based ([Torrance and Sparrow 1967; Cook and Torrance 1982]) reflectance models, and recently also more advanced parametric BRDFs have been proposed, aiming at reproducing the behaviors observed in MERL ([Löw et al. 2012; Brady et al. 2014]). As all models are simplifications of the true behavior, one has to determine what regions of a BRDF the models should prioritize, i.e., what objective function the optimizers should minimize. Using the L_1-norm to emphasize the base of a specular peak, rather than the extremum has been suggested, and various transformations of the observed data have also been proposed such as square or cubic root, logarithmic, and cosine weighting [Ngan et al. 2005]. We leverage some of these observations, including logarithmic mapping and cosine-weighting in our BRDF remapping, but also normalize by the average or a reference BRDF. Crucially, we focus on data-driven reflectance, rather than parametric BRDF models. It is also important to note that although parametric models are thought of as compact, even the most simple models, such as the Phong model, have at least 7 tunable parameters (three if ignoring color). This calls for at least the same number of samples, but ideally many more to get a robust fit. Given our sparse data, even the number of parameters in the most simple analytical models is often comparable to, or exceeds, the number of samples we use. In addition, our proposed method is based on solving a linear system, thus eliminating the need for non-linear optimization and the challenge of local minima.

3 Data and Mapping

We base our analysis on the MERL isotropic BRDF database [Matusik et al. 2003a]. This database covers 100 materials of varying reflectance, from soft diffuse materials like rubber, to hard specular materials like chrome. The reflectance is represented by dense BRDF measurements in a 3D volume using Rusinkiewicz half-difference angle coordinates $(\theta_h, \theta_d, \phi_d)$ [Rusinkiewicz 1998]. The resolution for each RGB color is $(90 \times 90 \times 180)$, or $1,458,000$ measurements. We seek to dramatically reduce the number of measurement samples needed to 20 or fewer. Principal Component Analysis (PCA) has been performed on this dataset before [Matusik et al. 2003a; Ngan et al. 2006], with the obervation that a linear transformation on the raw BRDFs, such as PCA, is inferior to non-linear transformations. Furthermore, Matusik et al. [2003a] observed that linear combinations of raw BRDFs could give rise to unrealistic results such as negative reflectance values and "holes".

Log-Relative Mapping: The poor performance of PCA on raw BRDF values is closely related to the high dynamic range within the BRDF (which is several orders of magnitude), combined with the variation clearly not following a normal distribution. This fact motivates the use of a mapping of data that preserves inter-BRDF variation while dampening intra-BRDF variation. This mapping should at the same time also make the data more normally distributed. We propose a novel log-relative mapping for this purpose:

$$\rho \mapsto \ln\left(\frac{\rho \ \cos_{\text{weight}} + \epsilon}{\rho_{\text{ref}} \ \cos_{\text{weight}} + \epsilon}\right), \tag{1}$$

where ρ is the BRDF, ϵ is a small constant that avoids division by zero and sensitivity to camera noise (we use $\epsilon = 0.001$), and ρ_{ref} is a *reference* BRDF, relative to which the mapping is applied. In our experiments, we choose the reference BRDF to be the median value for each $(\theta_h, \theta_d, \phi_d)$, over the entire dataset of BRDFs. We choose the median rather than the mean, to make the mapping more robust towards outliers in the dataset. A cosine-weight is applied to compensate for extreme grazing-angle values, as in previous work,

$$\cos_{\text{weight}} = \max\left\{\cos(\mathbf{n}\cdot\boldsymbol{\omega}_i)\cos(\mathbf{n}\cdot\boldsymbol{\omega}_o)\ ,\ \epsilon\right\}, \tag{2}$$

where $\mathbf{n}, \boldsymbol{\omega}_i, \boldsymbol{\omega}_o$ are the normal, illumination-direction, and view-direction vectors respectively, obtained from converting a BRDF location $(\theta_h, \theta_d, \phi_d)$ to the Cartesian coordinate frame. The reference BRDF, ρ_{ref}, is shown in Fig. 3.

Note that every $(\theta_h, \theta_d, \phi_d)$ BRDF value is essentially compared individually to a reference BRDF, and the natural logarithm is then used to weight smaller and greater values equally (i.e., a value *half* the size of the reference value should have the same magnitude as a value twice as big as the reference).

RGB Colors as Independent BRDF Samples: It is apparent that many (most) BRDF behaviors are covered by the database, with materials ranging from smooth and soft, to hard and specular, with varying Fresnel effect (refractive indices), and even retro-reflection. It is however also apparent that not all color-variation has been covered, e.g., there is a pink specular material, but not a pink soft material. Therefore, we choose to work in grey-scale and treat each of the 3 color channels of the BRDFs as individual observations. This allows us to abstract away the color, and effectively have three times as many observations (material samples), at the cost of the samples being a little correlated. Our algorithm then simply reconstructs each color channel of the BRDF separately; this does not require any additional measurements.

With 100 materials, each having 3 color-channels that are being treated as individual grey materials, a total of $m = 300$ BRDFs are available in the database. Each material can be vectorized as a point in a $p = 90 \cdot 90 \cdot 180 = 1,458,000$-dimensional space. This gives an observation matrix $\mathbf{Y} \in \mathbb{R}^{m \times p}$. As mentioned above, we use the median of the dataset as the reference BRDF, $\boldsymbol{\rho}_{\text{ref}} \in \mathbb{R}^p$:

$$\rho_{\text{ref},i} = \text{median}\left(Y_{[1,i]}, Y_{[2,i]}, \ldots, Y_{[m,i]}\right) \tag{3}$$

Using the reference BRDF, all observations (rows) in $\boldsymbol{Y}$ can be mapped using the mapping in Equation 1, resulting in the mapped observation matrix $\boldsymbol{X}$:

$$X_{j,i} = \text{mapping}(Y_{[j,i]}, \rho_{\text{ref},i}). \tag{4}$$

Principal Components: Up to $k = m = 300$ principal components may be extracted from $\mathbf{X}$ by performing singular value decomposition (SVD) of the mean-subtracted mapped observation matrix:

$$(\boldsymbol{X} - \hat{\boldsymbol{\mu}}) = \boldsymbol{U}\boldsymbol{\Sigma}\boldsymbol{V}^T, \tag{5}$$

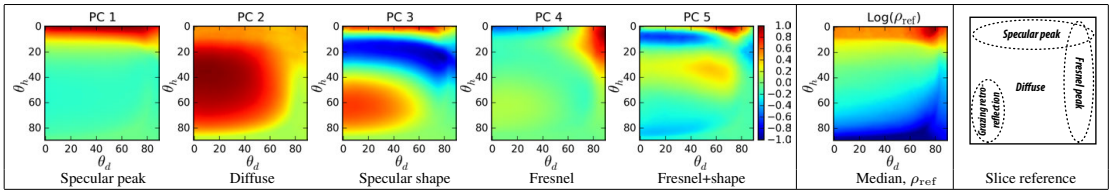

Figure 3: *BRDF-slices of the first 5 principal components of the MERL database, using the mapping from Equation 1. Slices are made at $\phi_d = 90°$, and an interpretation of them is shown on the far right, adapted from [Burley 2012] . Notice how the primary variation (the first principal component) is in the specular peak, and the second principal component primarily contributes to the diffuse region of the BRDF. The third component contracts or widens the specular peak. The fourth component adds Fresnel-effect and finally the fifth both contributes to Fresnel, shaping the specular peak, and a bit of retro-reflection.*

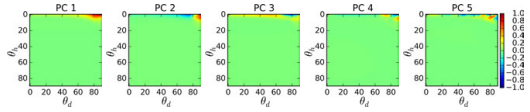

Figure 4: *BRDF-slices of the first 5 principal components of the MERL database without using any mapping. Slices are made at $\phi_d = 90°$. Due to the large dynamic variation in the raw BRDFs, the specular direction is dominating all variation.*

where $\boldsymbol{\mu} \in \mathbb{R}^{1\times p}$ is the mean over m rows of $\mathbf{X}$, and $\hat{\boldsymbol{\mu}} \in \mathbb{R}^{m\times p}$ simply repeats $\boldsymbol{\mu}$ for each row. The columns of $\boldsymbol{V} \in \mathbb{R}^{p\times k}$ are eigenvectors of the covariance $(\boldsymbol{X} - \hat{\boldsymbol{\mu}})^T(\boldsymbol{X} - \hat{\boldsymbol{\mu}})$, and correspond to the principal components of the data. The diagonal elements, σ_i^2, of $\boldsymbol{\Sigma} \in \mathbb{R}^{k\times k}$ correspond to the variance explained by the i^{th} principal component.

In Fig. 3, the first 5 principal components are visualized as BRDF-slices [Burley 2012]. An interpretation reference is shown to the far right in the figure. The slices reveal very interesting structures of the principal components: the first principal component largely models the intensity of the specular peak, by affecting only the region where θ_h is close to zero. The second principal component models diffuse contribution allowing for either raising or lowering the overall reflectance for all non-grazing angles. The blue band in the third component allows for widening or contraction of the specular peak. Finally, the fourth and fifth components model various combined effects; most notably the Fresnel effect contribution at θ_d close to $90°$ and the additional shaping of the specular peak in PC5, but also a small contribution to the retro-reflective behaviour in the lower left corner. These informative principal components are a result of the log-mapping introduced in Equation 1. Without it, the majority of all numerical variation is concentrated in the specular peak, drowning all off-peak variation of the BRDFs. This is shown in Fig. 4, where slices of the first 5 unmapped principal components are illustrated. Although these components numerically describe the data well, we see qualitatively that they hold little information about the overall nature of a BRDF.

Finally, as it will later become convenient, a matrix of scaled principal components, $\boldsymbol{Q} \in \mathbb{R}^{p\times k}$, can be obtained by:

$$\boldsymbol{Q} = \boldsymbol{V}\boldsymbol{\Sigma}. \tag{6}$$

Here, the length of each principal component has been scaled by the amount of variance it covers.

4 Optimization of Sampling Directions

Before introducing the optimization scheme used to determine optimal sampling directions, we give the general idea behind reconstruction of BRDFs, as this is the primary driver behind the objective function used to choose the sampling directions.

Using the scaled principal components $\boldsymbol{Q} \in \mathbb{R}^{p\times k}$ obtained from Equation 6, a new BRDF $\boldsymbol{x}$ may be synthesized using a linear combination $\boldsymbol{c}$ of the principal components ($\boldsymbol{c} \in \mathbb{R}^{k\times 1}$ is a vector):

$$\boldsymbol{x} = \boldsymbol{Q}\boldsymbol{c} + \boldsymbol{\mu}, \tag{7}$$

and likewise, had $\boldsymbol{x}$ been known, the linear combination of principal components best modeling it could be found by solving the linear system for $\boldsymbol{c}$. The expected sensitivity to errors in this modeling can be estimated by the condition number κ of the matrix $\boldsymbol{Q}$:

$$\kappa(\boldsymbol{Q}) = \frac{\sigma_{\max}(\boldsymbol{Q})}{\sigma_{\min}(\boldsymbol{Q})} = \frac{\sigma_1}{\sigma_k}, \tag{8}$$

which is the ratio between the maximum and minimum singular values of $\boldsymbol{Q}$. The lower the condition number, the less the sensitivity to noise and numerical errors [Ipsen and Wentworth 2014].

Recall that every $(\theta_h, \theta_d, \phi_d)$ location in the BRDF volume corresponds to a specific light/view-direction, and that every location additionally corresponds to a row in $\boldsymbol{Q}$. Therefore, the problem of determining the n best directions for sampling becomes a problem of determining the reduced matrix $\tilde{\boldsymbol{Q}} \in \mathbb{R}^{n\times k}$ of n rows from $\boldsymbol{Q}$, that minimizes the condition number $\kappa(\tilde{\boldsymbol{Q}})$.

Minimizing Condition Number: Matusik et al. [2003a] use a greedy algorithm to evaluate when the condition number of $\tilde{\boldsymbol{Q}}$ stabilizes for increasing n. The strategy is to initially pick n random rows from $\boldsymbol{Q}$ and then in a random order try to replace rows in $\tilde{\boldsymbol{Q}}$ with random rows from $\boldsymbol{Q}$, while only keeping the swaps that reduce $\kappa(\tilde{\boldsymbol{Q}})$. Our experience with this approach is that it converges very slowly for small n (see Fig. 5).

The rows of $\boldsymbol{Q}$ are formed by a vectorization of a discrete three-dimensional volume holding values that exhibit continuous variation. This means that the rows of $\boldsymbol{Q}$ are not uncorrelated, and more importantly, we can estimate the gradient of a row by looking up its neighbors in the volumetric representation. Rather than treating the rows in $\boldsymbol{Q}$ as independent and without structure, as Matusik et al.'s method does, we thus propose utilizing gradients to more effectively minimize condition number, $\kappa(\tilde{\boldsymbol{Q}})$. We found that standard numerical optimizers have difficulties in solving this minimization. This is partly due to the integer steps required when moving through the BRDF volume, and partly due to the invalid regions existing in the BRDF volume (views below horizon). We therefore develop our own simple algorithm. We start with a random initialization of $r \leq n$ sampling points (we used $r = 1$). We then randomly pick one of the points, and numerically evaluate the gradient $\nabla\kappa = \left(\frac{\delta\kappa(\tilde{\boldsymbol{Q}})}{\delta\theta_h}, \frac{\delta\kappa(\tilde{\boldsymbol{Q}})}{\delta\theta_d}, \frac{\delta\kappa(\tilde{\boldsymbol{Q}})}{\delta\phi_d}\right)$, moving along this

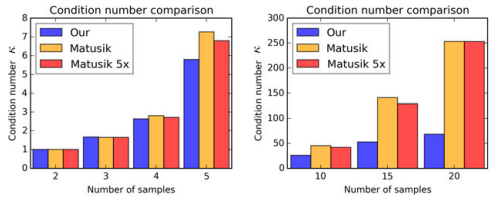

Figure 5: *Comparison of condition number for our and Matusik et al.'s method. Blue: Condition number reached by our method at convergence. Orange: condition number reached by Matusik et al.'s method using the same computation time as our method. Red: Condition number for Matusik et al.'s method using 5 times the computation time as our method.*

gradient for a pre-determined step-length. This is repeated until convergence. After convergence if $r < n$ we add a point and repeat optimization. The method was not very sensitive to step-length. We chose an initial length of 3° (3 cells), and reduced this to 1° (1 cell) when the former step-length had converged.

Algorithm: A summary of the full algorithm to minimize condition number to choose optimal sampling directions is as follows:

1. Pick $r \leq n$ random sampling locations in $(\theta_h, \theta_d, \phi_d)$. For a more robust initial guess, repeat this randomization multiple times and choose the guess that had the lowest $\kappa(\tilde{\boldsymbol{Q}})$.
2. Randomly choose one of the r points. Estimate $\nabla\kappa$ and move the point one step-length in this direction if the destination is a valid location in the BRDF volume. Otherwise, clip $\nabla\kappa$ accordingly. Repeat until convergence.
3. Optionally reduce step-length and repeat (2).
4. If $r < n$, add a new point (r++) and repeat (2).

(In the special case of $n = 1$, the condition number cannot be estimated and instead we utilize the leverage or 2-norm of the rows in $\tilde{\boldsymbol{Q}}$ as suggested by [Ipsen and Wentworth 2014].)

Validation: This approach works very well for small values of n, whereas it becomes comparable with the method of [Matusik et al. 2003a] for very large values (beyond the scope of this paper). Within our goals of minimal sampling, $n < 20$, the gains are significant as shown in Fig. 5. We use our method to find the optimum set of n rows that minimizes $\kappa(\tilde{\boldsymbol{Q}})$ and plot this (blue bar). Afterwards we run Matusik et al.'s method for the same amount of computation time and plot the obtained condition number (orange bar). Finally we let Matusik et al.'s method run for 5 times the computation time we used and plot the obtained condition number (red bar); as can be seen, the convergence of Matusik's method is slow, so additional computation time does not significantly change his results. Our condition numbers are significantly lower for $5 \leq n \leq 20$.

To evaluate if our method does in fact converge to a global minimum, we first found the ground truth global minimum by brute-force computations for $n = 2$, and then repeated the algorithm 50 times with different random initial conditions, plotting the resulting sampling locations, the minimum error sampling over all runs (the final result of our algorithm), and the ground-truth, as shown in Fig. 6. Red points indicate the first sampling direction and pink points indicate the second. The blue circles indicate the best solution found and the white stars (on top of them) indicate the global minimum found by brute force computations. The red points are

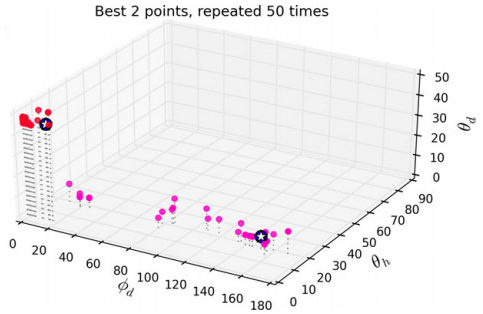

Figure 6: *Optimization repeated 50 times for $n = 2$ sampling directions. Red corresponds to first sampling direction, purple to second. The blue circles indicates the best constellation found. The two white stars indicate the ground truth global minimum found through brute-force evaluation of all combinations ($\kappa = 1.00008$). Our method is seen to correctly find the global minimum. Notice that all red points are fairly well clustered around the global minimum, indicating that our method converges well every time. A scattering is seen over ϕ_d for the purple points; this is however related to the fact that ϕ_d becomes ambiguous for $\theta_d \to 0^\circ$.*

seen to be well clustered around the global minimum. For the purple points we observe a lot of scattering over ϕ_d; this is however related to the fact that ϕ_d becomes ambiguous for $\theta_d \to 0^\circ$ as is the case here. The blue circles and white stars align, showing that we do in fact find the global minimum $\kappa = 1.0008$.

5 Reconstruction

Given a small number of samples n from an unknown BRDF, we wish to reconstruct the missing elements of the BRDF. We do this by projecting the known information into the PCA space, and by using the information of the principal components in $\boldsymbol{Q}$ to reconstruct the remaining information.

Let $\tilde{\boldsymbol{x}} \in \mathbb{R}^n$ be the vector of known values of a BRDF, let $\tilde{\boldsymbol{\mu}} \in \mathbb{R}^n$ be the vector of corresponding mean values from Equation 5, and let $\tilde{\boldsymbol{Q}} \in \mathbb{R}^{n \times k}$ be the corresponding rows of the principal components in $\boldsymbol{Q}$. The linear combination of principal components, $\boldsymbol{c}$, that best models the observed data is then obtained by:

$$\begin{aligned} (\tilde{\boldsymbol{x}} - \tilde{\boldsymbol{\mu}}) &= \tilde{\boldsymbol{Q}}\boldsymbol{c} \\ \boldsymbol{c} &= \underset{\boldsymbol{c}}{\operatorname{argmin}} \|(\tilde{\boldsymbol{x}} - \tilde{\boldsymbol{\mu}}) - \tilde{\boldsymbol{Q}}\boldsymbol{c}\|^2 \\ &= \left(\tilde{\boldsymbol{Q}}^T\tilde{\boldsymbol{Q}}\right)^{-1}\tilde{\boldsymbol{Q}}^T(\tilde{\boldsymbol{x}} - \tilde{\boldsymbol{\mu}}), \end{aligned} \tag{9}$$

and the full BRDF, $\boldsymbol{x} \in \mathbb{R}^p$, is then reconstructed by using the full principal components:

$$\boldsymbol{x} = \boldsymbol{Q}\boldsymbol{c} + \boldsymbol{\mu}. \tag{10}$$

Finally, we can apply the inverse mapping from Equation 1 to obtain the original unmapped BRDF.

Although the least squares solution above is unbiased, it usually results in severely over-fitted results, deviating significantly from ground truth. Blanz et al. [2004] addresses this issue using ridge regression and we adapt this approach for BRDFs. The length of the scaled principal components, $\boldsymbol{Q}$, is proportional to the amount of variance they explain. Hence, the magnitude of the elements in $\boldsymbol{c}$ directly links to how much a fit deviates from the mean behavior,

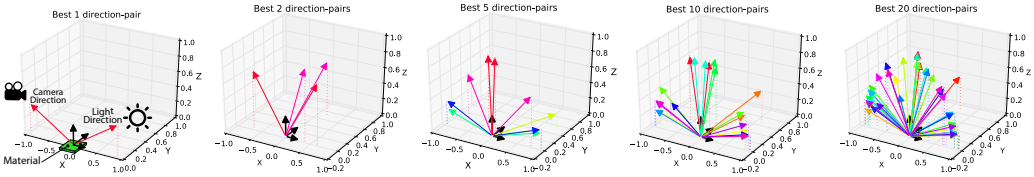

Figure 7: *Optimal sampling directions for $n = \{1, 2, 5, 10, 20\}$ samples. Each color pair corresponds to a view/illumination-combination. Notice that for a single observation, the 60° constellation is the optimum. When extending to two observations, an off-peak sampling should be performed, and continuing to 5, 10 and 20 we see that the majority of measurements should lie within the plane of incidence.*

i.e., $\|\boldsymbol{c}\|^2$ is proportional to the unlikelihood of a reconstruction. Introducing the hyper-parameter η in conjuction with the 2-norm of $\boldsymbol{c}$, it is possible to favour reconstructions closer to the observed distribution of BRDFs:

$$\boldsymbol{c} = \underset{\boldsymbol{c}}{\operatorname{argmin}} \|(\tilde{\boldsymbol{x}} - \tilde{\boldsymbol{\mu}}) - \tilde{\boldsymbol{Q}}\boldsymbol{c}\|^2 + \eta\|\boldsymbol{c}\|^2. \tag{11}$$

This expression has the closed form solution:

$$\boldsymbol{c} = \left(\tilde{\boldsymbol{Q}}^T\tilde{\boldsymbol{Q}} + \eta\boldsymbol{I}\right)^{-1}\tilde{\boldsymbol{Q}}^T(\tilde{\boldsymbol{x}} - \tilde{\boldsymbol{\mu}}), \tag{12}$$

where $\boldsymbol{I}$ is the identity matrix. As may be seen, a value of $\eta = 0$ corresponds to the least squares solution in Equation 9, and for $\eta \to \infty$, $\boldsymbol{c}$ goes to zero and the reconstruction moves towards the mean solution $\boldsymbol{\mu}$. We have found that the method is not very sensitive to the value of η; we use $\eta = 40$. For completeness we evaluated the use of L_1 penalized minimization (Lasso, [Tibshirani 1996]) to obtain a sparser set of PCs, and did not observe better performance.

Finally, recall that as mentioned in Sec. 3 color information has been removed from the training data. This means that in order to reconstruct a colored BRDF, each color channel must be reconstructed separately by Equations 10 and 12.

6 Results

Based on the optimization approach described in Sec. 4, we were able to obtain a prioritized list of optimal sampling directions for $n = \{1, 2, 5, 10, 20\}$ samples, and validate the accuracy of reconstruction using these directions for both the MERL database materials, as well as for new measured BRDFs (Sec. 7).

Optimal Sampling Directions: The optimization method was repeated 50 times in order to verify repeatability, and to enable us to pick the minimum condition-number solution. In Table 1, these directions are listed for different values of n, and they are visualized by colored pairs of arrows for view-illumination combinations in Fig. 7. We emphasize that these directions can be used directly for minimal sampling of any BRDF within a gonioreflectometer or gantry-based setup for a flat sample; the implementer need not re-run our optimization. We will also make the source code for reconstruction, principal components and mean values available online upon publication, to directly allow application of Equations 10 and 12 for BRDF reconstruction from the sparse measured samples.

Note that the computed sampling directions lie primarily in the plane of incidence and, for some measurements, resemble the aspecular directions $15^\circ, 25^\circ, 45^\circ, 75^\circ$, and 100° reported by Westlund and Meyer [2001] to be industry standards for measuring goniochromatic surfaces. Intuitively, it makes sense that the single most important measurement is at the perfect reflection around 60° c.f. Fig. 7, in order to determine the intensity of the specular peak. Likewise, for $n = 2$, we see that while the first measurement should capture the specular peak, the second measurement moves far off-peak and measures the diffuse component of the material. It is important to emphasize, as stated in the introduction, that the reported sampling directions do not cover the full variability of BRDFs. To fully capture a BRDF, generally thousands of samples are required [Lensch et al. 2003]. What these results provide are the strategically best locations to sample from in a minimal sampling setup, in order to capture as much unique information as possible per sample. Note also that these directions hold for all BRDFs, and no complex adaptive acquisition scheme is required.

n	$\theta_h[^\circ]$	$\theta_d[^\circ]$	$\phi_d[^\circ]$
1	0	66	0
2	2	40	24
	29	21	52
5	1	4	36
	77	13	86
	8	79	85
	3	74	145
	13	52	80
10	3	12	28
	63	19	89
	5	77	77
	2	60	180
	15	4	130
	1	6	37
	2	79	110
	39	76	89
	0	71	104
	5	75	180
20	9	12	69
	66	35	103
	4	76	150
	3	79	107
	33	63	105
	1	7	174
	21	8	180
	7	64	180
	6	73	180
	2	63	95
	11	11	124
	6	74	123
	1	62	129
	33	49	24
	14	71	55
	8	35	180
	31	77	91
	2	72	130
	2	47	113
	10	43	68

Table 1: *Optimium sampling directions in Rusinkiewicz coordinates [Rusinkiewicz 1998], when n BRDF samples can be acquired.*

Reconstruction Quality on MERL Database: To assess the reconstruction quality, we first describe experiments on the MERL BRDF database itself; the next section discusses validation on new samples. To avoid overfitting, the data was randomly split into two groups: 90 materials for training, and 10 materials for testing. The optimization was performed again on the reduced training-dataset and although it did not provide exactly the same directions, these were close to what was observed for the full dataset. Hence, the 10 testing materials are completely separate from the training phase.

We first evaluate the performance of the sampling directions, by comparing the reconstruction quality using the five industry standard directions reported by Westlund and Meyer [2001], with the reconstruction quality using the five optimal directions we have obtained. Using ours and Westlund and Meyer's [2001] five directions for sampling—which correspond to five known rows in $\boldsymbol{x}$ and $\boldsymbol{Q}$—the testing materials were reconstructed and the results compared to the ground truth. Fig. 8 shows the root-mean-squared error of mapped values between reconstruction and ground truth, normal-

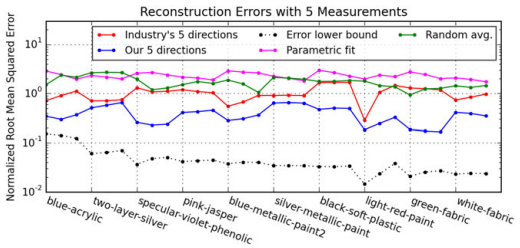

Figure 8: *RMS error of reconstruction of unknown mapped BRDFs normalized by mean mapped BRDF value, using (blue) our 5 best points of sampling, (red) 5 common industry directions [Westlund and Meyer 2001], and (dashed) all values of the BRDF. For comparison we also fitted the Ward parametric model to our 5 samples (purple), and also evaluated the average of 20 reconstructions using 5 random directions (green). Each material is represented by 3 datapoints for its R, G, and B errors.*

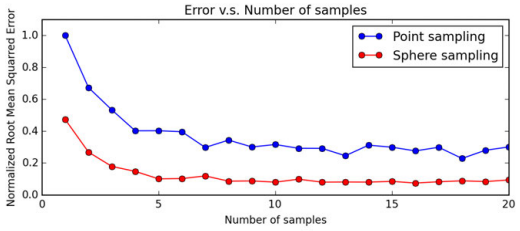

Figure 9: *Normalized average reconstruction error of unknown samples versus number of sampling directions used.*

ized by the mean mapped BRDF value, for three different reconstructions: using our five directions; using the five directions of Westlund and Meyer [2001]; using all directions ($\tilde{\boldsymbol{x}} = \boldsymbol{x}$), which is a projection of the data into PCA space and is the lower limit for the error. In addition, Fig. 8 also shows the (much higher) error of the parametric Ward model fitted to our five sampling directions (purple), as well as the average error of 20 runs where five purely random sampling directions were used. It is apparent that our proposed five directions outperform the industry sampling directions in reconstruction quality by up to an order of magnitude, and have very low error.

An evaluation of reconstruction error for an increasing number of sampling points is shown in the blue curve in Fig. 9 (the red curve for sphere sampling corresponds to Sec. 9). The figure shows the average normalized root-mean-squared error of reconstruction for the 10 testing materials, using a range of 1 to 20 sampling directions. Note that already at 4-5 samples the average error is starting to stabilize. The long tail following indicates that whereas the first samples yield great improvements to the reconstruction, latter samples only improve it slowly.

In Fig. 2, reconstructions of the 10 testing materials for an increasing number samples, $n = \{1, 2, 3, 5, 10, 20\}$, are shown. The renderings of spheres with the respective materials are done using a front light at a direction of $[1, 1, 1]$ and a back-light causing grazing angle reflections from a direction of $[-1, -1, -3]$. In addition to the low-number sampling directions, projections into PC space are also shown. These are made by fitting the principal components to the full BRDFs and illustrate the best possible reconstructions obtainable by the PCs. Finally, in the last column, reference renderings of the materials are shown. In accordance with Fig. 9, it is observed that the reconstructions stabilize after $n = 5$ samples, and at $n = 20$ there are no noticeable visual differences between the reconstruction and the reference. A single outlier is the "white-fabric" material, where the method has difficulties capturing the diffuse appearance of the material due to the strong specular prior in the data. This is addressed in Sec. 8 and a better reconstruction is shown in the last row of the figure.

In the supplementary material, we also report results on all 100 materials (without separating training and testing data) for completeness, with comparable results.

7 Validation on New Materials

To validate the reconstruction method with real data, beyond what is found in the MERL database, the in-plane BRDF of five flat samples of new materials was densely sampled using a spherical gantry. The materials evaluated were: a glossy blue book, a brown-red notebook with a smooth highlight, a specular binder-cover, a diffuse piece of green cloth, and a diffuse piece of yellow paper. We considered the BRDF at a single spatial location, the center of the sample. Note that diffuse materials are not purely Lambertian. Reference images of the five samples are shown in the lower right corners in Fig. 10. The in-plane BRDF profiles were densely sampled for all materials with a 1° resolution using a 45° incident light. In addition, the BRDF at the best 20 sampling directions, listed in Table 1, were also acquired, in order to apply our method to reconstruct the full 3D isotropic BRDF.

Using our proposed reconstruction method from Equation 12, we reconstruct the full BRDFs, using the best $n = 20$ samples. In the left column of Fig. 10, the measured in-plane BRDF values are plotted as solid curves for red, green, and blue channels. The in-plane reflectances, extracted from the full reconstructed BRDFs are plotted as dashed curves. Note that these plots are 1-D curves extracted from the full 3D BRDF volumes and as such are only very small fractions of all the data that has been reconstructed. In general, there is a very good match, indicating accurate BRDF reproduction on real samples.

The most significant deviations are observed in the 3rd reconstruction, the binder-cover, and the 4th reconstruction, the green cloth. For the binder-cover, the diffuse component remains constant much longer than what has been learned from the data as being "natural". This is most likely caused by a very isotropic subsurface scattering in the material. For the green cloth, a retroreflective behavior is observed at the incident light direction. Although retroreflective behavior is represented by a few samples in the MERL database, it is not enough to match the retroreflectivity of the cloth using the first 20 principal components. Note that overall appearance of materials is reproduced well, with very few BRDF measurements.

Renderings of the materials using the same rendering setup as in Fig. 2 are shown in the top right corners of Fig. 10. In addition, renderings of the materials using more complex geometry (Killeroo model) and high dynamic range environment lighting (Grace Cathedral, [Debevec 1998]) are in Fig. 1. Color variations are due to the different colors in the environment lighting.

8 Refinement

During reconstructions we noticed that for diffuse materials, a ringing sometimes appeared around the specular peak. This ringing is caused by the bias towards specular materials in the MERL database. This bias is not only due to a predominance of specular materials, but also due to the numerical magnitude that specular peaks have. A simple way of addressing this ringing, if needed, is

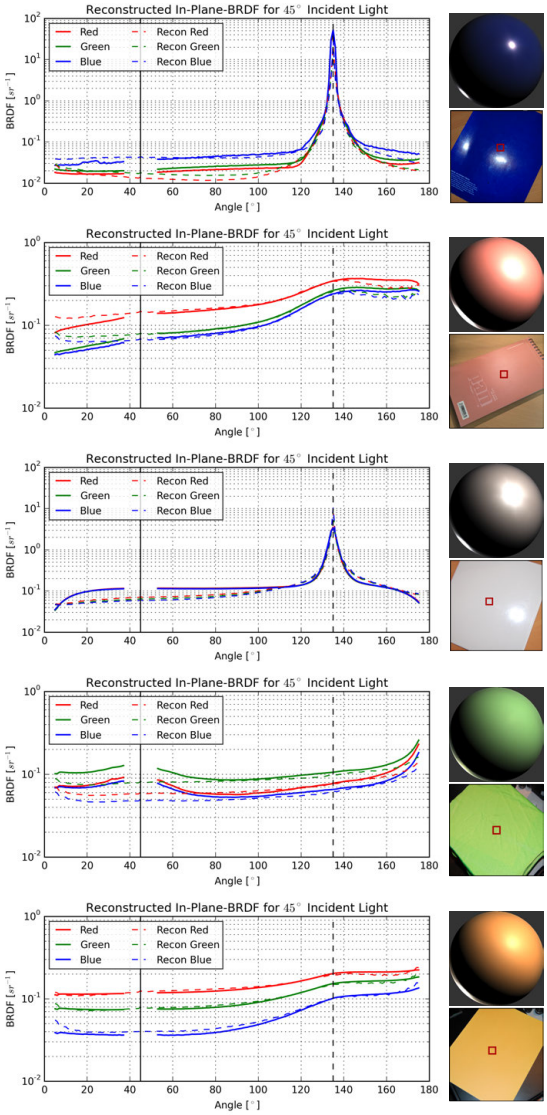

Figure 10: *Reconstruction of BRDF from five unknown materials: A glossy dark-blue book, a soft-specular notebook, a binder-cover, a piece of green cloth, and a piece of yellow paper. Lower right: reference photos of the measured materials. Upper right: renderings of reconstructed BRDFs with a front light at* $[1, 1, 1]$ *and a back light at* $[-1, -1, -3]$*. Left: Comparison between the measured in-plane BRDF values (solid) and the reconstructed in-plane BRDF values (dashed). Incident light is at* 45° *(marked as solid vertical line) and perfect reflection at* 135° *(marked with dashed vertical line). Note that these plots represent a single curve extracted from the fully reconstructed 3D BRDF volume.*

n	1	2		5				
θ_d [°]	5	4	70	4	10	31	68	75

Table 2: *Optimal sampling directions in Rusinkiewicz coordinates [Rusinkiewicz 1998], when* n *images are acquired by imaging a sphere. For each acquired image, all combinations of* (θ_h, ϕ_d) *are captured. Thus, only* θ_d *needs to be varied.*

splitting up the database into "soft" and "specular" materials, and using the respective principal components $\boldsymbol{Q}_{\text{soft}}$, and $\boldsymbol{Q}_{\text{specular}}$ to reconstruct a material. Determining if a material is specular is easily done by inspecting the magnitude of the ratio between an in-peak sample and an out-of-peak sample. This refinement procedure is not strictly needed, but does in some cases improve reconstructions. An example of this is shown in the two bottom rows of Fig. 2. Here, the reconstruction of the diffuse "white-fabric" BRDF has introduced a ringing around the specular highlight, and even at 20 samples the ringing persists. By using "soft" PCs the artifact is effectively removed, producing convincing results with as few as 3 BRDF measurements.

9 Extension to Image-Based BRDF Capture

An effective way of capturing multiple BRDF samples per image is from spheres of a homogeneous material [Marschner et al. 2000]. This is how the extensive MERL database was captured [Matusik et al. 2003b], and is an approach that is often used today. This of course puts a constraint on the types of BRDFs possible to capture, as not all materials can be cut or molded into perfect spheres.

For any angle $\theta_d \leq 90^\circ$ between camera and lightsource, an image of a perfect sphere covers all surface normal orientations in the positive hemisphere. An interesting observation is that an image of an illuminated sphere (with $\theta_d \leq 90^\circ$) actually corresponds to a 2D slice of the 3D Rusinkiewicz coordinate frame (θ_h, ϕ_d) at θ_d. Hence, to capture the full 3D isotropic BRDF, only a sweep over θ_d must be made. This leads to a natural extension of our work, namely in determining the best n slices through the BRDF-volume, corresponding to the best n angles between camera and illumination when capturing a BRDF from an image of a spherical material.

We modify the optimization algorithm in Sec. 4. Where a measurement in the point-sampling setup corresponds to a single location in the BRDF volume and a single row in $\boldsymbol{Q}$, a measurement in a spherical-sampling setup corresponds to many rows in $\boldsymbol{Q}$. For a given angle θ_d, let $\mathcal{L}(\theta_d)$ be the set of BRDF locations, $(\theta_h, \theta_d, \phi_d)$, visible on the sphere. $\tilde{\boldsymbol{Q}}$ will now include the set of rows in $\boldsymbol{Q}$ corresponding to $\mathcal{L}(\theta_d)$ for each of the n measurements. In this case, the condition number κ depends only on the θ_d values, so that $\nabla\kappa = \frac{\delta\kappa(\tilde{\boldsymbol{Q}})}{\delta\theta_d}$. Using the new $\tilde{\boldsymbol{Q}}$ and $\nabla\kappa$, the optimization in Sec. 4 is again used to find the optimal sampling directions θ_d.

Our results are presented in Table 2 and visualized in Fig. 11. It is seen that the single most important sample is of the oblique angle reflection of the material (low θ_d). The second most important sample is the grazing angle reflection (high θ_d). For additional samples, we observe a spreading over all angles, but with a predominance at low and high values of θ_d.

As with the point-sampling setup, we qualitatively evaluate the reconstructions of the 10 test materials. The results are shown in Fig. 12 for $n = \{1, 2, 5\}$ sampling directions. After only two images, appearance is accurately captured for all materials. A quantitative analysis (red error graph in Fig. 9) confirms this, and shows that almost optimal reconstruction is achieved with 5 images. In agreement with Table 2, the first image captures the correct oblique angle appearance (first column of Fig. 12) and the second image captures the correct grazing angle appearance (second column). We

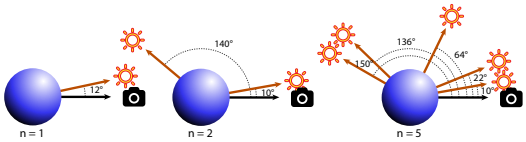

Figure 11: *Optimal sampling directions for spheres with $n = \{1, 2, 5\}$ images. Black arrows denote the direction to the camera. Orange arrows denote the direction to the light-source (due to reciprocity these may be interchanged). Notice that θ_d is the angle to the half-vector; the angle between view and light is $2\theta_d$.*

also performed a comparison to randomly chosen sampling directions. Intuitively, with more samples available from an image, the difference in error should be lower than for point sampling. We observe that random sampling results in roughly 35% higher errors for up to $n = 5$, after which it converges, approaching our error, again indicating again that 5 images are sufficient for reconstruction.

For a final validation we used the Cornell Reflectance database [Foo 1997] to simulate additional θ_d slices completely uncorrelated with the MERL data. These are shown in the last 3 rows.

10 Conclusions and Future Work

In this paper, we have developed a method for optimal, minimal sampling of BRDFs. Perhaps surprisingly, we show that $n = 20$ individual measurements is adequate in most cases for accurate isotropic BRDF reconstuction, and $n = 2$ images suffices for image-based BRDF measurements of spherical samples.

Our method leverages the MERL database [Matusik et al. 2003a], and proposes a novel mapping of BRDFs, allowing extraction of very descriptive principal components. A reconstruction approach based on ridge-regression, that utilizes the learned principal components, is described. We believe we are the first to present a BRDF reconstruction method that utilizes the statistical likelihood of a synthesized BRDF through the magnitude of the eigenvalue-scaled principal components. This approach yields better reconstructions than previous methods, and may have broader applicability.

We also develop a method for determining the regions of greatest importance, to sample the BRDFs. We provide an explicit table of the strategically best $n = \{1, 2, 5, 10, 20\}$ directions for sampling any unknown BRDF, and validate our results against previous industry standard sets of directions, as well as with measurements on new BRDFs not in the MERL database. We also show how the approach can be extended to sampling spheres via image-based BRDF measurement. In that case, two images often suffice.

In the future, the approach could also be extended to other acquisition geometries and customized for a particular gantry setup and near-field views of a homogeneous flat sample, where multiple light-view directions are available in a single image. Another interesting extension is to allow for capturing spatially varying BRDFs, since most gonioreflectometers are equipped with cameras. Our prioritized lists could also be used for importance sampling general BRDFs for rendering. The descriptive principal components may also be useful in editing and synthesizing novel BRDFs. In summary, we believe our results take an important step towards making rapid acquisition of data-driven reflectance models more practical in many applications.

Learned principal components, lists for $n = [1, 50]$ sampling directions, sample code, and reconstructed BRDFs, can be downloaded from our website: `http://brdf.compute.dtu.dk`.

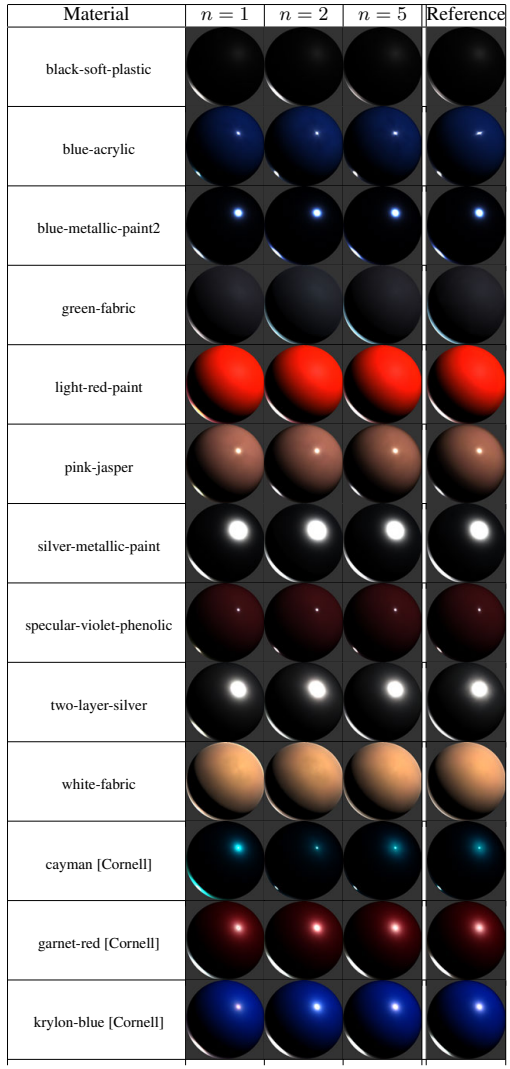

Figure 12: *Reconstructions of test samples, simulating BRDF capture using a sphere [Marschner et al. 2000]. The BRDFs are rendered as spheres, illuminated by a front light at a direction of $[1, 1, 1]$, and a back light causing grazing angle reflections at $[-1, -1, -3]$. Reconstructions are made with $n = \{1, 2, 5\}$ sampling directions. The far right column shows reference renderings of the true BRDFs. We see that two measurements (images) are sufficient to capture the true appearance of a material. The bottom 3 rows show materials from the Cornell Database [Foo 1997].*

Acknowledgements

This work was funded in part by NSF grants 1451828, 1451830 and the UC San Diego Center for Visual Computing. We thank Chiwei Tseng for acquiring some of the materials in Fig. 10.

References

AITTALA, M., WEYRICH, T., AND LEHTINEN, J. 2013. Practical SVBRDF capture in the frequency domain. *ACM Transactions on Graphics (TOG) 32*, 4, 110.

BLANZ, V., MEHL, A., VETTER, T., AND PETER SEIDEL, H. 2004. A Statistical Method for Robust 3D Surface Reconstruction from Sparse Data. In *3D Data Processing Visualization and Transmission*, 293–300.

BLINN, J. F. 1977. Models of light reflection for computer synthesized pictures. In *SIGGRAPH 77*, 192–198.

BRADY, A., LAWRENCE, J., PEERS, P., AND WEIMER, W. 2014. genBRDF: discovering new analytic BRDFs with genetic programming. *ACM Transactions on Graphics (TOG) 33*, 4, 114.

BURLEY, B. 2012. Physically based shading at Disney. In *Practical physically-based shading in film and game production*, S. Hill and S. McAuley, Eds., ACM SIGGRAPH Courses. Article 10.

COOK, R. L., AND TORRANCE, K. E. 1982. A reflectance model for computer graphics. *ACM Transactions on Graphics (TOG) 1*, 1, 7–24.

DANA, K. J., AND WANG, J. 2004. Device for convenient measurement of spatially varying bidirectional reflectance. *J. Opt. Soc. Am. A 21*, 1, 1–12.

DEBEVEC, P. 1998. Rendering synthetic objects into real scenes: Bridging traditional and image-based graphics with global illumination and high dynamic range photography. In *SIGGRAPH 98*, 189–198.

FOO, S. C. 1997. *A gonioreflectometer for measuring the bidirectional reflectance of material for use in illumination computation*. Master's thesis, Cornell University.

FUCHS, M., BLANZ, V., LENSCH, H. P., AND SEIDEL, H.-P. 2007. Adaptive sampling of reflectance fields. *ACM Transactions on Graphics (TOG) 26*, 2, 10.

GHOSH, A., ACHUTHA, S., HEIDRICH, W., AND O'TOOLE, M. 2007. BRDF acquisition with basis illumination. In *International Conference on Computer Vision*, 1–8.

HERTZMANN, A., AND SEITZ, S. M. 2003. Shape and materials by example: A photometric stereo approach. In *Computer Vision and Pattern Recognition*, vol. 1, IEEE, 533.

HULLIN, M. B., HANIKA, J., AJDIN, B., SEIDEL, H.-P., KAUTZ, J., AND LENSCH, H. 2010. Acquisition and analysis of bispectral bidirectional reflectance and reradiation distribution functions. *ACM Transactions on Graphics (TOG) 29*, 4, 97.

HUNTER, R. S., AND JUDD, D. B. 1939. Development of a method of classifying paints according to gloss. *ASTM Bulletin*, 97, 11–18.

HUNTER, R. S. 1987. *The measurement of appearance*. John Wiley & Sons.

IPSEN, I. C. F., AND WENTWORTH, T. 2014. The effect of coherence on sampling from matrices with orthonormal columns, and preconditioned least squares problems. *SIAM J. Matrix Analysis Applications 35*, 4, 1490–1520.

LAFORTUNE, E., FOO, S., TORRANCE, K., AND GREENBERG, D. 1997. Non-Linear Approximation of Reflectance Functions. In *SIGGRAPH 97*, 117–126.

LENSCH, H. P. A., LANG, J., S, A. M., AND PETER SEIDEL, H. 2003. Planned sampling of spatially varying BRDFs. *Computer Graphics Forum 22*, 3, 473–482.

LÖW, J., KRONANDER, J., YNNERMAN, A., AND UNGER, J. 2012. BRDF models for accurate and efficient rendering of glossy surfaces. *ACM Transactions on Graphics (TOG) 31*, 1, 9.

MARSCHNER, S., WESTIN, S., LAFORTUNE, E., TORRANCE, K., AND GREENBERG, D. 2000. Image-Based BRDF Measurement including Human Skin. In *Eurographics Rendering Workshop*, 139–152.

MATUSIK, W., PFISTER, H., BRAND, M., AND MCMILLAN, L. 2003. A data-driven reflectance model. In *ACM Transactions on Graphics (TOG)*, 759–769.

MATUSIK, W., PFISTER, H., BRAND, M., AND MCMILLAN, L. 2003. Efficient isotropic BRDF measurement. In *Eurographics Rendering Workshop*, 241–247.

NGAN, A., DURAND, F., AND MATUSIK, W. 2005. Experimental analysis of BRDF models. In *Eurographics Symposium on Rendering*, 117–126.

NGAN, A., DURAND, F., AND MATUSIK, W. 2006. Image-driven navigation of analytical BRDF models. In *Eurographics Symposium on Rendering*, 399–407.

NICODEMUS, F. E., RICHMOND, J. C., HSIA, J. J., GINSBERG, I. W., AND LIMPERIS, T. 1977. *Geometric Considerations and Nomenclature for Reflectance (NBS Monograph 160)*. National Bureau of Standards (US).

NOLL, T., STRICKER, D., KOHLER, J., AND REIS, G. 2013. A full-spherical device for simultaneous geometry and reflectance acquisition. In *Proceedings of the on Applications of Computer Vision*, IEEE Computer Society, WACV, 355–362.

PHONG, B. T. 1975. Illumination for computer generated pictures. *Communications of the ACM 18*, 6, 311–317.

REN, P., WANG, J., SNYDER, J., TONG, X., AND GUO, B. 2011. Pocket reflectometry. *ACM Transactions on Graphics (TOG) 30*, 4, 45.

ROMEIRO, F., AND ZICKLER, T. 2010. Blind reflectometry. In *European Conference on Computer Vision*. 45–58.

ROMEIRO, F., VASILYEV, Y., AND ZICKLER, T. 2008. Passive reflectometry. In *European Conf. on Computer Vision*, 859–872.

RUSINKIEWICZ, S. 1998. A new change of variables for efficient BRDF representation. In *Eurographics Rendering Workshop*, 11–22.

SCHWARTZ, C., SARLETTE, R., WEINMANN, M., RUMP, M., AND KLEIN, R. 2014. Design and implementation of practical btf measurement devices focusing on the developments at the university of Bonn. *Sensors 14*, 5, 7753–7819.

TIBSHIRANI, R. 1996. Regression shrinkage and selection via the lasso. *Journal of the Royal Statistical Society. Series B (Methodological) 58*, 267–288.

TORRANCE, K. E., AND SPARROW, E. M. 1967. Theory for off-specular reflection from roughened surfaces. *JOSA 57*, 9, 1105–1112.

TUNWATTANAPONG, B., FYFFE, G., GRAHAM, P., BUSCH, J., YU, X., GHOSH, A., AND DEBEVEC, P. 2013. Acquiring reflectance and shape from continuous spherical harmonic illumination. *ACM Transactions on Graphics (TOG) 32*, 4, 1–12.

WARD, G. J. 1992. Measuring and modeling anisotropic reflection. In *SIGGRAPH 92*, 265–272.

WESTLUND, H. B., AND MEYER, G. W. 2001. Applying appearance standards to light reflection models. In *SIGGRAPH 01*, 501–510.

WEYRICH, T., MATUSIK, W., PFISTER, H., BICKEL, B., DONNER, C., TU, C., MCANDLESS, J., LEE, J., NGAN, A., JENSEN, H. W., AND GROSS, M. 2006. Analysis of human faces using a measurement-based skin reflectance model. *ACM Transactions on Graphics (TOG) 25*, 3, 1013–1024.

WHITE, D., SAUNDERS, P., BONSEY, S. J., VAN DE VEN, J., AND EDGAR, H. 1998. Reflectometer for measuring the bidirectional reflectance of rough surfaces. *Applied optics 37*, 16, 3450–3454.

Appendix E

Contribution C.V: Anatomically Correct Surface Recovery

Anatomically Correct Surface Recovery: A Statistical Approach

Rasmus R. Jensen( ), Jannik B. Nielsen,
Rasmus Larsen, and Rasmus R. Paulsen

DTU Compute, Technical University of Denmark, Richard Petersens Plads,
Building 324, 2800 Kgs. Lyngby, Denmark
{raje,jbol,rlar,rapa}@dtu.dk
http://www.compute.dtu.dk

Abstract. We present a method for 3D surface recovery in partial surface scans. The method is based on an Active Shape Model, which is used to predict missing data. The model is constructed using a bootstrap framework, where an initially small collection of hand-annotated samples is used to fit to and register unknown samples, resulting in an extensive statistical model. The statistical recovery uses a multivariate point prediction, where the distribution of the points is given by the Active Shape Model. We show how missing data in a partial scan, once point correspondence is achieved, can be predicted using the learned statistics. A quantitative evaluation is performed on a data set of 10 laser scans of ear canal impressions with minimal noise and artificial holes. We also present a qualitative evaluation on authentic partial scans from an actual direct in ear scanner prototype. Compared to a state-of-the-art surface reconstruction algorithm, the presented method gives matching prediction results for the synthetic evaluation samples and superior results for the direct scanner data.

Keywords: Surface recovery · Hole closing · Multivariate statistics · Shape modeling · In ear scanning · Active shape model

1 Introduction

Direct surface scanning of humans is an increasingly used modality where the applications include model creation in the entertainment industry, plastic surgery planning and evaluation, craniofacial syndrome evaluation [10,14], and in particular hearing aid production. In this paper, we are concerned with a particular surface shape namely that of the ear canal. Ear canal surface scans are used in custom hearing aid fitting. This is a very large industry that probably makes the ear the most scanned part of the human anatomy. A standard hearing aid producer generates more than a thousand scans per week. When producing custom in-the-ear devices like hearing aids and monitors, the standard routine is to inject silicone rubber into the patients ear and then laser scan this impression. While this technique normally creates complete surfaces, direct ear scanners are

© Springer International Publishing Switzerland 2015
R.R. Paulsen and K.S. Pedersen (Eds.): SCIA 2015, LNCS 9127, pp. 212–223, 2015.
DOI: 10.1007/978-3-319-19665-7_18

emerging and it is expected that probe scans with these devices will require handling of missing data due to occlusion in the complex anatomy of the human ear and the limited space for the scanner probe. In this paper we present a method for predicting missing data based on the information in the partial scan. Hole filling and missing data recovery is a well studied problem, in particular for 2D images. In 3D, data recovery is sometimes considered a by-product of the surface reconstruction algorithm. The algorithms used to generate triangulated surfaces from point clouds will usually try to cover missing areas using some mathematical or physical assumptions. One series of approaches uses Delaunay triangulation of border points [12]. Such methods are obviously susceptible to noise in the border points and will typically require some form of smoothing. An alternative strategy is to interpolate implicit (signed distance) functions locally or globally under various forms of regularisation [11,18]. Other methods, inspired from 2D inpainting approaches have also been investigated [6,7,20]. These are typically based on a variational definition of the behavior of the surface where the holes are.

In our method, we predict the missing points based on the existing points in the scan. Instead of using variational formulations or physical assumptions on the behaviour of the surface, we utilise population statistics of the given class of surfaces learned from an annotated and co-registered training set. We base our population statistics of the ear canal on an extensive statistical shape model of the ear canal constructed in a bootstrap framework. The method is general and is applicable to all surface scans, where a statistical shape distribution can be estimated. The 3D morphable models introduced for the analysis and synthesis of 3D faces [5] can also be used to recover missing data in surface scans [4]. In [5] a 3D statistical shape and texture model is built based on a set of registered training samples and from this a principal component analysis is performed giving a set of eigenvectors and values. To recover missing data the set of known points are found in a pre-processing step and the missing data points are found by computing the optimal linear combination of eigenvectors fitting the known data. This is combined with a ridge regression regularisation to avoid non-plausible shapes. The approach described in [5] is similar to our prediction step, but in contrast we also include the steps needed to identify the missing points in the described framework. Furthermore, we also weight the geodesic distance from the missing points to the known points in the prediction.

1.1 Data and Preprocessing

The data consists of 310 scanned left-ear impressions. The scans have been acquired from a traditional 3D scanner, resulting in meshes of arbitrary triangulation. From this collection, 12 representatives are chosen and from these point correspondence over the selected impressions is created using the method initially described in [17]. Furthermore, the Markov Random Field regularization of the correspondence field described in [16] was used to further optimize the dense correspondence. This small subset of impressions with point correspondence form the basis for the bootstrapping framework. This is used to encompass

the entire collection of ear impressions, with the goal of constructing a statistical shape model as for example described in [8,17]. The method described in [17] requires manual annotation of anatomical landmarks which is non-trivial and therefore an automated method is preferred. A small collection of scans have been acquired by a prototype in-ear 3D scanner[1]. They are partial in the sense that some areas of the surface are missing due to noise and/or occlusion. Finally, a small set of scanned ear-impressions, not part of the original 310 samples, have had holes cut in them to mimic the nature of the partial scans. We denote these manually created partial scans as synthesized partial scans. This set is used for controlled evaluation of our method. In the following, some parameters have been assigned fixed values manually chosen for our data. These parameters should be validated for other uses of the framework.

2 Bootstrapped Active Shape Model

In order to accurately recover missing information in a partial scan we construct a statistical shape model [8]. For this, point correspondence is needed over the training set. Initially a small subset of samples is manually annotated and registered using the approach described in [16,17]. Using this subset, an Active Shape Model (ASM) is constructed as described in [8,17]. The statistical model is aligned and fitted to each unknown sample. This is done iteratively, allowing co-registration to and inclusion in the ASM, thereby expanding the model sample by sample. The ASM thus grows in size as the bootstrapping procedure processes unknown samples, allowing it to explain an increasing amount of shape variation from the dataset. Intuitively this leads to the expectation that the algorithm will become increasingly better at fitting to unknown shapes and that later samples are better registered than former, wherefore a revisit of early registrations may be chosen as a finalising step.

Assuming a collection of m aligned shapes, each consisting of p 3D points $\mathbf{v}_i = (x_1, y_1, z_1, \ldots, x_p, y_p, z_p)^T \in \mathbb{R}^n$. These shapes can be interpreted as being points in an $n = 3p$-dimensional space. The average shape is thus $\bar{\mathbf{v}} = \frac{1}{m}\sum_{i=1}^{m} \mathbf{v}_i$ and the shape deviation from mean $\mathbf{x}_i = \mathbf{v}_i - \bar{\mathbf{v}}$. In order to investigate the variation of the data, an observation matrix $\mathbf{X} = (\mathbf{x}_1, \ldots, \mathbf{x}_m) \in \mathbb{R}^{n \times m}$ can be constructed. The covariance matrix, $\mathbf{\Sigma}$, of $\mathbf{X}$ is found by

$$\mathbf{\Sigma} = \frac{1}{m}\mathbf{X}\mathbf{X}^T \in \mathbb{R}^{n \times n}. \tag{1}$$

Performing an Eigenvalue decomposition of this covariance matrix, thus provides insight in the primary modes of variation within the dataset $\mathbf{\Sigma} = \mathbf{P}\Lambda\mathbf{P}^T$, where $\mathbf{P} = (\mathbf{p}_1, \ldots, \mathbf{p}_m)$ is a matrix consisting of columns of Eigenvectors and $\Lambda = \mathrm{diag}(\lambda_1, \ldots, \lambda_m)$ is a diagonal matrix holding the Eigenvalues. These Eigenvalues corresponds to the variation expressed of the respective Eigenvector directions, i.e. $\lambda_i = \sigma_i^2$. In scenarios where $m < n$, only a subset of the Eigenvalues will be non-zero, the size of this subset will be denoted m'.

Given the collection of non-zero Eigenvalues and corresponding Eigenvectors described above, these can be used as a basis. Any shape $\tilde{\mathbf{v}}$ can then be synthesised by a linear combination of the Eigenvectors, weighted by their Eigenvalues:

$$\mathcal{M}(\mathbf{c}) = \tilde{\mathbf{v}} = \sum_{i}^{m'} c_i \lambda_i \mathbf{p}_i = \mathbf{P}\Lambda\mathbf{c}, \tag{2}$$

where $\mathbf{c} = (c_1, \ldots, c_{m'})$ is a vector of weights determining how much the individual Eigenvectors contributes in the synthesis. This constitutes the Active Shape Model and hereby the ASM can be interpreted as a function of the weights in $\mathbf{c}$, i.e. $\mathcal{M}(\mathbf{c})$.

The raw samples to be included in the ASM may not be positioned or oriented correctly relative to each other. Multiple approaches to automatic alignment of shapes exists, we have chosen to use 3D Shape Context Descriptors [9].

The descriptors describes a point on a 3D surface by a histogram of its local neighbourhood, indicating the local geometric distribution of points. Given a point $\mathbf{q}$ on a surface, any neighbouring point's relative position to $\mathbf{q}$ can be expressed in spherical coordinates (r, θ, φ). Here r is the radial distance between $\mathbf{q}$ and a neighbour $\mathbf{q}_n$. The inclination angle θ and the azimuthal angle φ requires a choice of reference-frame in order to be intercomparable between differently aligned samples. In this experiment, 3D data were acquired from a laser scanner using a rotating platform. The 3D representations of the ear impressions thus have a consistent vertical axis. This consistency can be utilised to construct a common frame of reference. In this frame of reference the third basis element is aligned with the normal of the point $\mathbf{q}$. This is formulated as $\mathbf{b}_3 = \mathbf{n}_\mathbf{q} = (n_x, n_y, n_z)^T$. The first basis element is aligned with the vertical axis, with the restraint of being orthogonal to $\mathbf{b}_3$. Denoting a vector pointing along the fixed vertical axis $\mathbf{v} = (0, 1, 0)^T$, this is found by $\mathbf{b}_1 = \mathbf{v} - (\mathbf{v} \cdot \hat{\mathbf{b}}_3)\hat{\mathbf{b}}_3$, i.e. a vector rejection of $\mathbf{v}$ on $\mathbf{n}_\mathbf{q}$, where $\hat{\mathbf{b}}$ denotes the normalised value of $\mathbf{b}$. As a result of orthogonal basis vectors in a right-handed coordinate-system, the second basis element is thus restrained to being $\mathbf{b}_2 = \mathbf{b}_3 \times \mathbf{b}_1$. From this basis, a rotation matrix, rotating to the local frame of reference can be constructed $\mathbf{R} = \left[\hat{\mathbf{b}}_1\ \hat{\mathbf{b}}_2\ \hat{\mathbf{b}}_3\right]$. Any neighbouring point, $\mathbf{q}_n$, can thus be described in $\mathbf{q}$'s local frame of reference by $\tilde{\mathbf{q}}_n = \mathbf{R}(\mathbf{q}_n - \mathbf{q})$. Within this frame of reference, the inclination angle and the azimuthal angle of the point is given by $\theta = \arccos(\tilde{q}_{n,z}/r)$ and $\varphi = \arctan(\tilde{q}_{n,y}/\tilde{q}_{n,x})$.

Based on the coordinates (r, θ, φ), points in the proximity of $\mathbf{q}$ can be grouped in a discrete set of bins. Hereby a histogram over the 3-dimensional distribution of points surrounding $\mathbf{q}$ can be constructed and used as a feature vector. In our experiment, (r, θ, φ) of points within a radius of 10 mm were divided into $(8, 13, 4)$ bins respectively, yielding a 416-dimensional feature vector or Shape Context Descriptor. The choice of utilising the vertical axis to construct a common frame of reference poses a constraint on the geometry as points having normals parallel to the vertical axis cannot be used. In practice this means that perfectly horizontal surfaces cannot be evaluated. Through the Hungarian method [13], point-descriptors

are matched and based on this matching a corresponding transformation can be computed in a least squares sense. The standard χ^2 histogram distance is used as cost function [3]. An illustration is shown in Fig 1. The resulting set of matched points is used to compute the optimal translation and rotation in a least squares sense [9].

Using this method, unknown samples are aligned to the mean of the ASM, $\bar{\mathbf{v}}$, thus supplying a plausible pre-alignment. Failed pre-alignments are easily detected by evaluating the average Euclidean point to point distance between the mean shape and the aligned shape. In our dataset, alignments with average point-to-point distances above 5 mm are rejected.

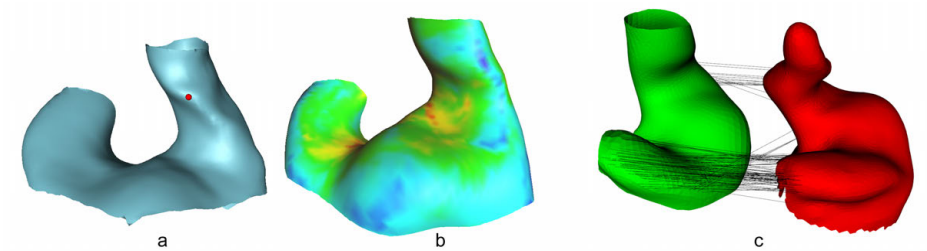

Fig. 1. The descriptor in the point marked by the red marker in a) is compared to the descriptors in all points of b). Colouring in b) corresponds to the χ^2 distance between the descriptors. c) Lines indicating the 100 most significant Shape Context matches between the two samples.

Given a roughly aligned unknown sample, $\mathbf{v}_a$, the alignment is refined and the ASM, $\mathcal{M}(\mathbf{c})$, is fitted. This is done in an iterative manner, where an Iterative Closest Point (ICP) [19] alignment of the sample is followed by an ASM-fitting of the model, and repeated upon until convergence is met. In our ICP implementation the points from the ASM surface are matched to their nearest surface neighbours on the new sample, with the constraint that points connected to a border should be ignored.

For the fitting, we seek to find a deformation of the Active Shape Model that minimises the error between the model and the unknown sample. An ASM constructed from the shape analysis of m samples, each consisting of n points, will be parametrised in an m'-dimensional space and thus have m' modes of variation.

Let $\mathbf{q}_i \in \mathbb{R}^3$ be a point belonging to the ASM, $\mathcal{M}(\mathbf{c})$, and let $\mathbf{q}'_i \in \mathbb{R}^3$ be the closest point on the target sample surface $\mathbf{v}_a$. We seek to find the set of weights $\mathbf{c}^*$ that minimises the sum of distances between $\mathbf{q}$ and $\mathbf{q}'$:

$$\arg\min_{\mathbf{c}} \|\mathcal{M}(\mathbf{c}) - \mathbf{v}_a\| = \arg\min_{\mathbf{c}} \frac{1}{m'} \sum_{i=1}^{m'} \|\mathbf{q}_i - \mathbf{q}'_i\| \tag{3}$$

We solve this optimisation problem by utilising an implementation of the Nelder-Mead method [15]. We reduced the number of parameters used to a number

corresponding to 99% explained variance af the training data. As the model-fitting is basically a synthesisation from a k-dimensional (assumed) normal-distribution, a confidence level for an obtained set of parameters $\mathbf{c}^*$ can thus be computed by utilising the Mahalanobis distance M between the parameter set and the ASM distribution since $M^2 \sim \chi^2_n$. This allows validation of fittings by setting a reasonable confidence limit. In our implementation, a confidence level of 99.9% was used.

Having determined $\mathbf{c}^*$ for $\mathcal{M}$ and $\mathbf{v}_a$, the model mesh $\mathcal{M}(\mathbf{c}^*) = \tilde{\mathbf{v}}$ is propagated to the sample shape $\mathbf{v}_a$ in order to perform a point-wise registration using the procedure described in [16]. The result is a mesh of p points, following the shape of $\mathbf{v}_a$, all with correspondence to the model, $\mathcal{M}$. The quality of the registration is determined by computing the 20^{th} percentile of the minimum angle in the projected triangles and rejecting registration where this is below 15°. This measure is valid since the model mesh has been optimised and has near equilateral triangles. Secondly, the normals of the projection are compared to the normals of $\tilde{\mathbf{v}}$. Registrations having an average dot-product between the normals of $\tilde{\mathbf{v}}$ and the projection below 0.75 are rejected.

When an alignment and a registration is obtained using the iterative scheme above, they are both refined iteratively. During each iteration the registration-mesh is smoothed using simple meaning of the nearest neighbours. The surface normals of the smoothed mesh are found and regularised using local averaging of directions. A new set of correspondence points are found in the sample scan in the direction of the regularised normals and the alignment, $\mathbf{v}_a$, is adjusted accordingly. This process is repeated until convergence. As the sample input scan is expected to be more densely sampled than $\mathcal{M}(\mathbf{c}^*)$ the iterative update ensures a regular mesh with evenly distributed vertices. Each sample that is successfully fitted is added to the ASM. ASM is hereby improved to cover additional shape variation.

3 Surface Recovery on Partial Scans

As described, a crucial, and not easily solved, part of recovering missing data is to co-register a partial mesh with the ASM. This is required in order to obtain point-correspondence between model and surface, creating a partial scan with a mesh structure identical to that of the model. The process of co-registering an unknown scan to the ASM is basically addressed in section 2. In the case of reconstructing partial scans, however, the exact same approach may not suffice. This is mainly due to the fact that an automatic alignment between a partial scan and model may prove to be difficult for Shape Context features. The difficulties arise in scenarios where the key shape features of the model are not present on the scan or vice-versa. We limit ourselves to the already existing Shape Context alignment approach, and where this failed, manual alignment was used. The result of registering and fitting the ASM to a partial scan is that the ASM template mesh is deformed and propagated to the partial scans in areas where there are valid data. The template mesh vertices are marked as missing when

the corresponding point or area in the partial scan is not present or valid. If an area is missing in the partial scan, the point projection will often result in that the project point is placed on a boundary in the partial scans, thus enabling detection of missing point correspondences. Given a registration, we aim to recover missing surface data in a partial scan such that the recovered data are anatomically correct. We approach this by using a statistical model and define the set of known and unknown data in a partial scan as follows:

$$\begin{aligned} \text{missing vertices: } \mathbf{s}_1^{\mathrm{T}} &= (x_{11}, y_{11}, z_{11}, x_{12}, y_{12}, z_{12}, \ldots) \\ \text{known vertices: } \mathbf{s}_2^{\mathrm{T}} &= (x_{21}, y_{21}, z_{21}, x_{22}, y_{22}, z_{22}, \ldots) \end{aligned}$$

The correspondence allows for differentiation between known vertices and missing vertices in the partial scan. We will determine how the unknown data $\mathbf{s}_1$ are predicted from known vertices in $\mathbf{s}_2$. Without any prior knowledge of the distribution of data, we consider a shape $\mathbf{s}$ consisting of $\mathbf{s}_1$ and $\mathbf{s}_2$ as belonging to the normal distribution:

$$\mathbf{s} = \begin{bmatrix} \mathbf{s}_1 \\ \mathbf{s}_2 \end{bmatrix} \in N\left(\begin{bmatrix} \mu_1 \\ \mu_2 \end{bmatrix}, \begin{bmatrix} \mathbf{\Sigma}_{11} & \mathbf{\Sigma}_{12} \\ \mathbf{\Sigma}_{21} & \mathbf{\Sigma}_{22} \end{bmatrix} \right) \ , \ \mathbf{\Sigma}_{12}^{\mathrm{T}} = \mathbf{\Sigma}_{21} \tag{4}$$

The expected value of $\mathbf{s}_1$ given $\mathbf{s}_2$ is $\mathrm{E}\{\mathbf{s}_1|\mathbf{s}_2\} = \mu_1 + \mathbf{\Sigma}_{12}\mathbf{\Sigma}_{22}^{-1}(\mathbf{s}_2 - \mu_2)$. With the variance $\mathrm{V}\{\mathbf{s}_1|\mathbf{s}_2\} = \mathbf{\Sigma}_{11} - \mathbf{\Sigma}_{12}\mathbf{\Sigma}_{22}^{-1}\mathbf{\Sigma}_{21}$ From the ASM we get an aligned set of shapes. This training set is denoted $X_{aligned}$. From the training set the covariances $\mathbf{\Sigma}_{11}$ and $\mathbf{\Sigma}_{12}$ as well as the means (μ_1, μ_2) are learned. As there are far less shapes than points, $\mathbf{\Sigma}_{22}$ will be singular. Let $\mathbf{\Sigma}_{22} = \mathbf{P}\Lambda\mathbf{P}^{\mathrm{T}}$ be the Eigenvalue decomposition. We restrict $\mathbf{\Sigma}_{22}$ to its affine support, i.e. the dimensions spanned by the Eigenvectors corresponding to the k positive Eigenvalues, such that $\mathbf{\Lambda}^* = \mathrm{diag}(\lambda_1, \lambda_2, \ldots, \lambda_k)$ and $\mathbf{P}^* = [\mathbf{p}_1\ \mathbf{p}_2\ \ldots\ \mathbf{p}_k]$. The projection of $\mathbf{s}_2$ using the k selected Eigenvectors $\mathbf{P}^*$: $\mathbf{y}_2 = {\mathbf{P}^*}^{\mathrm{T}}\mathbf{s}_2$ has affine support for $\mathbf{s}_2$ and the variance:

$$\mathrm{V}\{\mathbf{y}_2\} = \mathrm{V}\{\mathbf{P}^*\mathbf{s}_2\} = {\mathbf{P}^*}^{\mathrm{T}}\mathbf{\Sigma}_{22}\mathbf{P}^* = \mathbf{\Lambda}^* \tag{5}$$

The covariance of $\mathbf{s}_1$ and $\mathbf{y}_2$ is:

$$\mathrm{C}\{\mathbf{s}_1, \mathbf{y}_2\} = \mathrm{C}\{\mathbf{s}_1, {\mathbf{P}^*}^{\mathrm{T}}\mathbf{s}_2\} = \mathrm{C}\{\mathbf{s}_1, \mathbf{s}_2\}\mathbf{P}^* = \mathbf{\Sigma}_{12}\mathbf{P}^* \tag{6}$$

Finally, the prediction of the unknown data $\mathbf{s}_1$ can be done using the projection $\mathbf{y}_2$:

$$\mathrm{E}\{\mathbf{s}_1|\mathbf{y}_2\} = \mu_1 + \mathbf{\Sigma}_{12}\mathbf{P}^*{\mathbf{\Lambda}^*}^{-1}{\mathbf{P}^*}^{\mathrm{T}}(\mathbf{s}_2 - \mu_2) \tag{7}$$

This expected value can be used for any unknown set of vertices $\mathbf{s}_1$ given a partial scan $\mathbf{s}_2$, be that a single missing vertex or all the missing data. If every unknown vertex is predicted according to the described method the known triangulation from the training set can be propagated to the predicted data set and will then constitute a full surface reconstruction. The method can also be used to filter data for noise if the known scan data are also recovered. By varying the number

k values of Eigenvectors used in the projection the fraction of described variance can be controlled.

Practically, the set of known vertices found during the registration of the partial scan is $\mathbf{s}_2$ and the full scan as provided by the scanner is $\mathbf{s}_{scan}$. Let $\mathbf{s}_1^*$ be the predicted missing data, $\mathbf{s}_2^*$ the prediction of the partial scan and $\mathbf{s}^*$ be the full reconstructed shape. The full average shape is denoted μ. With an initial registration the algorithm works as follows: We repeat the loop body with two

Algorithm 1. Anatomical surface recovery

procedure AnatomicalSurfaceRecovery($X_{aligned}, s_2, s_{scan}$) ▷
  $\mathbf{s}^* \leftarrow \begin{bmatrix} \mathbf{0} \\ \mathbf{s}_2 \end{bmatrix}$
  repeat
    Procrustes align $\mathbf{s}^*$ to μ and apply same transformation to $\mathbf{s}_{scan}$
    Predict $\mathbf{s}_1^*$ using the described method ▷ the described variance is increased in each iteration
    Predict $\mathbf{s}_2^*$ using the described method ▷ the described variance is increased in each iteration
    $\mathbf{s}^* \leftarrow \begin{bmatrix} \mathbf{s}_1^* \\ \mathbf{s}_2^* \end{bmatrix}$
    Find vertex correspondence between $\mathbf{s}^*$ and $\mathbf{s}_{scan}$
    Update $\mathbf{s}_2$ and $\mathbf{s}^*$ with the correspondence vertices from $\mathbf{s}_{scan}$
  until convergence
  return $\mathbf{s}_1^*$ and $\mathbf{s}_2^*$ ▷
end procedure

different recovery approaches. First $\mathbf{s}_1^*$ and $\mathbf{s}_2^*$ are predicted all at once. In the last few loops the data are predicted vertex by vertex using only the nearest vertices in the prediction. The vertex distances are found as the geodesic distances on the mean shape, so these only have to be calculated once. The geodesic distances are used to ensure topological consistency when selecting a neighbourhood. Our shape model has 3096 vertices and in the local recovery we only use the 10 nearest of these. In the local prediction the recovered data is locally very true to the original scan. We restrict the Eigenvalues in the recovery to the ones describing 30% of the variance and then gradually raise this to 99.9%. Gradually raising the percentage of described variance helps the algorithm produce anatomically correct shapes and prevents the influence of bad correspondences in the initial iterations.

4 Results

Based on the method described in section 2, we were able to construct an extensive Active Shape Model of the left ear based on the available dataset. A total of 310 samples were processed and from these, 241 passed the automatic quality verification. As the Active Shape Model processes new samples, the complexity

of the model increases and thus the fraction of variation explained per principal component must be expected to drop. The fraction of variation explained by the 10 first principal components were computed as the ASM grew in size and it was stabilising, indicating that the shape model eventually captures the true class variability. In the ASM 90% of all variance is contained within the first 37 modes of variation. We do, however, expect that the automatic registration procedure has induced an amount of false variation in form of vertex drifting along the sample surfaces. Such variation of course directly affects the compactness of the ASM in the form of low-variance principal components, assuming that the drifts are uncorrelated. The actual shape variation from the ear is therefore expected to be found within the first principal components. A final manual inspection of mesh distortions resulted in an additional 80 registrations being removed from the ASM. Effectively this resulted in the final ASM consisting of 161 shapes.

In order to compare our approach with existing methods for reconstruction, a collection of 10 scanned ear impressions, not included in the training data, was chosen and all scans had a reasonable sized hole cut in them. The holes were cut between first and second bend of the ear canal, in an area that is known to often be occluded when using experimental optical in-ear scanners. Hereby any reconstruction of these partial scans can be compared to the ground-truth, allowing for a quantitative comparison of methods.

For each mesh in the collection of *synthesised* partial scans the missing data was recovered. This was done using our method, both with and without smoothing, and the Markov Random Field (MRF) surface reconstruction approach [18]. The MRF approach has previously shown to reconstruct anatomical surfaces well. All reconstructions were then compared to the ground truth, by computing a signed distance (based on surface normals) between all reconstructed points and the original surface. In Fig. 2 the reconstructions of synthetic partial scans are shown, where the surface values denotes the signed distance between reconstruction and truth (in millimeters). The average signed point-distances between surface reconstructions can be seen in the table below:

#	MRF	Proposed	Proposed +local smoothing	#	MRF	Proposed	Proposed +local smoothing
1	-0.07	-0.17	-0.27	6	0.07	-0.05	-0.08
2	0.05	0.01	-0.01	7	0.08	-0.001	0
3	-0.04	0.02	0.001	8	0.01	-0.02	-0.03
4	-0.001	-0.015	-0.02	9	0.02	0.03	0.01
5	-0.07	-0.01	-0.013	10	-0.01	0.07	0.07

A significant outlier in the error is observed in sample #1. After inspection, this sample revealed an abnormal cavity in the skin of the ear-canal, explaining the higher error. It should be noted that no prior, neither statistical or physical, would be able to predict such errors. Although this comparison proves high performance of our method, it does not fully illustrate the strength of having a statistically based prior. The MRF approach predicts missing points based on the existing curvature of data in contrast to our method that predicts missing

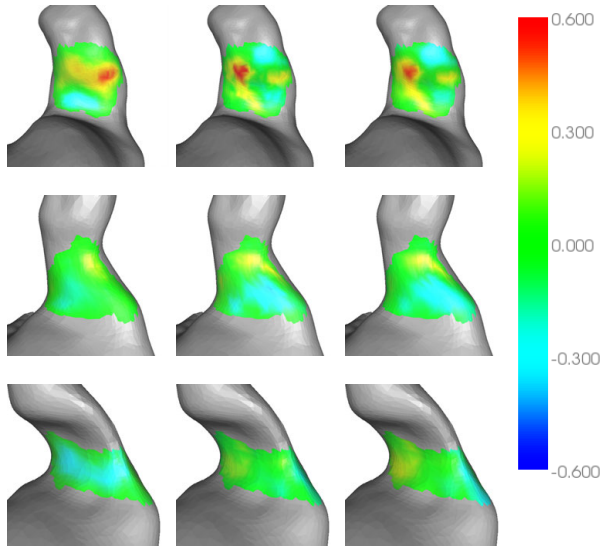

Fig. 2. Reconstruction of missing data for 3 different scans (rows), using Markov Random Field (MRF) reconstruction (column 1), our method (column 2) and the smoothed variant of our method (column 3). Surface values corresponds to the signed distance between reconstruction and ground truth.

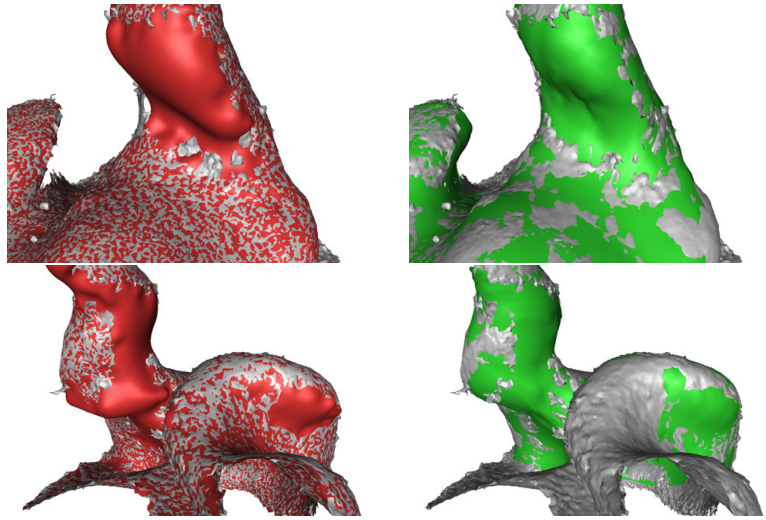

Fig. 3. Partial scans from a prototype direct ear scanner. Raw data is shown with grey. Surfaces reconstructed using the MRF method are red and the surfaces reconstructed using the proposed method are green.

points based on knowledge of the shape variation of an ear population. Effectively this means that where either noisy edges exists or data is sparse, the MRF approach has little chance of estimating the true surface. In this test each hole is surrounded by smooth noiseless surface areas providing an optimum setting for the MRF reconstruction. In the following, we will present a qualitative comparison based on authentic optical 3D scans of the ear, suffering from high noise and sparse point support.

We have tested our algorithm on 12 scans from a prototype direct in ear scanner [1]. In cases with a lot of noise, our strong prior enables our method to produce anatomically correct meshes that are also locally true to the covered areas. Qualitative inspection shows very good hole closing in the 12 scans. In addition all 12 scans were 3D printed as earplugs and tested by the respective test subjects with positive feedback. Fig 3 shows scans with a big part of the ear canal missing. The missing part has been recovered with both the MRF method and the proposed method. As can be seen, our proposed method produces what seems to be a much more plausible surface in the missing part.

5 Conclusion

We have shown that we can predict the missing parts of partial scans using a statistical model. The ability to predict missing data is comparable to state-of-the-art algorithms, when holes are relatively small and the data is fair without too much noise. On scans from a real in-ear scanner probe prototype, the qualitative results produced with the proposed method are much more plausible when visually inspected. The more extensive prior knowledge about the shape to be reconstructed makes the recovery much more robust, when recovering larger holes. The results also seem invariant to the presence of noise, and as such the method can also function as a noise filter. Surface reconstruction algorithms that only use the immediate vicinity in the reconstruction are very sensible to noise on the edges of the area to be recovered.

After using the proposed data recovery method on 12 scans they were 3D printed on a stereolithograpy (SLA) machine [2] and worn by the test subjects for a substantial time. They all proved to be well fitting in the subjects ears even though the hard material from the SLA machine makes the ear plugs very susceptible for non-accurate fitting. We have therefore demonstrated a complete pipeline from direct ear scanning to production of well fitting hearing devices.

Acknowledgments. This work was (in part) financed by the *Danish National Advanced Technology Foundation* (project no 019-2009-3). We thank Oticon A/S for supplying the scanned ear impression data.

References

1. 3Shape, Copenhagen. http://www.3Shape.com
2. Projet MP3000, 3Dsystems. http://www.3DSystems.com/

3. Belongie, S., Malik, J., Puzicha, J.: Shape matching and object recognition using shape contexts. IEEE Trans. on Pattern Analysis and Machine Intelligence **24**(4), 509–522 (2002)
4. Blanz, V., Mehl, A., Vetter, T., Seidel, H.P.: A statistical method for robust 3D surface reconstruction from sparse data. In: Proc. 3D Data Processing, Visualization and Transmission, pp. 293–300 (2004)
5. Blanz, V., Vetter, T.: A morphable model for the synthesis of 3D faces. In: Proc. 26th Annual Conference on Computer Graphics and Interactive Techniques, pp. 187–194 (1999)
6. Caselles, V., Haro, G., Sapiro, G., Verdera, J.: On geometric variational models for inpainting surface holes. Computer Vision and Image Understanding **111**(3), 351–373 (2008)
7. Clarenz, U., Diewald, U., Dziuk, G., Rumpf, M., Rusu, R.: A finite element method for surface restoration with smooth boundary conditions. Computer Aided Geometric Design **21**(5), 427–446 (2004)
8. Cootes, T., Taylor, C., Cooper, D., Graham, J.: Active shape models - their training and application. Computer Vision and Image Understanding **61**(1), 38–59 (1995)
9. Frome, A., Huber, D., Kolluri, R., Bülow, T., Malik, J.: Recognizing objects in range data using regional point descriptors. In: Pajdla, T., Matas, J.G. (eds.) ECCV 2004. LNCS, vol. 3023, pp. 224–237. Springer, Heidelberg (2004)
10. Hammond, P., Hutton, T., Allanson, J., Campbell, L., Hennekam, R., Holden, S., Patton, M., Shaw, A., Temple, I., Trotter, M., et al.: 3D analysis of facial morphology. American Journal of Medical Genetics Part A **126**(4), 339–348 (2004)
11. Kazhdan, M., Bolitho, M., Hoppe, H.: Poisson surface reconstruction. In: Proc. Eurographics Symposium on Geometry Processing, pp. 61–70 (2006)
12. Kolluri, R., Shewchuk, J., O'Brien, J.: Spectral surface reconstruction from noisy point clouds. In: Proc. Eurographics Symposium on Geometry Processing, pp. 11–21 (2004)
13. Kuhn, H.W.: The Hungarian method for the assignment problem. Naval Research Logistic Quarterly **2**, 83–97 (1955)
14. Lanche, S., et al.: A statistical model of head asymmetry in infants with deformational plagiocephaly. In: Ersbøll, B.K., Pedersen, K.S. (eds.) SCIA 2007. LNCS, vol. 4522, pp. 898–907. Springer, Heidelberg (2007)
15. Nelder, J.A., Mead, R.: A simplex method for function minimization. The Computer Journal **7**(4), 308–313 (1965)
16. Paulsen, R.R., Hilger, K.B.: Shape modelling using markov random field restoration of point correspondences. In: Taylor, C., Noble, J.A. (eds.) IPMI 2003. LNCS, vol. 2732, pp. 1–12. Springer, Heidelberg (2003)
17. Paulsen, R., Larsen, R., Nielsen, C., Laugesen, S., Ersbøll, B.: Building and testing a statistical shape model of the human ear canal. In: Dohi, T., Kikinis, R. (eds.) MICCAI 2002. LNCS, vol. 2489, pp. 373–380. Springer, Heidelberg (2002)
18. Paulsen, R., Bærentzen, J., Larsen, R.: Markov random field surface reconstruction. IEEE Trans. on Visualization and Computer Graphics **16**(4), 636–646 (2010)
19. Rusinkiewicz, S., Levoy, M.: Efficient variants of the icp algorithm. In: Proc. 3D Digital Imaging and Modeling, pp. 145–152 (2001)
20. Verdera, J., Caselles, V., Bertalmio, M., Sapiro, G.: Inpainting surface holes. In: Proc. of International Conference on Image Processing, vol. 2 (2003)

Appendix F

Contribution C.VI: Minimal BRDF Sampling for Two-Shot Near-Field Reflectance Acquisition

Minimal BRDF Sampling for Two-Shot Near-Field Reflectance Acquisition

Zexiang Xu[1] Jannik Boll Nielsen[2] Jiyang Yu[1] Henrik Wann Jensen[1] Ravi Ramamoorthi[1*]
[1]University of California, San Diego [2]Technical University of Denmark

Abstract

We develop a method to acquire the BRDF of a homogeneous flat sample from only two images, taken by a near-field perspective camera, and lit by a directional light source. Our method uses the MERL BRDF database to determine the optimal set of light-view pairs for data-driven reflectance acquisition. We develop a mathematical framework to estimate error from a given set of measurements, including the use of multiple measurements in an image simultaneously, as needed for acquisition from near-field setups. The novel error metric is essential in the near-field case, where we show that using the condition-number alone performs poorly. We demonstrate practical near-field acquisition of BRDFs from only one or two input images. Our framework generalizes to configurations like a fixed camera setup, where we also develop a simple extension to spatially-varying BRDFs by clustering the materials.

Keywords: rendering, reflectance, BRDF, MERL, reconstruction

Concepts: •**Computing methodologies** → **Reflectance modeling;**

1 Introduction

Accurate BRDF models are critical for realistic image synthesis. Many analytic BRDF models have been proposed [Torrance and Sparrow 1967; Ward 1992]. However, the greatest fidelity is obtained by data-driven reflectance, such as the MERL BRDF database of 100 real materials [Matusik et al. 2003a].

In this paper, we focus on the canonical problem of measuring the 3D isotropic BRDF of a flat sample of homogeneous material. The conventional approach is to use a gonioreflectometer, laboriously sampling illumination-view pairs [Foo 1997]. However, fully sampling a 3D isotropic BRDF domain can require thousands or millions of samples, making this approach very expensive. Mirror-based imaging setups [Ward 1992] can reduce some dimensions, but still require a large number of samples. They also need more complex setups, and can be difficult to calibrate.

Recently, [Nielsen et al. 2015] presented a significant reduction in the number of samples needed to about 20, assuming the BRDF lies approximately in the subspace of the MERL BRDF database. They leverage a logarithmic mapping (originally proposed for BRDF factorization by [McCool et al. 2001]). They then optimize sampling directions to minimze the condition number of the related acquisition matrix (an approach first proposed by [Matusik et al. 2003b]).

*email {zexiangxu, jiy173, henrik, ravir }@eng.ucsd.edu, jbol@dtu.dk
Permission to make digital or hard copies of all or part of this work for personal or classroom use is granted without fee provided that copies are not made or distributed for profit or commercial advantage and that copies bear this notice and the full citation on the first page. Copyrights for components of this work owned by others than the author(s) must be honored. Abstracting with credit is permitted. To copy otherwise, or republish, to post on servers or to redistribute to lists, requires prior specific permission and/or a fee. Request permissions from permissions@acm.org. © 2016 Copyright held by the owner/author(s). Publication rights licensed to ACM.
SA '16 Technical Papers,, December 05 - 08, 2016, , Macao
ISBN: 978-1-4503-4514-9/16/12
DOI: http://dx.doi.org/10.1145/2980179.2982396

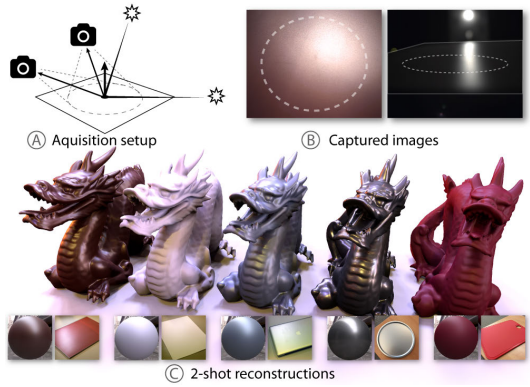

Figure 1: *By utilizing the field of view of a camera (A), many radiance observations can be acquired in parallel, to enable efficient BRDF measurement from a homogeneous flat material sample (we assume a near-field camera and distant light source). We demonstrate that as little as 2 view/light configurations enable accurate reconstruction for most materials. The two input images are shown in (B); our acquisition uses data from the circular center of the sample outlined, which may appear elliptical at oblique angles. Qualitatively, the first image captures the overall shape and intensity of the specular highlight and diffuse color. The second image captures grazing angles and Fresnel effects, also refining diffuse shading. From these inputs, we reconstruct a full measured BRDF, which can be visualized on a sphere or used for rendering (C); input material samples are shown in the insets and in results in Fig. 11.*

However, there are several limitations of [Nielsen et al. 2015]. First, they use a gantry-based system, where each "measurement" is actually a full 2D image seen by the camera. However, this additional information is not used in their work, providing only a single observation. We seek to exploit the additional degrees of freedom by acquiring multiple BRDF measurements simultaneously, using a near-field camera, so each point on the sample corresponds to a slightly different viewing direction. In this paper, we demonstrate an improved minimal BRDF sampling method for near-field acquisition. Indeed, accuracy comparable to the 20 measurements in [Nielsen et al. 2015] is achievable with only two near-field images, and high-fidelity results are sometimes achieved with a single image, with field-of-view only about 25°, as shown in Figs. 1, 2.

A major technical challenge is finding the optimal light-view directions. The conventional condition number metric is not adequate, since it can increase dramatically (or even go to infinity) for a set of closely-related near-field measurements. While the measurements are no longer completely independent, they do provide additional information. Even for the goniometric case in [Nielsen et al. 2015], we show that condition number does not fully model the error.

We therefore develop an entirely new framework to accurately estimate the error in BRDF acquisition from a set of samples, considering both deviation from the ideal (noise, BRDF not fitting MERL data), and accuracy of reconstruction based on where samples are located (Fig. 3). The condition number only approximates error from the first term (noise), while we usually want to minimize the latter term (reconstruction error). Our framework enables sig-

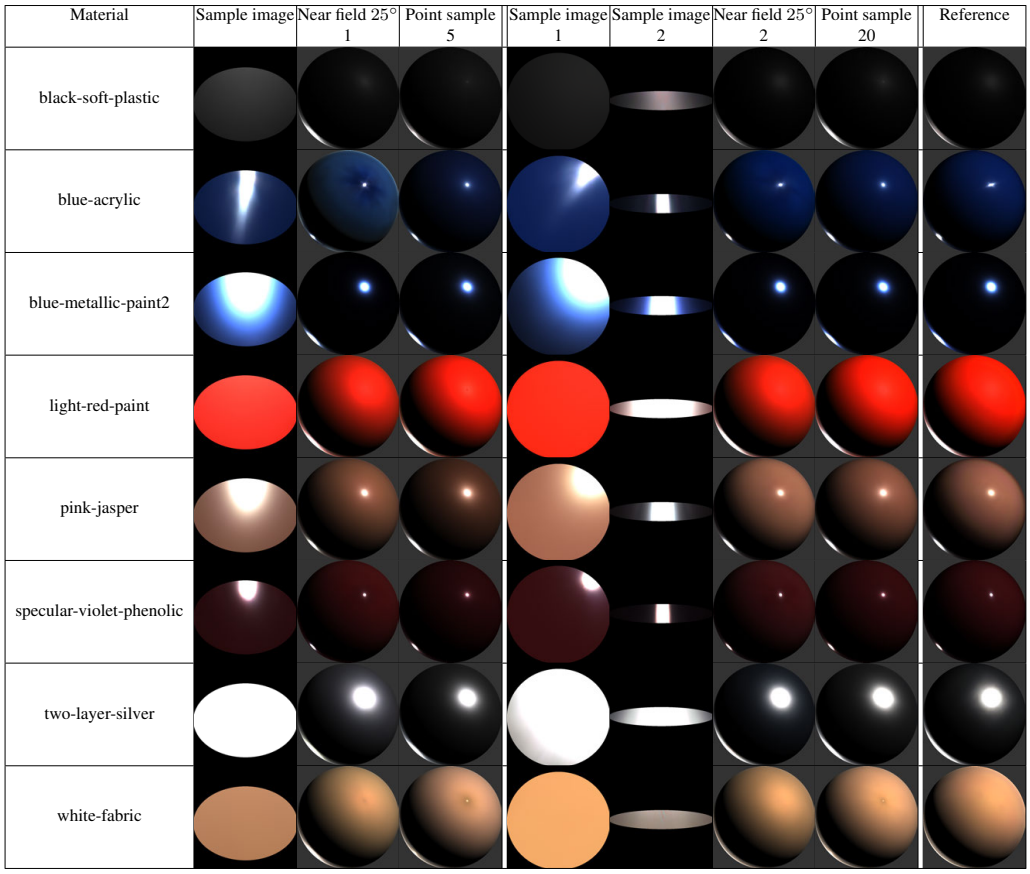

Figure 2: *Simulations on MERL BRDF database for one and two-shot near-field BRDF measurement. BRDFs shown are not used at all in analysis/choosing the optimal directions. The sample subtends an angle of* 25° *when camera is at the zenith (we consider a circular region, sample images elliptical when viewed at an oblique angle; see Figs. 4, 9). After sample label, first 3 columns show single image near-field acquisition, with input, our method and previous work with 5 point samples. The next 4 columns show two image acquisition with inputs, our method, and previous work with 20 point samples. The reference image is shown rightmost. Single-shot measurement is comparable to 5 samples in [Nielsen et al. 2015]. Near-reference quality images, comparable to 20 samples in [Nielsen et al. 2015], are obtained with two-shot meaurement. For very broad specularities like light red paint, we do not fully observe the highlights in the input images, and therefore slightly underestimate their width. The supplementary material has results for simulations on all of the MERL BRDF materials.*

nificantly better reconstruction error for the multiple-measurement near-field setup (Fig. 5). We make the following contributions:

Novel Theoretical Analysis: We develop a new framework to predict the error in BRDF acquisition from sampling a particular set of directions (Sec. 4), that extends naturally to multiple measurements and allows for optimization (Sec. 5).

Optimal BRDF Sampling Directions: We provide optimal light-view directions for the near-field case (Sec. 6), showing how multiple simultaneous BRDF measurements can dramatically reduce the number of images (see Fig. 2 for simulations on MERL database). The new error framework also provides improved accuracy even for point-sampled measurement (Appendix B).

Practical BRDF Acquisition: We develop BRDF measurement using only two near-field images (two-shot), and we demonstrate results on several real examples (Sec. 7). We also briefly explore extensions to a fixed camera setup with two light directions (Sec. 8), including a simple first step towards acquiring spatially-varying BRDFs by clustering materials.

2 Related Work

We focus on measured data-driven BRDFs. A few recent works have evaluated and developed improved parametric fits to the MERL BRDF database [Ngan et al. 2005; Low et al. 2012; Brady et al. 2014]. Earlier, Lensch et al. [2003] proposed adaptive sampling of a BRDF, based on the uncertainty of the parametric fit. Fuchs et al. [2007] also proposed an adaptive sampling approach, but first require a relatively dense grid of samples. Our approach actually requires less data (only one or two images), is more accurate, and requires only linear solution, rather than non-linear optimization. Our method is also conceptually related to other areas, such as the use of key points for animation [Meyer and Anderson 2007].

We briefly review related work in efficient BRDF acquisition below.

Basis and Environment Lighting: One approach to speed up BRDF acquisition is to use basis functions for complex illumination [Ghosh et al. 2007; Aittala et al. 2013; Tunwattanapong et al. 2013]. Our setup is simpler and requires fewer measurements, enabling direct BRDF measurement from a directional source, without any deconvolution. Other work has dealt with (uncontrolled) environment lighting [Romeiro et al. 2008; Romeiro and Zickler 2010], but requires non-linear regularization and priors.

Image-Based BRDF Acquisition: The MERL database was acquired by Matusik et al. using image-based BRDF measurement [Marschner et al. 2000] on spheres. Our approach is conceptually similar, making use of images rather than point measurements, but works with conventional flat surfaces (not all BRDFs are easily found as, or can be wrapped on, spheres). Earlier, Karner et al. [1996] fit anisotropic BRDFs to images of a flat sample, but required a parametric model. A variety of other optical setups acquire multiple samples simultaneously, including [Ward 1992; Dana and Wang 2004; Noll et al. 2013]. These methods usually require complex imaging setups, which are hard to calibrate.

One and Two Shot Approaches: Most recently, Aittala et al. [2015] proposed a two-shot spatially-varying BRDF capture setup, but it is aimed at reproducing the "texture" of material samples, rather than a complex measured BRDF. Earlier, [Hertzmann and Seitz 2003] used reference BRDFs to recover shape and spatially-varying reflectance. Ren et al. [2011] developed a pocket reflectometry method, comparing to reference tiles, using a handheld light source and fixed camera. In contrast, we do not require a physical reference since we can leverage the MERL database, which also has a much broader set of reference materials.

Industry Material Standards: Beyond computer graphics, the materials industry has developed a number of standards for measuring and characterizing reflectance. [Hunter and Judd 1939] proposes a single measurement at 60° perfect reflection. The ASTM Standard D523 for measuring gloss adds near-normal and grazing angle measurements at 85° and 20° [Hunter 1987]. We extend this approach by considering near-field measurements. Our optimal sets of one and two measurements produce results that are close to the above observations, but are based on rigorously minimizing the expected error. Moreover, we can recover a full accurate data-driven BRDF, since we consider multiple measurements over the entire sample. Additional works in graphics include the five measurement directions in [Westlund and Meyer 2001], which are improved on by [Nielsen et al. 2015] and further refined by our method.

3 Background

In this section, we briefly discuss necessary background on using the MERL database [Matusik et al. 2003a] for BRDF measurement, following [Nielsen et al. 2015]. We conclude by providing intuition for why the condition number metric is not ideal, especially in the near-field lighting case, a result that may also impact other problems involving sparse sampling and reconstruction in graphics.

BRDF Database and Processing: The database consists of 100 materials. Each material is represented using $p = 1,458,000$ exhaustive measurements of the 3D isotropic BRDF volume in the $(\theta_h, \theta_d, \phi_d)$ parameterization [Rusinkiewicz 1998] (Fig. 4), with resolution $90 \times 90 \times 180$ degrees. Following [Nielsen et al. 2015], we treat each color channel separately, effectively obtaining $m = 300$ database BRDFs. We also apply their log-relative mapping (inspired by the logarithmic transform proposed in [McCool et al. 2001]). BRDF ρ is transformed to $\ln\left[(\rho w + \epsilon)/(\rho_{\text{ref}} w + \epsilon)\right]$, where $\epsilon = 0.001$ avoids division by zero, ρ_{ref} is the reference or (per-observation) median BRDF, and the weight w is simply the maximum of the cosine of incident and outgoing angles. In this paper, we deal only with these log-mapped BRDFs. Inverse mapping is done at the end to obtain the final measured BRDF.

BRDF Principal Components: Let $X \in \mathbb{R}^{m \times p}$ be the full matrix of all MERL BRDF observations, where the rows are mapped BRDFs and the columns are a particular direction. We use the principal components Q, obtained by performing a singular-valued decomposition (SVD) after subtracting the mean BRDF,

$$X - \hat{\mu} = U \Sigma V^T \qquad Q = V\Sigma, \tag{1}$$

where it is convenient to include the singular values in $Q \in \mathbb{R}^{p \times k}$. k is the number of principal components we consider (in our case, $k = m$, but one could use fewer components). The columns of Q are the scaled eigenvectors of the covariance, and correspond to a basis for the space of BRDFs. A particular BRDF x may be obtained as a linear combination of the basis,

$$x = Qc + \mu, \tag{2}$$

where $c \in \mathbb{R}^{k \times 1}$ is a vector of coefficients. $\mu \in \mathbb{R}^{p \times 1}$ is the mean BRDF, while $\hat{\mu} \in \mathbb{R}^{m \times p}$ is a matrix, repeating μ^T over m rows.

Solving for the Measured BRDF: In practice, we observe x at some sample observations, from which we seek to estimate c,

$$\tilde{x} - \tilde{\mu} = \tilde{Q}c, \tag{3}$$

where the tildes indicate that we have a reduced set of observations at n samples, with $\tilde{\mu}$ and $\tilde{x} \in \mathbb{R}^{n \times 1}$. $\tilde{Q} \in \mathbb{R}^{n \times k}$ is the set of rows in Q corresponding to the set of reduced observations. It is also convenient to define $y = x - \mu$, with $\tilde{y} = \tilde{x} - \tilde{\mu}$ and $\tilde{Q}c = \tilde{y}$. Finally, let $S \in \mathbb{R}^{n \times p}$ be a selection matrix that is zero everywhere, except that $S_{ij} = 1$ in row i iff j is the direction corresponding to observation i. We can now define the reduced $\tilde{Q} = SQ$ and $\tilde{y} = Sy$, which will be useful for the error analysis in Sec. 4.

In [Nielsen et al. 2015], $n \ll p, m$, and typically $n \sim 20$. In our case, for near-field imaging, we have fewer image captures (typically only one or two), but we have several observations at each image, since we make use of the full 2D image. n can now be larger and, in some cases, could even be greater than m. However, the near-field samples are correlated, having the same light and similar view directions, so conceptually we still have a reduced matrix.

The above equation can be solved for the coefficients using Tikhonov regularization (I is the identity matrix. We set $\eta = 40$; we find results are not sensitive to this regularization parameter),

$$c = \text{argmin}| \left(\tilde{x} - \tilde{\mu}\right) - \tilde{Q}c|^2 + \eta|c|^2 = \left(\tilde{Q}^T\tilde{Q} + \eta I\right)^{-1} \tilde{Q}^T\tilde{y}. \tag{4}$$

A useful intuition is to consider a closed-form expression for the regularized inverse. Assuming the full SVD of $\tilde{Q} = A\Lambda B^T$,

$$\tilde{Q}^+_\eta = \left(\tilde{Q}^T\tilde{Q} + \eta I\right)^{-1} \tilde{Q}^T = B\Lambda^+_\eta A^T, \tag{5}$$

where Λ^+_η is a diagonal matrix with the same shape as Λ, but with a modified set of singular values: $\sigma \to \sigma/(\sigma^2 + \eta)$. Note that the pseudo-inverse $\tilde{Q}^+$ and Λ^+ are obtained by setting $\eta = 0$, in which case $\tilde{Q}^+ = B\Lambda^+A^T$ as expected. In essence, the regularization term creates a $\eta-$modified pseudo-inverse where the inversion of small singular values does not blow up.

Optimizing Sampling Directions: In [Matusik et al. 2003b; Nielsen et al. 2015], the optimal sampling directions (the rows of $\tilde{Q}$

chosen, or equivalently the selection matrix S with $\tilde{Q} = SQ$) are found by optimizing (minimizing) the condition number,

$$\kappa(\tilde{Q}) = \frac{\sigma_{max}(\tilde{Q})}{\sigma_{min}(\tilde{Q})}, \tag{6}$$

where $\sigma_{\max}$ and $\sigma_{\min}$ are the maximum and minimum singular values of $\tilde{Q}$. The condition number is a standard numerical tool, and reducing it minimizes the sensitivity to noise and related errors.

Formally, consider a matrix equation such as equation 3, with $\tilde{Q}c = \tilde{y}$ (with $\tilde{y} = \tilde{x} - \tilde{\mu}$ as usual). The condition number is the worst case (upper bound) estimate of the ratio of fractional error δc in output to fractional error/noise $\delta\tilde{y}$ in input,

$$\frac{|\delta c|/|c|}{|\delta\tilde{y}|/|\tilde{y}|} \leq \kappa(\tilde{Q}). \tag{7}$$

3.1 Limitations of Using the Condition Number

The condition number gives good results for point-sampled BRDF measurement [Matusik et al. 2003b; Nielsen et al. 2015]. It can be considered a measure of correlation between samples, and minimizing it chooses sampling directions that discriminate between distinct BRDFs. However, we found that it did not easily extend to near-field measurements, where a large number of related observations are made (Fig. 5). The observation matrix $\tilde{Q}$ is now often rank deficient or nearly so, and close-by observations can drive the condition number very large or even to infinity, reducing its ability to discriminate and choose optimal directions. This leads to the paradox where fewer observations are preferred. In the next section, we formally derive the expected error, considering both reconstruction error and noise. For near-field BRDF measurement, we achieve a dramatic improvement; one to two near-field images is adequate.

There are also many technical limitations of condition number. First, there are two terms related to error: noise or other imperfections (deviations from MERL data); and reconstruction error caused by having too few samples (even in the presence of zero noise or deviation). $\kappa(\tilde{Q})$ only bounds the first term (noise/deviations), but the major component of the error is actually reconstruction error from having fewer observations than principal components. Second, condition number considers fractional error, assuming the error is proportional to the signal. However, the accuracy of measurements from real cameras is determined by a number of factors (shot noise, read noise, dark current), which are constant or proportional to the square root of intensity, and not the intensity itself. Indeed, well lit pixels have less relative noise, and in this paper we more accurately model the noise as a constant magnitude, independent of the signal. Third, κ only provides a worst-case bound, while we are often interested in the average error, say over all of the materials in the MERL BRDF database. Hence, our optimal sampling directions improve somewhat on [Nielsen et al. 2015] even for point-sampling.

4 Sampling Error Analysis

In this section, we conduct a novel analysis of the BRDF reconstruction error from a sparse set of samples. This error can be minimized to find the optimal set of sampling directions, for both conventional point-wise BRDF acquisition, and near-field image-based measurement. For completeness, we consider three sources of error: deviation from the MERL database, sparse sampling, and noise in measurement. In practice, deviation error from the MERL database is not easy to predict, nor is the real noise level easy to evaluate. Therefore, our practical algorithm will focus on minimizing the reconstruction error from sparse sampling, which is the main factor in choosing suitable directions for BRDF acquisition.

Deviation from BRDF Model: We assume the BRDF being measured lies in the subspace spanned by the MERL database (and encapsulated in Q). If this is not the case, we can only find the best projection of the MERL BRDF data. This error is present even when we have all observations. Using pseudo-inverse Q^+ of Q,

$$c = Q^+(x - \mu) = Q^+ y = \Sigma^{-1} V^T y, \tag{8}$$

where we expand $Q = V\Sigma$. The resulting deviation error is,

$$\boxed{E_{\text{deviation}} = |Qc - y| = |(VV^T - I)y|.} \tag{9}$$

Note that $V \in \mathbb{R}^{p\times k}$ is an orthogonal matrix with $V^TV = I$, but since $k < p$, $VV^T \in \mathbb{R}^{p\times p}$ is not the identity. However, if y is in the MERL BRDF database, it is given as a column of $Y^T = (X - \hat{\mu})^T = V\Sigma U^T$. Using the SVD decomposition, it is easy to see that $(VV^T - I)V\Sigma U^T = 0$, since $V^TV = I$.

Therefore, $E_{\text{deviation}} = 0$ if the material is in the subspace Q spanned by the MERL database, but will be nonzero if it lies outside this subspace. This is an intrinsic property of the material, and *independent of the sampling directions chosen.*

Projection to Sampling Directions: Choosing a sparse set of n sampling directions corresponds mathematically to choosing a particular selection matrix $S \in \mathbb{R}^{n\times p}$. Noting that $\tilde{Q} = SQ$ and $\tilde{y} = Sy$ by definition, so that $SQc = Sy$, we have

$$\bar{c} = (SQ)^+_\eta (Sy), \tag{10}$$

where in the last line we consider the regularized inverse of SQ, as per equation 5, and Sy are the observations we actually make with a camera or a gonioreflectometer. We use the bar on top of c to denote the recovered coefficients, with error

$$c - \bar{c} = \left(Q^+ - (SQ)^+_\eta S\right) y. \tag{11}$$

Finally, the reconstruction error is given by

$$\boxed{E_{\text{recon}} = \left|Q\left(Q^+ - (SQ)^+_\eta S\right) y\right|.} \tag{12}$$

This is the critical error we need to minimize, by choosing sampling directions (and hence S) optimally. It provides the error in reconstruction by measuring only a sparse set of samples, and applies equally whether those are point samples or multiple simultaneous image-based measurements. Note that this error exists even for noise-free measurements, coming purely from reconstruction error when using a sparse set of samples. (By using log-mapped BRDFs, we also limit the ability of intense specularities to unduly influence reconstruction error.) The condition number does not consider this term directly, but only sensitivity to noise. Nevertheless, we show in appendix A that minimizing condition number does adjust SQ to reduce (but not minimize) E_{recon}.

Figure 3 shows both deviation and reconstruction errors for the BRDFs in Fig. 2 (using a different set of 90 MERL materials as our data/training set). As expected, reconstruction error E_{recon} dominates in all cases. Blue acrylic has high $E_{\text{deviation}}$ since the star-shaped highlight deviates significantly from the database.

Noise Error: If we do have noisy data, the image observations y will be corrupted, and we will measure $\bar{y} = y + \triangle$, where $\triangle$ is the noise or error at each pixel. The resulting error in the coefficients is given from equation 10 by $(SQ)^+_\eta(S\triangle)$. Therefore,

$$\boxed{E_{\text{noise}} = \left|Q\,(SQ)^+_\eta\, S\triangle\right|.} \tag{13}$$

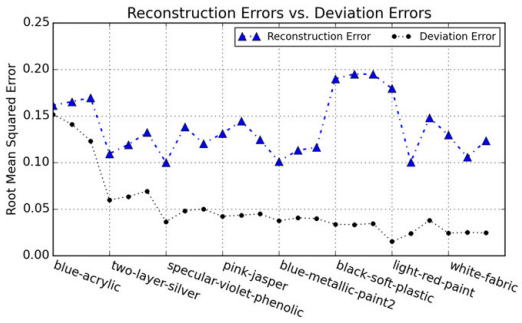

Figure 3: *Comparison of E_{recon} and $E_{\text{deviation}}$ for all materials in Fig. 2. Reconstruction error E_{recon} is dominant for most BRDFs.*

Conceptually, the condition number seeks to minimize this term. However, condition number provides only a worst-case bound, assuming the noise is proportional to the signal, which is not a correct assumption for cameras, where noise levels are relatively independent of image intensity. Moreover, our main focus is on reconstruction error from sampling (equation 12) rather than noise; one typically acquires high-dynamic range images from high-end cameras where noise is not the most significant challenge. Note that the condition number analysis also does not consider the full process, including the η-regularization. Finally, our focus is on near-field capture where we have several, but closely-related observations. This can lead to a very large condition number, while in fact the additional observations help in reducing the error.

The total error is written simply as (the less than sign comes from the triangle equality, since each error term considers the norm),

$$E_{\text{total}} \leq E_{\text{deviation}} + E_{\text{recon}} + E_{\text{noise}}. \tag{14}$$

Final Error Metric: For simplicity, we do not explicitly consider the deviation error, but just include it as part of the noise/error $\triangle$. A final issue is choosing y in equation 12 and $\triangle$ in equation 13, since these quantities depend on the measurements, camera noise, and are not known a-priori. For y, we minimize over all of the m materials in the MERL BRDF, essentially finding the sampling directions that best reconstruct the MERL materials. Define $y_i = x_i - \mu$ where $x_i \in \mathbb{R}^{p\times 1}$ is a vector corresponding to observations of BRDF i in the MERL database. For the noise, we assume a constant user-defined parameter β, corresponding to the noise/error level, $\beta = |\triangle|$, and use a noise vector $O \in \mathbb{R}^{p\times 1}$, where each element is simply 1. This can be seen as the expected magnitude of gaussian-distributed noise, where β controls the magnitude. Putting this together, our final expected error is,

$$E(S) = \left(\frac{1}{m}\sum_{i=1}^{m}\left|Q\left(Q^{+} - (SQ)_{\eta}^{+}S\right)y_i\right|\right) + \beta\left|Q\,(SQ)_{\eta}^{+}SO\right|. \tag{15}$$

Note that we add errors from reconstruction and noise. Each term on the right-hand side is a $p \times 1$ vector, and we take its norm. We also make explicit the dependence of E on selection matrix S.

In this paper, we focus mainly on minimizing the reconstruction error E_{recon} by choosing sampling directions. Therefore, we typically take $\beta = 0$, but we also demonstrate nonzero noise β in supplementary material. Finally, we emphasize that we have so far only defined error; the next section discusses how to choose the sampling directions, corresponding to the selection matrix S, to minimize this expected error. In essence, we seek $S = \text{argmin}\ E(S)$.

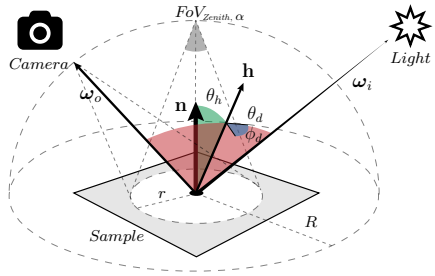

Figure 4: *Schematic of near-field reflectance acquisition. The half-diff angles $\theta_h, \theta_d, \phi_d$ are with respect to the center of the sample.*

5 Optimal Sampling Directions

We first describe selection of the optimal sampling directions for measuring individual light-view pairs in a BRDF, as in [Nielsen et al. 2015]. We refer to this as point sampling, to distinguish from the near-field image-based BRDF measurement of our method.

5.1 Point-Sampled BRDF Directions

We consider the whole space of valid directions $\mathcal{D} = \{\theta_h, \theta_d, \phi_d\}$ in the MERL database. Our goal is to find the optimal subset $\mathcal{D}^n$ with n directions, and form the corresponding n-row selection matrix S^n. For point samples, each row in S^n is simply one direction in $\mathcal{D}^n$. In other words, $S^n_{ij} = 1$ iff $\mathcal{D}^n_i = j$. The optimal $\mathcal{D}_n$ (and S_n) must be chosen to achieve the minimal error in equation 15.

We solve the optimization based on a numerical gradient descent framework analogous to [Nielsen et al. 2015], which is shown in that work to be more efficient and higher-quality than the greedy method of [Matusik et al. 2003b]. (Standard numerical optimizers do not work well, given the discrete BRDF space $\mathcal{D}$ and integer steps needed, as well as invalid BRDF regions.) However, we replace the condition number with the accurate error in equation 15, and extend the optimization framework to near-field measurements in Sec. 5.2. We start with an empty set $\mathcal{D}^0$ with no directions in it. Then we iteratively extend $\mathcal{D}^n$ to $\mathcal{D}^{n+1}$ as follows:

1. Randomly pick t candidate directions from $\mathcal{D} - \mathcal{D}^n$ (Typically we use t = 500.). For each candidate direction d, we form a selection matrix S_d of $\mathcal{D}^n \cup d$, and evaluate the expected error $E(S_d)$ from equation 15. An initial $\mathcal{D}^{n+1}$ and S^{n+1} is created with that $\mathcal{D}^n \cup d$ which has a minimal $E(S_d)$.

2. Randomly choose one of the $n+1$ directions in $\mathcal{D}^{n+1}$, which we denote as $(\theta_h, \theta_d, \phi_d)$. Numerically estimate the gradient of the error metric $\bigtriangledown E(S^{n+1}) = (\frac{\delta E(S^{n+1})}{\delta\theta_h}, \frac{\delta E(S^{n+1})}{\delta\theta_d}, \frac{\delta E(S^{n+1})}{\delta\phi_d})$. Move the chosen direction along $\bigtriangledown E$ with one step-length (initial step-length is 3 cells) if the destination is a valid location in $\mathcal{D}$. Repeat until convergence (finding a new direction each time).

3. Reduce step-length and repeat step 2 until convergence with step of 1 cell. Then the final $\mathcal{D}^{n+1}$ and S^{n+1} are formed.

5.2 Near-Field BRDF Directions

We now take advantage of sampling directions for all pixels in an image, instead of only the center of the image for point sampling. In general, the optimal directions depend on the camera's projection matrix and the size of the planar sample. To develop a general framework, we assume the image of interest is a circle on the plane

with radius r. We assume the camera moves on a hemisphere a distance R from the center of the circle, and is always pointed towards the center (i.e., the center pixel corresponds to the center of the sample). We also assume the image always sees the full sample (circle of interest). The key variable is the ratio $\nu = r/R$, which determines the linear field of view when the camera is at the zenith. The angular field of view $\alpha = 2\tan^{-1}\nu$, which is the angle we use to denote our near-field setup. A schematic of the setup is shown in Figs. 1 and 4. Note that the optimization framework is general, and can also apply to many other configurations. We discuss one-camera multiple light and one-light multiple view cases in Sec. 8.

The goal is still to find an optimal subset of camera directions $\mathcal{D}^n$. In this case, each direction represents the direction to the camera with respect to the center pixel. However, the corresponding selection matrix is no longer a n-row matrix. We replace S^n with $\bar{S}^n$ in near field acquisition. One direction in $\mathcal{D}^n$ forms a set of rows in $\bar{S}^n$, each of which corresponds to one pixel sample in an image. In general, there will be many more rows than for point-sampling, but many of the directions will be very closely related. Our error metric addresses this directly, and equation 15 still accurately predicts reconstruction error. We can now directly use $\bar{S}^n$ instead of S^n, and iteratively add directions from $\mathcal{D}^0$ to $\mathcal{D}^n$ as before. To validate the convergence of our method, we repeated the optimization 50 times with different random conditions, and fields of view. The results all converge well. The supplementary material shows convergence results for $n = 2$ near-field sampling with 25° field of view.

6 Evaluation with Simulations for Near-Field

We now evaluate the minimization of our error metric for near-field image-based BRDF measurement, using simulations with the MERL BRDF database. As shown in Fig. 5, our new error metric has significant advantages over using the condition number for the near-field case. (Visual results on rendered spheres are consistent with these numerical errors; results from minimizing condition number are often even worse than point-sampled measurements, far off from ground truth). Moreover, as seen in Fig. 6, our new image-based method is much more efficient than point-sampling; both methods capture similar images of a flat sample, but we make use of the full 2D image. Section 8 applies the framework to other configurations like fixed camera with multiple lights, or vice versa.

The setup is shown in Fig. 4. For simplicity, we assume a distant light source, and a near-field camera. In a single image, we capture a 2D slice of the BRDF (we consider a circular patch). Since we are assuming a flat sample with distant lighting, the illumination direction is the same everywhere, but the viewing direction varies at each pixel, enabling us to capture multiple observations simultaneously. It is clearly better to have a wider field of view to capture greater view variation, but this may require large samples and close cameras. In fact, we show that a relatively narrow field of view of about 25° suffices for two-shot BRDF acquisition.

We minimize equation 15, choosing the optimal light-view directions, as explained in Sec. 5.2. To evaluate the reconstruction error on the MERL BRDF, we use a slightly different set of directions using 90 training BRDF samples, testing on the 10 other materials not used at all in computing optimal directions. (We use the same training/test materials as [Nielsen et al. 2015] to enable direct comparisons to their approach.)

Figure 5 compares our average normalized reconstruction RMS errors for the unknown materials for several fields of view, as a function of the number of images, and to optimizing condition number alone. As shown in appendix B, condition number is actually a reasonable heuristic for point-sampled BRDF measurement [Nielsen et al. 2015], although our error metric performs somewhat better

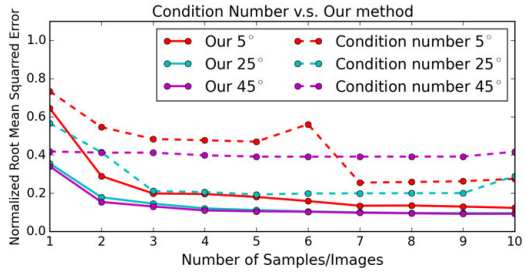

Figure 5: *Comparison of errors on unknown samples from our method, and from minimizing condition number, for near-field reflectance acquisition with different fields of view. It is clear that we produce better results for near-field reflectance acquisition.*

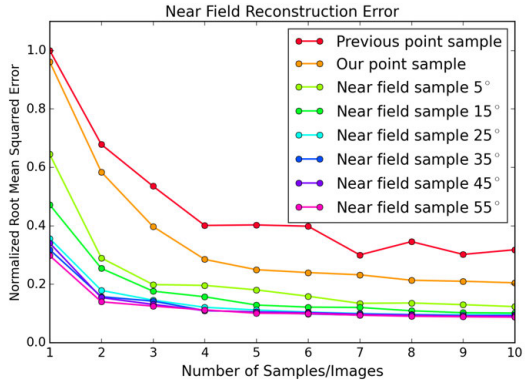

Figure 6: *Average RMS error over unknown samples for near-field reflectance acquisition. We plot the results for a number of different field of view angles. These results clearly show the benefits of our method, often requiring an order of magnitude fewer samples than point-sampled BRDF measurement.*

even in that case. However, it breaks down for near-field acquisition as seen in Fig. 5. With several correlated view directions, condition number becomes very large, losing the ability to discriminate between different sets of light-view directions. In some cases, it oscillates or does not decrease with increasing samples, while our method always performs well. *The new error metric is essential for determining optimal light-view directions in the near-field case.*

In Fig. 6, we compare RMS errors for several fields of view, and to point-sampled BRDF measurement (the top red curve is from [Nielsen et al. 2015] while the improved orange curve is using our error metric for the point-sampled case). We see that near-field reflectance acquisition requires almost an order of magnitude fewer images than point-sampled BRDF measurement. Also note that near-field acquisition converges quickly with increasing field of view; while larger fields of view help, 25° is already nearly best (supplementary shows similar curves even for extreme 85° and 175° fields of view). In fact, errors are comparable to standard spherical image-based BRDF measurement [Marschner et al. 2000] (with optimal directions chosen by our error metric; see Fig. 19 in appendix B). However, our approach applies more generally, to flat samples that cannot be obtained or wrapped on a sphere.

Figure 7 shows how errors decrease as more training materials are added to the database (in random order), showing a steady decrease

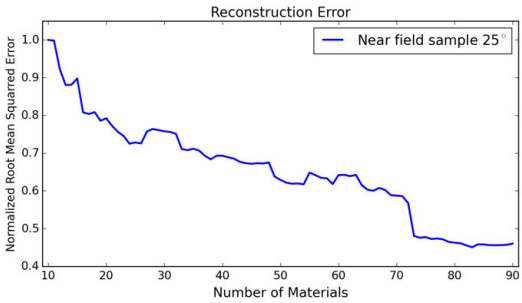

Figure 7: *Average RMS error versus number of materials in database for 2 shot near-field sampling with 25° field of view.*

n	$\theta_h[^\circ]$	$\theta_d[^\circ]$	$\phi_d[^\circ]$
1	3	42	1
2	0	60	0
	34	36	32

(a) 15°

n	$\theta_h[^\circ]$	$\theta_d[^\circ]$	$\phi_d[^\circ]$
1	3	50	9
2	6	23	41
	16	79	87

(b) 25°

n	$\theta_h[^\circ]$	$\theta_d[^\circ]$	$\phi_d[^\circ]$
1	3	52	0
2	4	40	0
	8	81	82

(c) 35°

n	$\theta_h[^\circ]$	$\theta_d[^\circ]$	$\phi_d[^\circ]$
1	3	60	4
2	0	81	0
	5	40	4

(d) 45°

Figure 8: *Tabulation of one and two near-field acquisition directions for fields of view ranging from 15° to 45°. Note that directions correspond closely to mirror reflection, imaging the highlight shape, and more grazing angles for Fresnel and other effects.*

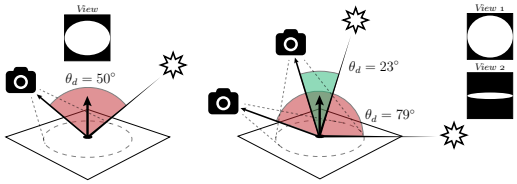

Figure 9: *Illustration of one- and two-shot camera/light configurations for a linear field of view of 25°.*

with more example BRDFs. Note that the MERL subspace depends on the specific BRDFs used, and the error curve can therefore increase slightly with the addition of a new material.

Note that with two-shot imaging, we can obtain essentially the same accuracy as 20 samples for point-sampled BRDF measurement, and even single-shot near-field acquisition achieves similar accuracy as about 5 samples for point-sampled BRDF measurement. These comparisons, simulated on the MERL data, are shown in Fig. 2. (We omit green fabric and silver metallic paint, whose results are very similar to black soft plastic and two layer silver respectively). We see that two-shot acquisition is adequate in nearly all cases. In some examples like pink jasper, specular violet-phenolic and white fabric, a single near-field image is comparable to 20 point-sampled images. In a few cases, like blue acrylic, two near-field images are required to achieve reasonable results; severe ringing is present in reconstruction from a single image. For very broad specularities like light red paint, we do not observe the full extent of the highlight in any single image, and slightly underestimate highlight width.

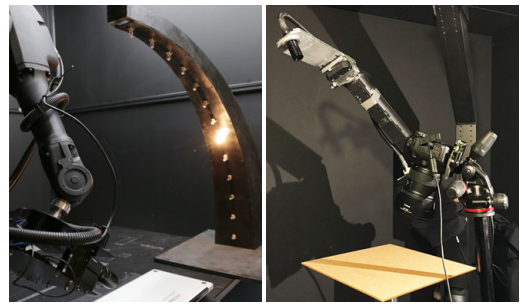

(a) *Setup A* **(b)** *Setup B*

Figure 10: *Photograph of our acquisition setup A and B. In setup A, a 6-axis industrial robot precisely positions the camera, and an illumination-arc positioned at $\phi = 0°$ illuminates the sample with halogen lights in $7.5°$ θ_d intervals. In setup B, a high-angular-resolution spherical gantry positions the light. A DSLR camera is positioned by utilizing the two arms of the gantry and a mirror.*

Finally, in Fig. 8, we tabulate our optimal 1,2 directions for near-field angles of 15°, 25°, 35° and 45°. Note that these directions are with respect to the center of the sample; the local view direction will vary at each pixel. For one image, we capture a slightly off-specular direction ($\theta_h = 3°$) at an angle of incidence of about 50°. Similarly, for two images, the first direction for 15° field of view is an exact specular reflection at 60°, although this varies somewhat with field of view. This is as expected, imaging the details of the specular highlight, around the center of the sample, and also accords well with measurements previously used in the appearance industry [Hunter and Judd 1939]. For most materials, this measurement also captures the overall diffuse color. The second direction usually varies somewhat from the specular (more for small fields of view, less for larger fields of view where diffuse and specular reflection are often both available in the same image). Intuitively, the second direction measures Fresnel effects at grazing angles (large θ_d for fields of view 25° and higher). It can also help refine the diffuse shading, especially for materials with broad specular lobes that cover all of the first image. Figure 9 illustrates the one- and two-shot light-view pairs for field of view 25°.

7 Results: Near-Field BRDF Measurements

In this section, we apply the reconstruction method, and optimal sampling directions (Sec. 6, Fig. 8), to image-based near-field BRDF acquisitions of several real samples captured at two different laboratories located in different continents (UCSD in USA and DTU in Denmark). The two laboratory setups deviate slightly and will be described next. We used both approaches to demonstrate the robustness of our method with a variety of simple capture scenarios, which do not require exact configuration or precise alignment between views. We used a portion of the input sample with field of view of 25°, since that achieves near-optimal results (Fig. 6).

Setup A (DTU): In this setup, we utilize a high-precision robot-vision system to precisely position the camera relative to a material sample (Fig. 10 left). The angular error of this positioning is less than 1 degree. The camera used is a Point Grey Grasshopper 3, industrial CCD camera, mounted with a Kowa LM16SC 16mm lens. The light-source consists of arc holding halogen light-bulbs, evenly distributed from 0° to 90° in 7.5° steps.

Setup B (UCSD): We use a (distant) Dolan-Jenner DC 950 light source mounted on one arm of a spherical gantry; the gantry con-

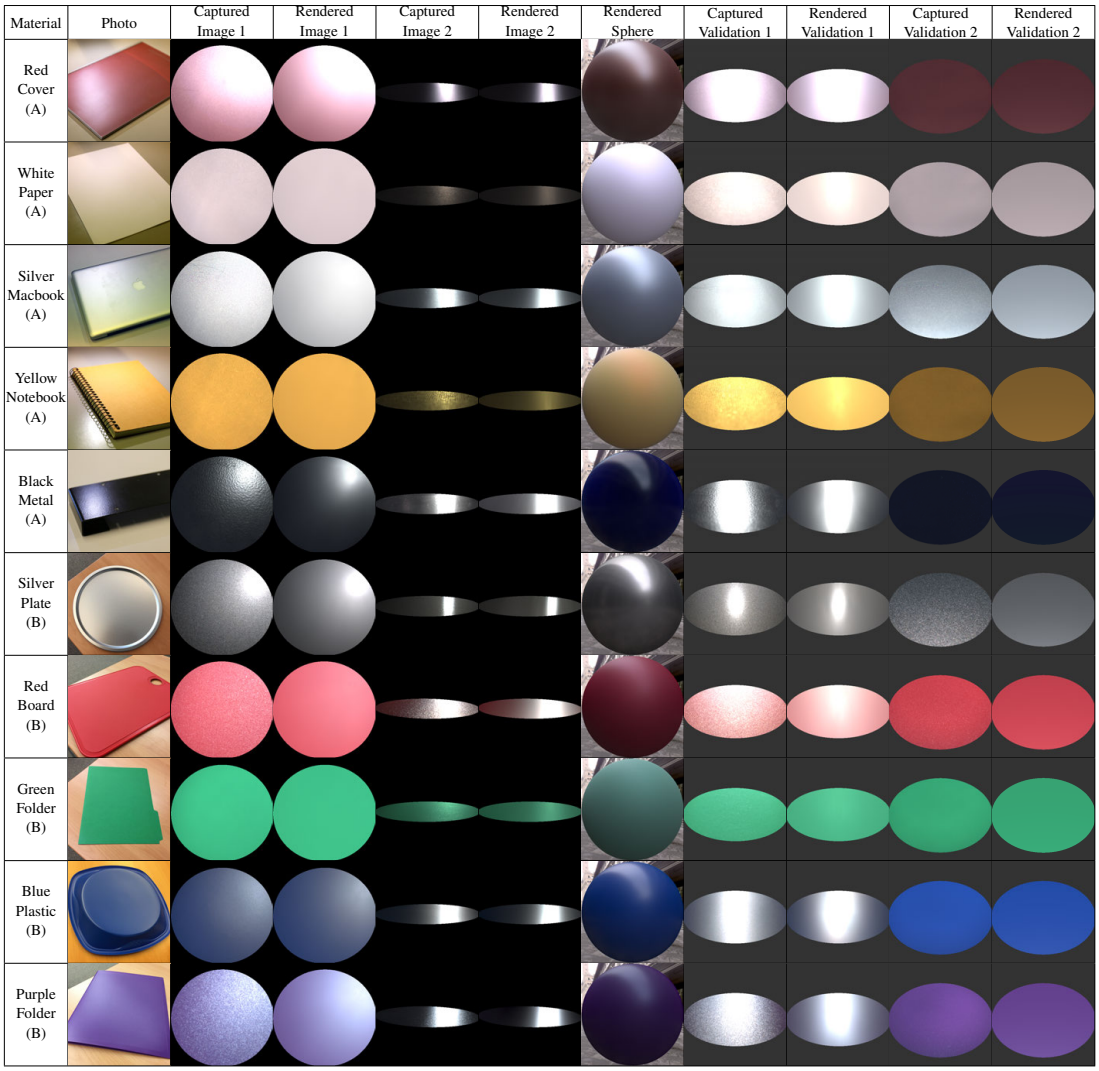

Figure 11: *Results for near-field BRDF acquisition on real materials. Materials labeled with (A) and (B) are captured by setups A and B. The material is shown first, followed by comparisons of input photographs and renderings with the measured BRDFs. These include both original views, as well as two new lightings and views not used as input. All renderings use the BRDF reconstructed from the two captured images. Good accuracy is obtained for all materials. We also visualize the full BRDF by rendering a sphere lit by an environment map. Note that we use optimal directions in Fig. 8 from the full MERL data, which differ slightly from those using 90 materials in Fig. 2.*

trols two high-precision arms having an angular resolution of 0.1°. However, the gantry's viewing arm/camera is too far away to obtain near-field images directly. We instead manually position a Canon EOS 5D Mark III camera mounted on a tripod close to the input sample (Fig. 10 right). In order to correctly position the camera, we place the gantry's two arms at the mirrored direction of the desired viewing location, and adjust the camera until it points towards both arms' center through a mirror. The final position of the camera is obtained through camera-calibration using a checkerboard.

The setups presented above have different limitations, in that the light-source confines setup A to a limited set of view/illumination configurations, whereas the manual positioning of the camera limits the precision of setup B. In both cases, we find the configuration that best matches the optimum directions in Figs. 8, 9. We thus demonstrate that our method is robust towards small variations in view/light configurations, while still obtaining very good results.

For acquisition, we capture multiple exposures to produce high-dynamic range images; each exposure is averaged over multiple images to reduce noise. The resulting values are then log-mapped, since our framework works with log-mapped BRDFs. Light inten-

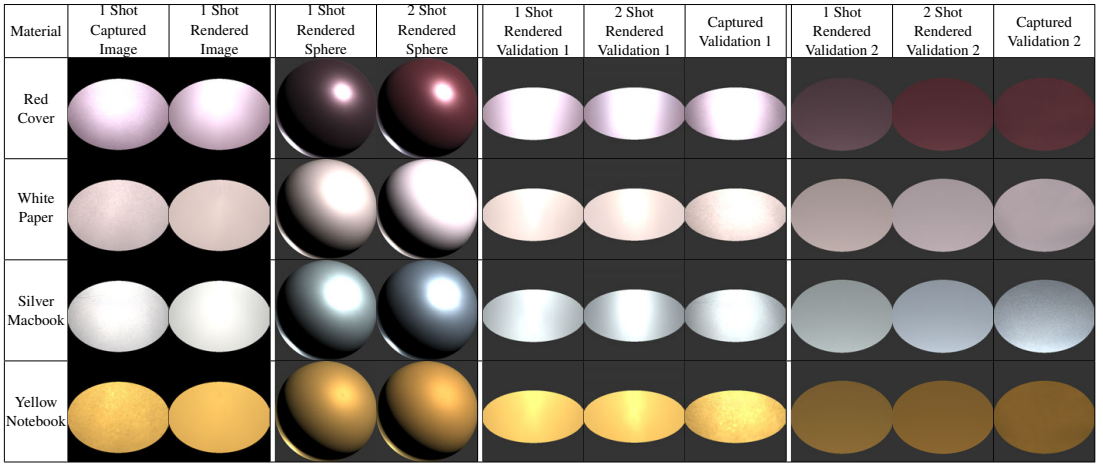

Figure 12: *Results for single image near-field BRDF acquisition on real materials, comparing one and two-shot reconstructions.*

sity is calibrated using a Spectralon material sample. By proper modeling of the intrinsic and extrinsic scene-parameters, all observed pixels (BRDF values) can be combined to form $\tilde{x}$ or $\tilde{y} = \tilde{x} - \tilde{\mu}$, using their corresponding view/light coordinates. With this, BRDF coefficients c can be solved from equation 4, and the full BRDF x recovered using equation 2, with a final step involving undoing the logarithmic mapping. We emphasize that all results in this section were obtained from only two image configurations of a standard flat planar sample, and in some cases only a single image.

Figure 11 shows several real samples, whose BRDFs we measured using two-shot near-field acquisition (analogous to Fig. 2 for MERL simulations). The first 5 rows are captured using setup A, and the last 5 rows with setup B. The colors differ slightly between the inset photograph and the comparisons, because of the off-white color of the actual light source. We compare the captured image (considering only the circular region of interest, per Fig. 4) with the rendering for both light-view input configurations. We also show two additional light-view configurations for validation, which were not used at all as an input. The validation configurations are chosen with $(\theta_h, \theta_d, \phi_d) = (0^\circ, 60^\circ, 0^\circ)$; $(22.5^\circ, 22.5^\circ, 0^\circ)$ to verify both specular and diffuse appearance. For visualization, we also show a rendered sphere with the corresponding BRDF lit by an environment map. The accompanying video shows the red cover, white paper and silver macbook under changing viewing directions with two illumination directions, comparing real and rendered results, including fading out the illumination to observe highlights without saturation. It can be seen that the real and rendered images match well. Even when the actual material has some noise or a slightly bumpy surface, we recover a smooth BRDF that is an accurate representation, for both diffuse and more glossy materials.

Finally, Fig. 12 shows what can be achieved with a single-shot capture (using setup A). In many cases, one input image is adequate to achieve reasonable results. However, the second input image does help refine the specular reflection somewhat, when comparing the rendered spheres. For example, white paper and yellow notebook are largely diffuse in the first image, and accurate specular and Fresnel information is only achieved at grazing angles in the second view. Moreover, in some cases, the diffuse color and shading can be somewhat refined by using both images.

We briefly discuss some limitations. As with all reconstruction methods based on the MERL data, we are ultimately limited by the subspace spanned by that data. Our simulations and experiments indicate excellent agreement with reference measurements, but there is unavoidable error when the material deviates from the MERL subspace. Moreover, for small field of view and BRDFs with broad highlights, our measurements may not capture the full range of the highlight in a single image, leading to under-estimating its width in reconstruction (light red paint in Fig. 2). For very dark materials, the noise can be over-fit, causing a blue tint for the black metal in the fifth row of Fig. 11. Finally, we do not account for surface imperfections or normal maps, which also contribute to the "noise" above. Nevertheless, as seen in Fig. 11, we produce accurate smooth BRDFs consistent with the input data.

8 Extension: Fixed Camera Setup

Our error analysis framework and optimization method for sampling directions is general, and could be applied in future to many different configurations. In this section, we consider a one-camera multiple-light case, where we use a single near-field viewing direction, while enabling multiple lighting directions. As before, we show that good results are achieved with two-shot acquisition with two lights. Note that we optimize for lights, and the single view direction, but do so while constraining the camera view to be the same (fixed) for all lighting directions. Using a fixed camera view may also enable simpler acquisition hardware in future. We also briefly discuss the symmetric case of a single fixed light direction, with multiple views. We consider a field of view of 25°.

Figure 13 shows the error of fixed camera, multiple light, and fixed light, multiple view, as a function of the number of images, also comparing to our point-sampling and near-field results. As before, our error analysis framework is essential for finding optimal directions, and condition number does not yield meaningful results.

The errors for one or two images are significantly lower than for point-sampling, and only somewhat more than the unconstrained near-field case considered previously (note that one shot acquisition is the same for fixed or free camera setup). However, the lack of flexibility when fixing light or view, leads to a slower decrease in error for more images. Figure 14(a) indicates the optimal two-image configuration for fixed camera and changing light. The camera is at a 64° angle to the surface, with light sources positioned to enable observation of both diffuse (light close to zenith) and specu-

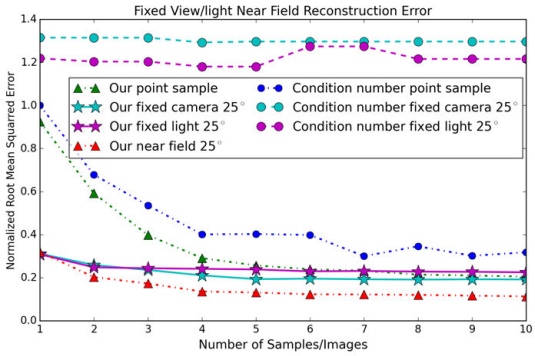

Figure 13: *Average RMS error over unknown samples for fixed camera/multiple lights, and fixed lighting direction/multiple views.*

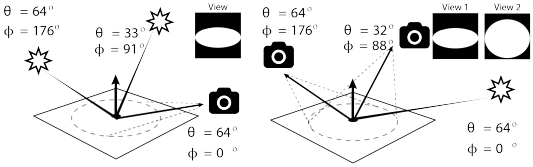

$\theta_h[^\circ]$	$\theta_d[^\circ]$	$\phi_d[^\circ]$
4	63	90
39	34	124

(a) *fixed view* 25°

$\theta_h[^\circ]$	$\theta_d[^\circ]$	$\phi_d[^\circ]$
4	63	90
39	33	126

(b) *fixed light* 25°

Figure 14: *Optimal configurations and angles for single view, multiple light and single light, multiple view cases, analogous to Fig. 9. Angles are shown as standard in-out and Rusinkiewicz coordinates.*

lar reflectance (light close to mirror direction). Having the camera at an angle to the surface enables capture of some Fresnel information, but a fixed camera setup will make it harder to fully reproduce grazing angles. We also show the analogous configuration for fixed light with multiple views in Fig. 14(b). Since fixed light/fixed view configurations are symmetric with similar error, we focus on the fixed camera setup, with only a single viewing direction, and therefore simpler calibration and alignment.

Figure 15 shows some synthetic MERL materials reconstructed with fixed view and two images. Note that the first input image is mostly specular while the second is mostly diffuse (dark for specular materials like metallic paint). The results are generally good in most cases. However, some ringing can be observed on the mostly diffuse white fabric. This corresponds to the higher error in Fig. 13, compared to the near-field case where both light and camera can move. Figure 16 shows comparable results for two real materials captured with setup B. We also show a validation view (specular with light/camera at 45°) not used as input. Good results are achieved with the two-shot fixed camera setup, although there is minor variance in the shape of the specular highlight.

Simple Extension to Spatially-Varying BRDFs: So far, we have not considered spatial variation. We take a first step with a simple extension for specific objects, which have two or more materials that have good coverage over the field of view (such as stars spread out on a background). The fixed-camera setup is ideal for this purpose, since no alignment/calibration between different near-field views is required. Note that this is an initial effort, and further work is required to extend the method to general SVBRDFs.

If we can cluster which pixels correspond to which material, we

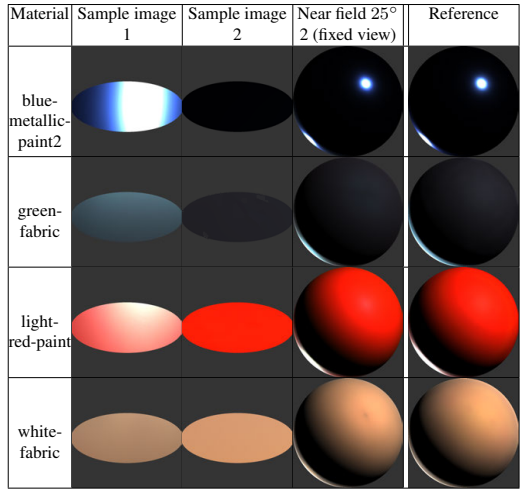

Figure 15: *MERL BRDFs reconstructed with fixed view and two images. This configuration works well for most materials.*

can separately estimate the BRDFs of the materials, using only the subset of pixels for that BRDF. The key requirement is *coverage* over the field of view, to enable one to see the full range of viewing angles. Using only a subset of pixels does not significantly increase error, especially since a 2D image already contains thousands to millions of observations. In practice, we cluster based on color observed in the second (diffuse) captured image. BRDFs are then estimated separately for each cluster. Figure 17 shows results for two greeting cards with spatial variation, acquired using setup B. In this example, we consider the full field of view, rather than only a circular region. As seen in Fig. 17, we cluster into three materials, and recover full BRDFs for all three materials. The rendered images are close to the captured, with the expected smoothing of surface roughness. (Microstructure and normal variations in the real object cause glints and rough specularities, which increase the apparent size of the highlight for the real object). The validation view, not used as input, also matches well.

9 Conclusions and Future Work

We have developed a method for acquisition of a full measured isotropic 3D BRDF from only two perspective images of a flat sample, lit with a directional light source. This is at least an order of magnitude reduction in effort over previous comparable techniques to measure a full BRDF, and requires only a standard flat homogeneous material sample. Our method is based on using the full 2D image information from a near-field view, and finds the best lighting and viewing directions by minimizing an estimate of the reconstruction error. We provide tables of these directions for different fields of view of the sample, which can directly be used by other researchers. Our major technical contribution is a formal derivation of reconstruction error, which provides a framework for minimization for both point-sampled and near-field BRDF acquisition, producing better results than the previous condition number heuristic.

In future work, we would like to explore other implications of our method. The new reconstruction error framework could have broad impact in problems like many light methods or computation of light transport matrices, where one seeks to reconstruct from a sparse set of samples. Finally, the one or two-shot nature of our method opens the possibility of designing new simple hardware, with light sources and camera in fixed position.

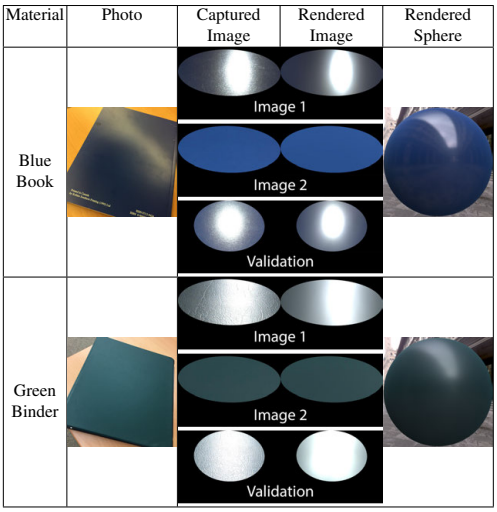

Figure 16: *Acquisition of real BRDFs from two images with fixed camera. We also show a validation view not used as input.*

Acknowledgements

We thank reviewers for their extensive comments. This work was supported by NSF grants 1451828, 1451830, and the UC San Diego Center for Visual Computing.

References

AITTALA, M., WEYRICH, T., AND LEHTINEN, J. 2013. Practical SVBRDF capture in the frequency domain. *ACM Transactions on Graphics (TOG) 32*, 4, 110.

AITTALA, M., WEYRICH, T., AND LEHTINEN, J. 2015. Two-shot SVBRDF capture for stationary materials. *ACM Transactions on Graphics (TOG) 34*, 4.

BRADY, A., LAWRENCE, J., PEERS, P., AND WEIMER, W. 2014. genBRDF: discovering new analytic BRDFs with genetic programming. *ACM Transactions on Graphics (TOG) 33*, 4.

DANA, K. J., AND WANG, J. 2004. Device for convenient measurement of spatially varying bidirectional reflectance. *J. Opt. Soc. Am. A 21*, 1, 1–12.

FOO, S. C. 1997. *A gonioreflectometer for measuring the bidirectional reflectance of material for use in illumination computation*. Master's thesis, Cornell University.

FUCHS, M., BLANZ, V., LENSCH, H. P., AND SEIDEL, H.-P. 2007. Adaptive sampling of reflectance fields. *ACM Transactions on Graphics (TOG) 26*, 2, 10.

GHOSH, A., ACHUTHA, S., HEIDRICH, W., AND O'TOOLE, M. 2007. BRDF acquisition with basis illumination. In *International Conference on Computer Vision*, 1–8.

HERTZMANN, A., AND SEITZ, S. M. 2003. Shape and materials by example: A photometric stereo approach. In *Computer Vision and Pattern Recognition*, vol. 1, IEEE, 533–540.

HUNTER, R. S., AND JUDD, D. B. 1939. Development of a method of classifying paints according to gloss. *ASTM Bulletin*, 97, 11–18.

HUNTER, R. S. 1987. *The measurement of appearance*. John Wiley & Sons.

KARNER, K., MAYER, H., AND GERVAUTZ, M. 1996. An image-based measurement system for anisotropic reflection. *Computer Graphics Forum (EUROGRAPHICS 96) 15*, 3, 119–128.

LENSCH, H. P. A., LANG, J., S, A. M., AND PETER SEIDEL, H. 2003. Planned sampling of spatially varying BRDFs. *Computer Graphics Forum 22*, 3, 473–482.

LOW, J., KRONANDER, J., YNNERMAN, A., AND UNGER, J. 2012. BRDF models for accurate and efficient rendering of glossy surfaces. *ACM Transactions on Graphics (TOG) 31*, 1.

MARSCHNER, S., WESTIN, S., LAFORTUNE, E., TORRANCE, K., AND GREENBERG, D. 2000. Image-Based BRDF Measurement including Human Skin. In *Eurographics Rendering Workshop*, 139–152.

MATUSIK, W., PFISTER, H., BRAND, M., AND MCMILLAN, L. 2003. A data-driven reflectance model. *ACM Transactions on Graphics (TOG) 22*, 3, 759–769.

MATUSIK, W., PFISTER, H., BRAND, M., AND MCMILLAN, L. 2003. Efficient isotropic BRDF measurement. In *Eurographics Rendering Workshop*, 241–247.

MCCOOL, M., ANG, J., AND AHMAD, A. 2001. Homomorphic Factorization of BRDFs for High-Performance Rendering. In *SIGGRAPH 01*, 171–178.

MEYER, M., AND ANDERSON, J. 2007. Key point subspace acceleration and soft caching. *ACM Transactions on Graphics (TOG) 26*, 3.

NGAN, A., DURAND, F., AND MATUSIK, W. 2005. Experimental analysis of BRDF models. In *Eurographics Symposium on Rendering*, 117–126.

NIELSEN, J. B., JENSEN, H., AND RAMAMOORTHI, R. 2015. On optimal, minimal BRDF sampling for reflectance acquisition. *ACM Transactions on Graphics (TOG) 34*, 6.

NOLL, T., STRICKER, D., KOHLER, J., AND REIS, G. 2013. A full-spherical device for simultaneous geometry and reflectance acquisition. In *Proceedings of the on Applications of Computer Vision*, IEEE Computer Society, WACV, 355–362.

REN, P., WANG, J., SNYDER, J., TONG, X., AND GUO, B. 2011. Pocket reflectometry. *ACM Transactions on Graphics 30*, 4.

ROMEIRO, F., AND ZICKLER, T. 2010. Blind reflectometry. In *European Conference on Computer Vision*, 45–58.

ROMEIRO, F., VASILYEV, Y., AND ZICKLER, T. 2008. Passive reflectometry. In *European Conf. Computer Vision*, 859–872.

RUSINKIEWICZ, S. 1998. A new change of variables for efficient BRDF representation. In *Eurographics Rendering Workshop*, 11–22.

TORRANCE, K. E., AND SPARROW, E. M. 1967. Theory for off-specular reflection from roughened surfaces. *JOSA 57*, 9, 1105–1112.

TUNWATTANAPONG, B., FYFFE, G., GRAHAM, P., BUSCH, J., YU, X., GHOSH, A., AND DEBEVEC, P. 2013. Acquiring reflectance and shape from continuous spherical harmonic illumination. *ACM Transactions on Graphics (TOG) 32*, 4, 1–12.

WARD, G. J. 1992. Measuring and modeling anisotropic reflection. In *SIGGRAPH 92*, 265–272.

WESTLUND, H. B., AND MEYER, G. W. 2001. Applying appearance standards to light reflection models. In *SIGGRAPH 01*, 501–510.

Appendix A: Details of Reconstruction Error

We analyze equation 12 in more detail, also relating it to the condition number metric. It is convenient to denote $y = Qc$, where c is the accurate coefficient vector to reconstruct the BRDF. In this case, noting $Q^+Q = I$,

$$E_{\text{recon}} = \left|Q\left(Q^+ - (SQ)^+_\eta S\right)Qc\right| = \left|Q\left(I - (SQ)^+_\eta SQ\right)c\right|. \tag{16}$$

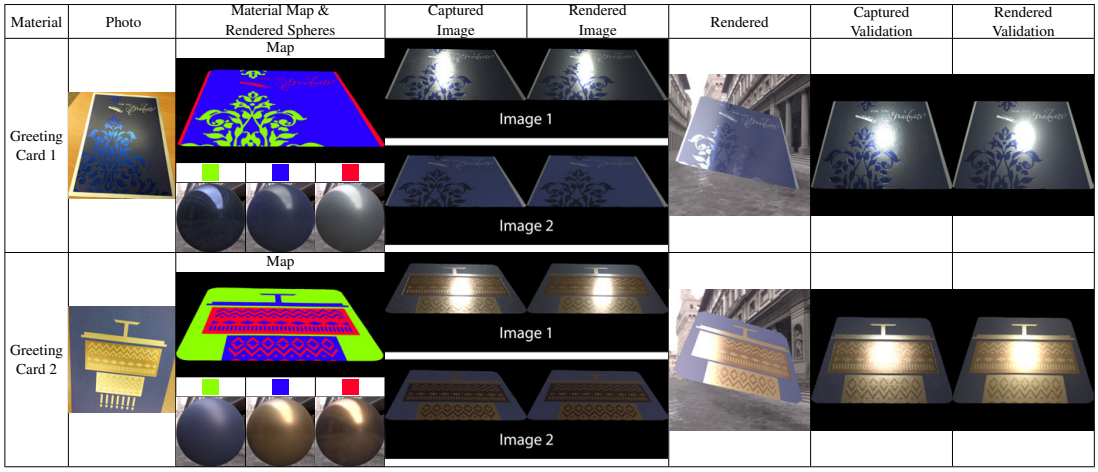

Figure 17: *Acquisition of spatially-varying BRDFs from two images with fixed camera. Note the close match of captured and rendered images, including in the validation view, not used as input (rightmost column). Rendered images are under environment lighting. We also show the 3 material clusters used in each case, and spheres rendered with the full BRDFs recovered for each of the 3 materials.*

Now, let us denote the SVD of $SQ = \tilde{Q}$ as $A\Lambda B^T$. From equation 5, $(SQ)^+_\eta = \tilde{Q}^+_\eta = B\Lambda^+_\eta A^T$. Now,

$$(SQ)^+_\eta (SQ) = B\Lambda^+_\eta A^T A\Lambda B^T = B\Lambda' B^T, \tag{17}$$

where $\Lambda' = \Lambda^+_\eta \Lambda$ is a diagonal matrix. If the singular values in Λ are σ (and those in Λ^+_η are $\sigma/(\sigma^2+\eta)$), then the singular values in Λ' are $\sigma^2/(\sigma^2+\eta)$. Further simplifying,

$$E_{\text{recon}} = \left| Q\left(I - B\Lambda' B^T\right) c \right| = \left| Q\left(B\Gamma B^T\right) c \right|, \tag{18}$$

where Γ is also a diagonal matrix with singular values $1 - \frac{\sigma^2}{\sigma^2+\eta} = \eta/(\sigma^2+\eta)$. To understand E_{recon}, we care about the singular values in Γ. The largest singular value is given by the minimum $\sigma_{\min}$, with value $\eta/(\sigma^2_{\min}+\eta)$. In general, we will reduce E_{recon} if we avoid small σ. Indeed, the condition number optimization affects the σ values and tries to make $\sigma_{\min}$ larger to reduce the condition number. However, it is not explicitly minimizing the above expression. In contrast, our approach explicitly considers the end-to-end system, as well as the effect of Q, the MERL BRDF materials encoded in the coefficient vector c, and the full spectrum of singular values, to fully minimize the error E_{recon}.

Appendix B: Point-Sampled BRDF Measurement

The main text discusses near-field image-based BRDF measurement. Here, we show that the new error metric also somewhat improves point-sampled BRDF acquisition. We compare our results to [Nielsen et al. 2015] with 5 directions in Fig. 18. (The dotted black curve at the bottom is the lower bound when using all of the input directions, essentially the unavoidable error $E_{\text{deviation}}$.) Note that this evaluation is identical to Fig. 8 in their paper, using the same graphs for their method, as well as parametric fits and the industry-standard 5 directions in [Westlund and Meyer 2001]. It is clear that we have somewhat lower error. This is not surprising since these results are computed assuming the observations are accurate without noise, while the condition number metric measures only sensitivity to noise, not reconstruction error. The supplementary material shows similar results for an example with 20 measurements and 2% noise. Nevertheless, minimizing the condition number is a reasonable heuristic for this setup.

We can also plot the average error over the unknown samples in the MERL BRDF database vs. the number of measurements n in Fig. 19. For both standard point-sampled acquisition, and the image-based spherical acquisition method of [Marschner et al. 2000] (extended to use optimal directions computed with either our error metric or using condition number), our method

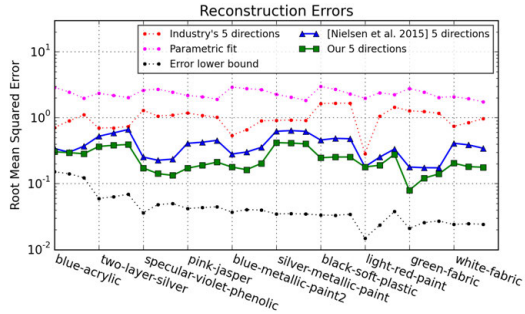

Figure 18: *Comparison of reconstruction with our new optimized 5 directions, and those from [Nielsen et al. 2015], parametric fits, and industry-standard directions. Our method (green curve) produces lower error than previous work (blue curve) on each BRDF.*

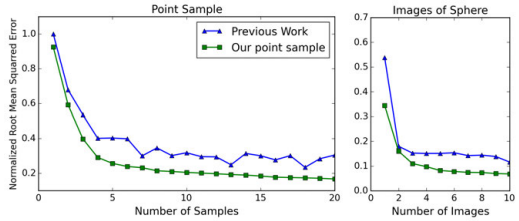

Figure 19: *Reconstruction error versus number of measurements. We obtain a smooth graph, strictly lower error than previous work.*

gives somewhat lower error. Another important observation is the shape of the curves. The result from [Nielsen et al. 2015] oscillates somewhat, since the condition number metric is not directly tied to (or always monotonic with) the actual error. By minimizing the actual expected reconstruction error, we obtain a smooth graph. The supplementary material provides our improved point-sampling directions, and comparisons for a few materials from the MERL database. In some cases we do qualitatively better, while there is a minor improvement in other cases. In general, our 5 directions is comparable to 20 samples using the previous condition number metric.

Appendix G

A Robot based Gonioreflectometer

Technical Note
A Robot based Gonioreflectometer

Jannik Boll Nielsen and Rasmus Ahrenkiel Lyngby

Spring 2016

In the Section for Image Analysis and Computer Graphics at the Technical University of Denmark we have an ABB welding robot at our hands. By equipping the robot with a camera and combining this setup with an arc-formed point-light array, we can semi-densely sample light reflections off a flat material sample for various configurations of incoming and outgoing light directions. See figure 1 for an illustration of the measurement system.

The basic idea is to move the camera around a sample which is placed under the light arc, while capturing the sample reflectance under each of the light sources, thus sampling all combinations of incoming and outgoing light rays. Remembering that the BRDF obeys Helmholtz reciprocity, we actually sample both configurations of light and camera positions in one go. In addition, as previously mentioned, we limit ourselves to isotropic BRDFs, why a rotation around the surface normal of the incoming and outgoing ray does not change the BRDF. Thus, we can simply keep the light arc at a fixed position and only move the camera around, hereby sampling the entire isotropic BRDF.

The factors limiting how dense we can sample surface reflectance are the spacing between the light-sources in the arc and the resolution of the Cartesian space in which the robot moves. The robot has a non-uniform grid of reachable positions, but in general the spacing between two reachable positions is sub-millimeter. The light arc is constructed with a fixed set of bulbs with a spacing of 7.5° and has a radius of 1000[mm]. Thus, the resolution of the robot is orders of magnitude higher than that of the light arc. However, we have assessed that a bulb spacing of 7.5° provides a good compromise between sample rate and measurement time, thus providing a semi-dense sampling within a reasonable time frame.

The light sources in the arc must be as close to point sources as possible. In theory, with only one light source on, this will ensure that each infinitesimal point on the sample surface will receive only a single, incoming ray of light. In effect, we can measure the reflectance of a single ray at an infinitesimal point by narrowing the camera's field of view to a fraction of a degree, such that it observes only a single outgoing ray at a time. That can be done by combining

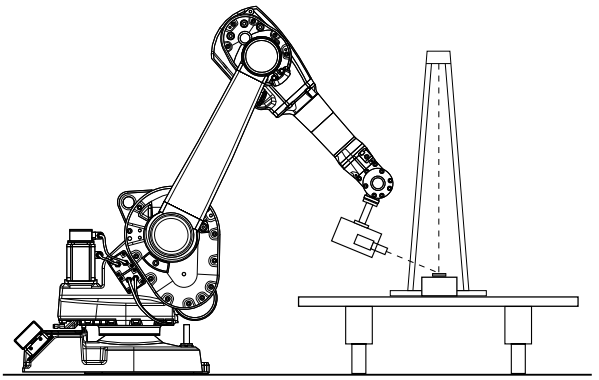

Figure 1: Illustration of the surface reflectance measuring system. It contains the robot, the light arc, a table, a sample stand, and the sample, which is illustrated by the gray box.

a long focal length and image cropping. However, in practice, it is impossible to move the camera around the sample while keeping its narrow field of view exactly aligned with the same infinitesimal point on the surface. Thus, a broader field of view is used, and the mean value of reflected light within the field of view is used as an estimate of the point radiance. In addition, light bulbs are not be perfect point sources as they have a spatial extend. Thus, they would have to be placed infinitely far away to act as true point sources. As it is not feasible to have a light arc with an infinite radius, we have compromised by choosing a sample-to-light distance which is at least three times longer than the camera-to-sample distance.

The camera is moved around the sample point such that it follows the surface of a sphere which is centered on the sample point and has a radius of 350[mm]. The camera is oriented such that it always points toward the sphere center. The reflected light is symmetric around the axis running parallel with, and through, the light arc. Put in another way, the light reflected to the right of the arc is identical to that reflected to the left. Thus, if we sample only the first half of the hemisphere from azimuth 0° to 180°, the other half going from 180° to 360° is simply identical to the first half, mirrored over the axis of the light arc, given that the arc is positioned at 0°. The camera path is defined in spherical coordinates with a resolution of 7.5° in both azimuth and elevation. Thus, the

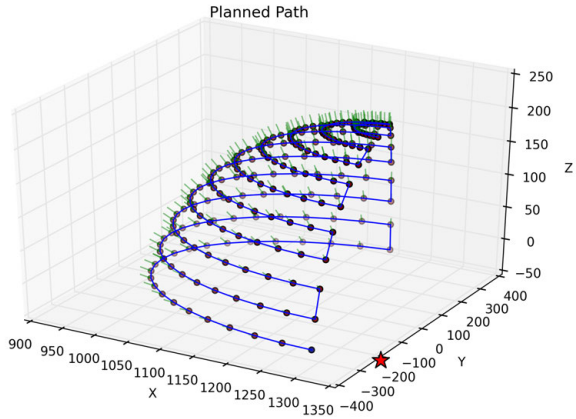

Figure 2: Illustration of the camera's trajectory. The star indicates the sphere center, the purple dots indicates sample positions, and the green lines indicates the camera orientation. We do not sample elevations of 0° as they cause no reflection. Thus, the first row is located at an elevation of 7.5°.

Cartesian equivalent of a given spherical camera position is calculated as follows:

$$x_{ij} = x_0 + r \sin\theta_i \cos\phi_j \quad \text{[mm]} \quad (1)$$

$$y_{ij} = y_0 + r \sin\theta_i \sin\phi_j \quad \text{[mm]} \quad (2)$$

$$z_{ij} = z_0 + r \cos\theta_i \quad \text{[mm]} \quad (3)$$

Where:

θ_i is the inclination of sample row i. [rad]

ϕ_j is the inclination of sample column j. [rad]

$[x_0, y_0, z_0]^T$ is the center of the sphere. [mm]

The orientation of the camera is calculated as follows:

$$\beta_i j = \frac{\pi}{2} + \theta_i \quad \text{[rad]} \quad (4)$$

$$\gamma_i j = \phi_j \quad \text{[rad]} \quad (5)$$

Where:

$\beta_i j$ is the camera pitch. [rad]

$\gamma_i j$ is the camera yaw. [rad]

The Cartesian coordinates and orientations for each sample point are calculated and stored in a matrix, which at run time is fed one-by-one to the robot in order to move it, and thus the camera, around. In practice, the orientation of the camera is converted to quaternion representation to comply with the robot controller. The camera trajectory with sample positions are illustrated in figure 2.

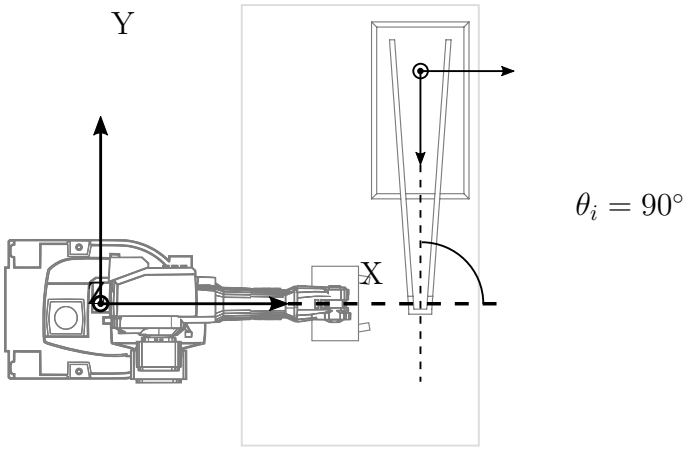

Figure 3: Illustration of the robot coordinate system and the relative position of the light arc. The intersection between the two stippled lines indicates the sphere path center where the sample is placed. The azimuth of the incoming light is $\theta_i = 90°$.

Note that the orientation of the robots coordinate system has to be taken into account. In practice, points lying on the robots x-axis corresponds to an azimuth of 0°. In order to operate the robot within its working area, we had to position the arc along the robots y-axis, why our coordinate system is rotated by 90°. This is illustrated in figure 3.

In order to truly measure the BRDF of a material, we would have to know the exact irradiance of the light sources in all directions and the correspondence between camera pixel intensity and radiance. In addition, we would need to know the exact geometry between the light sources, the sample surface, and the camera in order to get an accurate measure of the reflectance. This is difficult and impractical to measure. Instead, we get around this problem by using Spectralon®. Spectralon is patented and manufactured by Labsphere. In short, it is a material which has $> 99\%$ diffuse reflectance. Its reflection is thus very Lambertian, meaning that the relationship between radiance and irradiance is approximately given by $L^{(L)} = \mathbf{n}^T\mathbf{l}E$ where $\mathbf{n}$ and $\mathbf{l}$ are the surface normal and the unit-length incoming light direction, respectively. Note that the outgoing direction is not a part of the relationship, why the radiance is identical for all view directions. Thus, Spectralon uniformly spreads the incoming flux at a point over the hemisphere of that point with very little loss, meaning that the radiance integrated over the hemisphere is approximately equal to the incoming irradiance. This allows us to use Spectralon as a reference to which a given material sample can be compared. Put in another way, we can measure the BRDF for a given pair of incoming and outgoing directions for a given material by calculating the ratio between the reflected intensity of the material and the

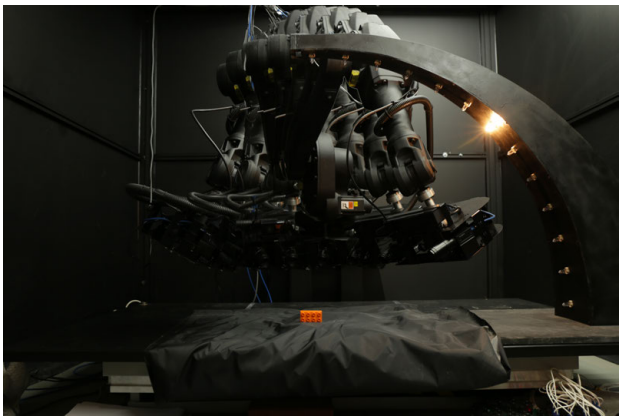

Figure 4: Illustration of the measurement process for a single light source. The image is composed of a sequence of images as the robot sweeps across one row of the path sphere.

reflected intensity of Spectralon for the same directions. This is defined as follows:

$$f_r(\theta_i, \theta_o, \phi_o) = \frac{I^{(M)}(\theta_i, \theta_o, \phi_o)}{I^{(S)}(\theta_i, \theta_o, \phi_o)} \qquad [\mathrm{sr}^{-1}] \qquad (6)$$

Where:

$I^{(M)}$ is the intensity of the material. $[\,\cdot\,]$

$I^{(S)}$ is the intensity of Spectrolon. $[\,\cdot\,]$

Note that this is a relative measure, why the unit which is used to measure the intensity is irrelevant. It could be flux, but it could as well be pixel intensity as a count from 0 to 1 or from 0 to 255.

The above constitutes all the components needed for constructing a BRDF measurement system. The work flow is defined in table 1 and the process is illustrated in figure 4.

Table 1: Work flow to measure a BRDF

Step		**Time**	**Notes**
1	Tool transform	1[h]	In practice, the tool transform only has to be estimated once. However, as the tools changes with temperature, humidity, and wear and tear, it is a good idea to re-estimate it regularly.
2	Alignment of Spectralon to arc	5[min]	The surface of the Spectralon sample has to be carefully aligned with the center of the semicircle formed by the light arc.
3	Spectralon measurement	3[h]	As with the tool transform, this process can be omitted. However, it should be conducted at least once for every new measurement day.
4	Alignment of material to arc	5[min]	Replace the spectralon sample with the material sample. Make sure the surface of the material align exactly with the surface of the Spectralon.
5	Material measurement	3[h]	
6	BRDF calculation	5[min]	Use Equation 6 to calculate the BRDF of the material.
Total		7[h]:15[min]	
Additional samples		3[h]:10[min]	

Appendix H

BRDF Estimation using Spectralon

Technical Note
BRDF Estimation using Spectralon

Jannik Boll Nielsen

December 2015

1 Introduction

When measuring BRDFs in a gonioreflectometer setup, usually one of two strategies is employed: the absolute, or the relative approach.
In the absolute method, the radiance of both the sample and the light-source are measured, and the two are compared to obtain the reflectance and BRDF. This, however, requires a direct measurement of the light-source, introducing a need for very high dynamic range detector, which may be a limiting factor in many setups.
In the relative method, a reference sample with known reflectance, usually Spectralon®, is used to infer the irradiance of the unknown material. Based on this, the reflectance and BRDF can be estimated using a much lower detector dynamic range. Obviously this advantage breaks when mirror-like objects are being measured, as this would correspond to measuring the light-source itself.

In this technical note we explain the relative method in detail, with the intention of enabling the reader to conduct correct BRDF measurements using this method. We utilize a camera-based gonioreflectometer and a flat Spectralon® reference sample.

2 Experiment Geometry

Before covering the radiance-computations, let us initially define the geometry of the experiment, with a special emphasis on the camera geometry. In Fig. 1 the layout of a standard measurement is illustrated: A point on a material sample is illuminated by a light-source from an angle θ_i, and a camera observes the point in a single pixel at an angle θ_o and a distance of r.

In this setup we assume known experiment geometry (θ_i, θ_o, r), as well as known camera parameters (f, D). What is usually unknown, however, is the solid angle,

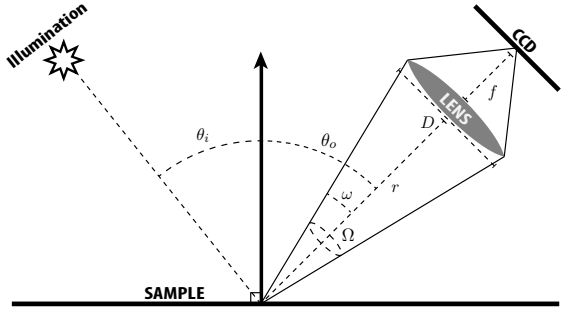

Figure 1: Layout with thin lens model camera as a detector. The camera is placed at a distance r from the sample, at an angle θ_o relative to the surface normal. Illumination comes from a point-source at angle θ_i. The camera has a focal length f and a lens diameter of D. Ignoring vignetting, any pixel on the camera CCD will approximately cover the solid angle Ω from the point measured on the sample.

Ω, observed by a single pixel on the CCD chip. This angle is necessary for scaling reflectances, as will be shown in Sec. 4.
The angle ω, depicted in Fig. 1 is easily seen to be:

$$\omega = \arctan\left(\frac{D}{2r}\right) \quad [rad] \tag{1}$$

From this, the solid angle Ω, corresponding to a cone with an apex angle of 2ω, is:

$$\begin{aligned} \Omega &= 2\pi\left(1-\cos\left(\omega\right)\right) && (2)\\ &= 2\pi\left(1-\cos\left(\arctan\left(\frac{D}{2r}\right)\right)\right) && (3)\\ &= 2\pi\left(1-\frac{1}{\sqrt{1+\left(\frac{D}{2r}\right)^2}}\right) \quad [sr] && (4) \end{aligned}$$

Thus, if ignoring vignetting effects that may occur at non-center pixels, the solid angle observed by a pixel on the camera CCD is approximately given by Eq. 4. Note however that this is a very simplified model of the camera system and as such, Eq. 4 is only an approximation.

The effective diameter, D, of the lens is not (necessarily) the physical diameter of the optical element. This can be due to the construction of the lens or, especially, due to the camera-iris controlling the exposure. Instead, D can be inferred by the focal length f and the f-number (F) used during acquisition. The relation between the effective lens diameter and the f-number is given by:

$$D = \frac{f}{F} \quad [m] \tag{5}$$

3 Camera Exposure Estimation

We here briefly introduce the principles behind converting from pixel intensities, Z, to exposure values, X, up to a factor of scale.
For convenience we remind the reader of the definition of radiant exposure:

$$H = E \cdot \Delta t, \quad \left[J/m^2\right] \tag{6}$$

where, E is the irradiance and Δt is the exposure time in seconds.
In our case we do not know the exact exposure, but only to a factor of scale, and as such refrain from using H and instead use X to emphasize that the absolute value is unknown:

$$X = k \cdot H \tag{7}$$

The CCD in a digital camera is usually very linear, i.e. there is a linear relation between the CCD signal and the irradiance. Often, however, camera manufacturers introduce some non-linear mapping, f, for various purposes. As a result, one cannot expect a linear relationship and should instead estimate a correct mapping to compensate for any non-linearities.
Debevec and Malik present in [1] an approach for estimating f^{-1}, such that $X = f^{-1}(Z)$, under the assumption of f being a monotonically increasing function. Their method involves capturing a range of images of a scene using a range of known exposure times, and they show that in log-space the mapping f^{-1} can be solved as a linear system. We will not present the details of the method here, but refer the reader to [1] for more information.

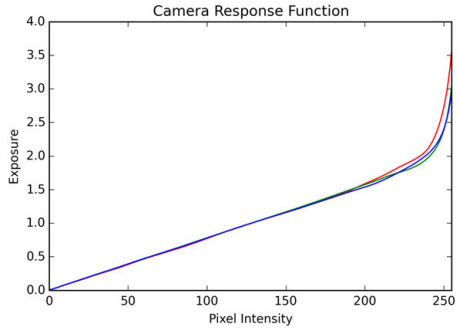

Figure 2: Camera response function, f^{-1}, for a Point Grey Scorpion CCD camera. The response function was obtained using 5 images acquired with exposure-times of $\Delta t = \{12.5, 25, 50, 100, 200\} ms$. As can be seen for pixel intensities up to around 200-225, the response function is very linear.

The method introduced above enables two important parts of BRDF acquisition: 1) It allows for the conversion to exposure (and irradiance) from pixel-intensities; and 2) It enables combining multiple images with different exposures into high dynamic range images.

In Fig. 2 an example of a measured Camera Response Function, f^{-1}, is shown. The function was estimated based on 5 images with exposure times of $\Delta t = \{12.5, 25, 50, 100, 200\} ms$. For this camera the response function is very linear for pixel intensities up to 200-225.

4 BRDF Estimation using Spectralon

In the relative method reflectance and BRDF are estimated by inspecting the ratio between the sensor-irradiance observing an unknown material and the sensor-irradiance when observing a known reference material from the same direction. In practice this corresponds to, for a given angle, capturing an image of the unknown material, capturing an image of the reference material, converting to exposure values, and calculating the ratio between the two. As stated in the introduction, we use Spectralon as a reference material due to the unique property that it has a near unit directional reflectance for all incoming and outgoing directions.

Let the observed exposure in a pixel imaging the unknown material be denoted $X_{\mathtt{mat}}$ and let the observed exposure in the same pixel imaging the reference material be denoted $X_{\mathtt{ref}}$. The ratio of the two scaled exposures will then be equal to the ratio of the irradiances:

$$\frac{X_{\mathtt{mat}}}{X_{\mathtt{ref}}} = \frac{k\, H_{\mathtt{mat}}}{k\, H_{\mathtt{ref}}} = \frac{H_{\mathtt{mat}}}{H_{\mathtt{ref}}} = \frac{E_{\mathtt{mat}}\, \Delta t}{E_{\mathtt{ref}}\, \Delta t} = \frac{E_{\mathtt{mat}}}{E_{\mathtt{ref}}} \tag{8}$$

In addition, since the images are acquired with the same imaging device, the pixel size of the two observations must be equal. We therefore see that the ratio of irradiances is in fact equal to the ratio of the radiant flux received:

$$\frac{E_{\mathtt{mat}}}{E_{\mathtt{ref}}} = \frac{\frac{d\Phi_{\mathtt{mat}}}{dA}}{\frac{d\Phi_{\mathtt{ref}}}{dA}} = \frac{d\Phi_{\mathtt{mat}}}{d\Phi_{\mathtt{ref}}} \tag{9}$$

Let us introduce the solid angle covered by a single pixel, $\Omega_{\mathtt{pixel}}$, described in Sec. 2. The Spectralon material has the unique property that the directional reflectance is near unity ($\rho_{\mathtt{ref}} \approx 1$). This means that the reflected flux, $\Phi_{\mathtt{ref}}$, equals the received flux from the illumination source, $\Phi_{\mathtt{ill}}$, scaled by the fraction of the hemisphere covered by the observer solid angle, $\frac{\Omega_{\mathtt{pixel}}}{\pi}$, and a cosine term:

$$\Phi_{\mathtt{ref}} = \frac{\Phi_{\mathtt{ill}}\, \Omega_{\mathtt{pixel}} \cos\theta_o}{\pi} \tag{10}$$

By definition $\rho_{\mathtt{mat}} = \frac{d\Phi_{\mathtt{mat}}}{d\Phi_{\mathtt{ill}}}$. Hence we can replace the two, revealing that the ratio of the observed pixel intensities is in fact the scaled reflectance of the unknown material:

$$\frac{d\Phi_{\mathtt{mat}}}{d\Phi_{\mathtt{ref}}} = \frac{d\Phi_{\mathtt{mat}}}{\frac{d\Phi_{\mathtt{ill}}\, \Omega_{\mathtt{pixel}} \cos\theta_o}{\pi}} = \frac{\rho_{\mathtt{mat}}\, \pi}{\Omega_{\mathtt{pixel}} \cos\theta_o} \tag{11}$$

We thus see that the ratio between the observed exposure of an unknown material sample, and the observed exposure of a Spectralon reference sample, is closely connected to the reflectance of the unknown material sample:

$$\rho_{\mathtt{mat}} = \frac{d\Phi_{\mathtt{mat}}}{d\Phi_{\mathtt{ref}}} \frac{\Omega_{\mathtt{pixel}} \cos\theta_o}{\pi} \tag{12}$$

$$= \frac{X_{\mathtt{mat}}}{X_{\mathtt{ref}}} \frac{\Omega_{\mathtt{pixel}} \cos\theta_o}{\pi}. \tag{13}$$

The BRDF is defined as the ratio between radiance leaving the sample and the irradiance hitting the sample:

$$f_{\mathtt{mat}} = \frac{dL_{\mathtt{mat}}}{dE_{\mathtt{ill}}} \quad \left[sr^{-1}\right] \tag{14}$$

With radiance being defined as:

$$L_{\mathtt{mat}} = \frac{d^2\Phi_{\mathtt{mat}}}{d\Omega\, dA\, \cos\theta_o} \quad \left[W \cdot m^{-2} \cdot sr^{-1}\right], \tag{15}$$

and irradiance defined as:

$$E_{\mathtt{ill}} = \frac{d\Phi_{\mathtt{ill}}}{dA} \quad \left[W \cdot m^{-2}\right], \tag{16}$$

it can be recognized that the BRDF may be rewritten to:

$$f_{\mathtt{mat}} = \frac{\frac{d^2\Phi_{\mathtt{mat}}}{d\Omega\, dA\, \cos\theta_o}}{\frac{d\Phi_{\mathtt{ill}}}{dA}}$$

$$= \frac{d^2\Phi_{\mathtt{mat}}}{d\Phi_{\mathtt{ill}}\, d\Omega\, \cos\theta_o}$$

$$= \frac{d\rho_{\mathtt{mat}}}{d\Omega\ cos\theta_o}$$

$$\approx \frac{\rho_{\mathtt{mat}}}{\Omega_{\mathtt{pixel}}\, \cos\theta_o} \quad \left[sr^{-1}\right]. \tag{17}$$

We thus see that in order to calculate the approximate BRDF value for a given view/illumination configuration, the reflectance of the material should be scaled by the solid angle spanned by a pixel and the cosine of the observer to account for geometry.
Combining this with the derivation from Eq. 13, we obtain:

$$f_{\mathtt{mat}} \approx \frac{X_{\mathtt{mat}}}{X_{\mathtt{ref}}\, \pi}. \tag{18}$$

To conclude, the estimation of the BRDF requires only the ratio between the two exposures captured, $X_{\mathtt{mat}}$ and $X_{\mathtt{ref}}$. If reflectance is needed, knowledge of the direction from which one is observing a sample, and the size of the solid angle covered by the camera, is also required.
A summery of the full acquisition procedure is as follows:

1. From a set of calibration images, recover the inverse response function (f^{-1}) of the camera, using the method of Debevec and Malik [1].
2. Capture an image of the material sample and another image of a Spectralon reference sample.
3. Convert pixel intensities, $Z_{\texttt{mat}}$ and $Z_{\texttt{ref}}$, to exposures, $X_{\texttt{mat}}$ and $X_{\texttt{ref}}$.
4. Estimate the material BRDF, $f_{\texttt{mat}}$, for the given direction using Eq. 18.
5. (Optionally) Using the known setup parameters, θ_o, r, D (or f and F), estimate the solid angle covered, $\Omega_{\texttt{pixel}}$ from Eq. 4, and scale the BRDF value to a reflectance value using Eq. 13.

5 Different surface normals

In eq. (18) we assume that the surface normal of the reference (Spectralon) sample is equal to that of the material sample. Furthermore, we assume that the exposures of the reference and material were obtained from the same physical distance. In scenarios where more complex geometry is being observed this assumption breaks, and the light-source intensities inferred by the reference sample should be scaled accordingly. The scenario is depicted in Fig. 3, where d is the distance from the light-source to the observed point on the surface, and θ_i is the angle between the surface normal at the same point and the direction to the light-source.

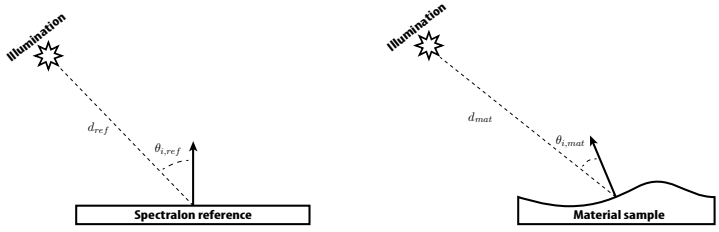

Figure 3: A case where the normal of the material sample is *not* equal to the normal of the reference (Spectralon) sample. d is the distance from the light-source to the observed point and θ_i is the angle between the surface normal and the direction to the light-source.

To compensate for the change in surface normal, we simply normalize by the cosine term the reference was observed under and scale by the cosine term the material was observed under:

$$\begin{aligned} f_{\texttt{mat}} &\approx \frac{X_{\texttt{mat}}}{X_{\texttt{ref}} \frac{\cos(\theta_{i,mat})}{\cos(\theta_{i,ref})} \pi} \\ &\approx \frac{X_{\texttt{mat}}}{X_{\texttt{ref}} \pi} \frac{\cos(\theta_{i,mat})}{\cos(\theta_{i,ref})} \end{aligned} \tag{19}$$

To address the difference in distance to the samples, knowing that the intensity of light follows the inverse square law, we can scale by the squared ratio of distances.

$$f_{\mathtt{mat}} \approx \frac{X_{\mathtt{mat}}}{X_{\mathtt{ref}}\,\pi}\,\frac{\cos(\theta_{i,ref})}{\cos(\theta_{i,mat})}\,\frac{d_{mat}^2}{d_{ref}^2} \tag{20}$$

Equation (20) thus constitutes the BRDF conversion that fully compensates for differing surface normals and observation illumination distances as depicted in figure 3. Note that X_{ref}, $\theta_{i,ref}$ and d_{ref}, providing the illumination information in the scene, are all constant and can be precomputed:

$$k_{ill} = \frac{\cos(\theta_{i,ref})}{X_{\mathtt{ref}}\,d_{ref}^2\,\pi} \tag{21}$$

$$f_{\mathtt{mat}} \approx X_{mat}\,\frac{d_{mat}^2}{\cos(\theta_{i,mat})}\,k_{ill} \tag{22}$$

References

[1] Paul E Debevec and Jitendra Malik. Recovering high dynamic range radiance maps from photographs. In *ACM SIGGRAPH 2008 classes*, page 31. ACM, 2008.

Appendix I

Obtaining Environment Maps for Global Illumination

Technical Note
Obtaining Environment Maps for Global Illumination

Jannik Boll Nielsen

Spring 2016

Proper radiometric modelling is crucial for reproducing scene-appearance accurately. This section describes how the radiometric scene-properties can be acquired. We separate this task into two subtasks:

1. Capturing and modelling *global* radiometric effects.
2. Capturing and modelling *local* radiometric effects.

In the global radiometric effects, we seek to capture and model illumination-sources affecting our scene. This is effectively done through the use of high dynamic range environment maps, under the assumption that the lights can in fact be modelled as being infinitely far away.

In the following subsections we describe the details concerning capturing and modelling environment maps.

1 Global Effects: Environment Map

To model global lighting effects we utilize the method of Debevec et al. [1] to capture a floating point precision spherical image of the surrounding scene. By assuming all elements captured in this spherical image are infinitely distant, all pixels composing the image may be treated as distant light sources allowing faithful environment lighting of local geometry. Here, we denote this image as an "environment map" and in fig 1 an example of such a map is shown. We employ the latitude-longitude panoramic format proposed by Reinhard et al. [3]

There are different approaches to capturing a spherical image of the surrounding scene using e.g. mirror spheres, stitching multiple images together, or panoramic

Figure 1: A $360° \times 180°$ image of the scene surroundings. We denote this an "environment map"

Figure 2: Mirror probe placed in scene for environment capture

cameras. Here, we utilize a highly polished bearing as a mirror sphere probe. In fig 2 a sample image of a scene with our probe is shown. By knowing the position of the camera and the fact that it is a sphere being observed, every pixel in the environment map has a unique location on the probe image, with the exception of the singularity directly behind the mirror probe. We will now describe the details in doing this probe unwrapping. For simplicity we assume an orthographic projection, i.e. assuming parallel view directions for all pixels of the sphere, but the extension to a perspective projection is trivial and only requires additional knowledge of the camera Field of View and distance to probe.

Let $Env(\phi, \theta)$ be the environment map (fig. 3, right) where $\phi \in [-\pi, \pi]$ is the azimuthal angle and $\theta \in [0, \pi]$ is the inclination. Furthermore, let $Probe(x, y)$ be the cropped probe image (fig. 3, center), where $x, y \in [0, 1]$. For a given resolution of ϕ and θ we wish to go through all locations in the environment map and lookup the corresponding intensity in the probe image. As with almost any image re-sampling, to ensure a smooth result with no holes or discontinuities, it is important that the mapping is done from the end-result's (environment map's) point of view, and not from the source's.

We define our coordinate system such that the direction to the camera is aligned with the x-axis (fig. 3, left), i.e. $V = [1, 0, 0]^T$. For a given location in the

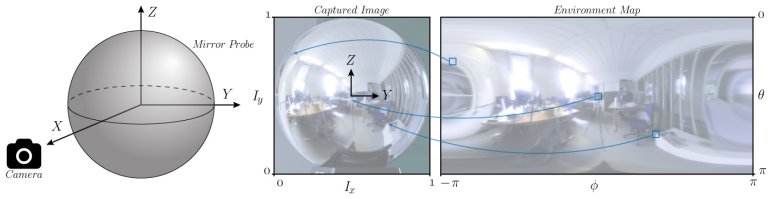

Figure 3: Unwrapping of spherical probe. The camera is assumed distant and aligned with the x-axis (left), such that an orthogonal projection of the XY-plane is observed (center). Every pixel/location in the environment map (right) thus has a unique location in the probe image, with the exception of the singularity precisely behind the sphere.

environment map, (ϕ_s, θ_s), the direction vector to this pixel, or light-source, is:

$$L = \begin{bmatrix} cos(\phi_s)\ sin(\theta_s) \\ sin(\phi_s)\ sin(\theta_s) \\ \cos(\theta_s) \end{bmatrix} \tag{1}$$

Now since we are dealing with perfect reflections, we know that at any point on the sphere probe, the view- and light-directions, L and V, are symmetrical around the surface normal, N. Hence, for sampling direction (ϕ_s, θ_s) in the environment map, the surface normal required to cause the reflection can be calculated as the normalized average of light and view:

$$N = \frac{L + V}{\|L + V\|} \tag{2}$$

Also here we see the singularity when $L = -V$. This is however of minor importance in practice.

Since the geometry being dealt with is a sphere, there is a unique location in the probe image (fig. 3, center) that holds the normal determined in eq. 2. By having the camera aligned with the x-axis of the world-coordinate system, the probe image will be aligned with the y/z-plane. The y- and z- components of N are thus directly related to the sampling position, (x_s, y_s), in the probe image:

$$\begin{bmatrix} x_s \\ y_s \end{bmatrix} = \begin{bmatrix} (N_y + 1)/2 \\ (N_z + 1)/2 \end{bmatrix} \tag{3}$$

Thus we get:

$$Env(\phi_s, \theta_s) = Probe(x_s, y_s) \tag{4}$$

Let us take a simple example, where we wish to lookup the environment map intensity at the direction $(\phi_s, \theta_s) = (0°, 90°)$, i.e. in the camera direction. Here, we see that:

$$L(0, \pi/2) = [1, 0, 0]^T \tag{5}$$

$$N = (L + V)/\|L + V\| = [1, 0, 0]^T \tag{6}$$

$$\begin{bmatrix} x_s \\ y_s \end{bmatrix} = \begin{bmatrix} (N_y + 1)/2 \\ (N_z + 1)/2 \end{bmatrix} = \begin{bmatrix} (0 + 1)/2 \\ (0 + 1)/2 \end{bmatrix} = \begin{bmatrix} (0.5 \\ 0.5 \end{bmatrix} \tag{7}$$

Correctly we get that the sampling location is located in the center of the captured probe image (fig. 3, center).

There may be scenarios where it is inconvenient to define the global coordinate system's x-axis as aligned with the camera direction. One example is if the camera was not level when capturing the probe image. This would cause a "wavy" horizon in the environment map, since the horizon at $\theta = \pi/2$ is misaligned with the true horizon. Another example could be if two images, taken from different angles, were to be merged to get rid of the before mentioned singularity.

In such cases we simply need to do a basis rotation before looking up values. Let $\tilde{V}$ be the *non*-x-axis-aligned direction to the camera and let $\tilde{L}$ be the light direction we wish to lookup. The normal in this non-aligned system, $\tilde{N}$ is again found through eq. 2. In order to be able to obtain sampling coordinates through eq. 3, $\tilde{N}$ needs to be realigned to the system where V aligns with this x-axis. This may be done by the rotation matrix, $\mathbf{R}$:

$$\begin{aligned} B_1 &= \tilde{V} \\ B_2 &= [0,0,1]^T \times B_1 \\ B_3 &= B_1 \times B_2 \\ \mathbf{R} &= [B_1\ B_2\ B_3]^T \end{aligned} \tag{8}$$

Hereby the aligned normal, N, is obtained through:

$$N = \mathbf{R}\tilde{N} = \mathbf{R}\left((\tilde{L} + \tilde{V})/\|\tilde{L} + \tilde{V}\|\right) \tag{9}$$

Allowing use of an arbitrary view direction, $\tilde{V}$.

The mapping operations presented above are highly parallelizable. In practice it is thus desirable to do these calculations on a GPU. In code sample 1, an OpenGL implementation using the GLSL shader language, shows how this mapping can be implemented on the graphics card. Using this approach, a 2K environment map is easily calculated in less than a second.

While we went into detail on how to unwrap a spherical probe image for use in rendering, we will omit the details on how to obtain high dynamic range images of the probes. Instead we refer the reader to Debevec and Malik's well written paper, "Recovering high dynamic range radiance maps from photographs" [2].

Code sample 1: GLSL fragment shader for sphere-unwrapping.

```
#version 330
#define M_PI 3.14159265
uniform vec2 uvSize;          //Size of environment map (width,height)
uniform vec2 probeImageSize;     //Size of probe image
uniform vec2 probeCenter;      //Center of probe in image
uniform float probeRadius;       //Radius of probe in image
uniform sampler2D probeIm;       //Texture containing probe image
uniform float thetaOffset = 0.0;  //Camera offset in spherical ↩
    coordinates
uniform float phiOffset = 0.0;

out vec4 FragColor;          //Output intensity

void main()
{
  vec2 pNorm = vec2(gl_FragCoord)/uvSize; //Normalized output pixel ↩
      coordinate
  float az = pNorm.x*2*M_PI;         //output azimuthal angle
  float inc = pNorm.y*M_PI;        //output inclination
  vec3 V = vec3(cos(phiOffset)*sin(M_PI/2+thetaOffset),
           sin(phiOffset)*sin(M_PI/2+thetaOffset),
           cos(M_PI/2+thetaOffset)); //View vector
  vec3 L = vec3(cos(az)*sin(inc),
           sin(az)*sin(inc),
           cos(inc));          //Light vector
  vec3 N = normalize(V+L);         //Surface normal

  //Create basischange matrix to align V with x-axis:
  vec3 B1 = V;
  vec3 B2 = cross(vec3(0,0,1),B1); //Assuming camera is horizontal
  vec3 B3 = cross(B1,B2);
  mat3x3 R = mat3x3(B1,B2,B3);
  vec3 Nr = transpose(R)*N;

  vec2 probeCoord = vec2(Nr.y,Nr.z);  //Normalized probe coordinate to↩
       lookup
  vec2 probeTexCoord = (probeCenter + probeCoord*probeRadius)/↩
      probeImageSize; //Texture coordinates
  FragColor = texture(probeIm,probeTexCoord); //sample value and ↩
      output
}
```

References

[1] Paul Debevec. Rendering synthetic objects into real scenes: Bridging traditional and image-based graphics with global illumination and high dynamic range photography. In *Proceedings of SIGGRAPH 98*, pages 189–198. ACM, 1998.

[2] Paul E. Debevec and Jitendra Malik. Recovering high dynamic range radiance maps from photographs. In *Proceedings of SIGGRAPH 97*, pages 369–378. ACM/Addison-Wesley, 1997.

[3] Erik Reinhard, Greg Ward, Sumanta Pattanaik, Paul Debevec, Wolfgang Heidrich, and Karol Myszkowski. *High Dynamic Range Imaging: Acquisition, Display and Image-Based Lighting*. Morgan Kaufmann/Elsevier, second edition, 2010.

Bibliography

[AAL16] Miika Aittala, Timo Aila, and Jaakko Lehtinen. Reflectance modeling by neural texture synthesis. *ACM Transactions on Graphics (Proceedings of SIGGRAPH 2016)*, 35(4):65, 2016.

[Aan03] Henrik Aanæs. *Methods for structure from motion*. PhD thesis, Technical University of Denmark, Department of Informatics and Mathematical Modeling, 2003.

[ACDC+15] Henrik Aanæs, Knut Conradsen, Alessandro Dal Corso, Anders Bjorholm Dahl, Alessio Del Bue, Mads Doest, Jeppe Revall Frisvad, Sebastian Hoppe Nesgaard Jensen, Jannik Boll Nielsen, and Jonathan Dyssel Stets. Our 3D vision data-sets in the making. In *The Future of Datasets in Vision 2015, CVPR 2015 Workshop*, 2015.

[ADSP12] H. Aanæs, A.L. Dahl, and K. Steenstrup Pedersen. Interesting interest points. *International Journal of Computer Vision*, 97:18–35, 2012.

[AMHH08] Tomas Akenine-Möller, Eric Haines, and Naty Hoffman. *Real-Time Rendering 3rd Edition*. A. K. Peters, Ltd., Natick, MA, USA, 2008.

[AP07] Michael Ashikhmin and Simon Premoze. Distribution-based BRDFs. *Unpublished Technical Report, University of Utah*, 2:6, 2007.

[APS00] Michael Ashikmin, Simon Premože, and Peter Shirley. A microfacet-based BRDF generator. In *Proceedings of SIGGRAPH 2000*, pages 65–74. ACM, 2000.

[AWL13] Miika Aittala, Tim Weyrich, and Jaakko Lehtinen. Practical SVBRDF capture in the frequency domain. *ACM Transactions on Graphics (Proceedings of SIGGRAPH 2013)*, 32(4):110, 2013.

[AWL15] Miika Aittala, Tim Weyrich, and Jaakko Lehtinen. Two-shot SVBRDF capture for stationary materials. *ACM Transactions on Graphics (Proceedings of SIGGRAPH 2015)*, 34(4):110, 2015.

[Bli77] James F Blinn. Models of light reflection for computer synthesized pictures. *Computer Graphics (Proceedings of SIGGRAPH 1977)*, 11(2):192–198, 1977.

[BLPW14] Adam Brady, Jason Lawrence, Pieter Peers, and Westley Weimer. genBRDF: Discovering new analytic BRDFs with genetic programming. *ACM Transactions on Graphics (Proceedings of SIGGRAPH 2014)*, 33(4):114, 2014.

[BS63] Petr Beckmann and Andre Spizzichino. The scattering of electromagnetic waves from rough surfaces. *International Series of Monographs on Electromagnetic Waves*, 4, 1963.

[BSH12] Mahdi M Bagher, Cyril Soler, and Nicolas Holzschuch. Accurate fitting of measured reflectances using a shifted gamma micro-facet distribution. *Computer Graphics Forum (Proceedings of EGSR 2012)*, 31(4):1509–1518, 2012.

[BSN16] Mahdi M. Bagher, John Snyder, and Derek Nowrouzezahrai. A non-parametric factor microfacet model for isotropic BRDFs. *ACM Transactions on Graphics*, 36(5), 2016.

[Bur12] Brent Burley. Physically based shading at Disney. In Stephen Hill and Stephen McAuley, editors, *Practical physically-based shading in film and game production*, ACM SIGGRAPH Courses. 2012. Article 10.

[CT82] Robert L Cook and Kenneth E. Torrance. A reflectance model for computer graphics. *ACM Transactions on Graphics*, 1(1):7–24, 1982.

[DCOS+15] Alessandro Dal Corso, Mikkel Damgaard Olsen, Kasper Hornbak Steenstrup, Jakob Wilm, Sebastian Jensen, Rasmus Reinhold Paulsen, Eythor Eiríksson, Jannik Boll Nielsen, Jeppe Revall Frisvad, Gudmundur Einarsson, and Hans Martin Kjer. Virtualtable:

a projection augmented reality game. In *SIGGRAPH Asia 2015 Posters*, page 40. ACM, 2015.

[Deb98] Paul Debevec. Rendering synthetic objects into real scenes: Bridging traditional and image-based graphics with global illumination and high dynamic range photography. In *Proceedings of SIGGRAPH 98*, pages 189–198. ACM, 1998.

[DVGNK99] Kristin J Dana, Bram Van Ginneken, Shree K Nayar, and Jan J Koenderink. Reflectance and texture of real-world surfaces. *ACM Transactions on Graphics*, 18(1):1–34, 1999.

[DW04] Kristin J. Dana and Jing Wang. Device for convenient measurement of spatially varying bidirectional reflectance. *Journal of the Optical Society of America A*, 21(1):1–12, 2004.

[EPA15] Eyþór Rúnar Eiríksson, David Bue Pedersen, and Henrik Aanaes. Predicting color output of additive manufactured parts. In *Proceedings of ASPE 2015 Spring Topical Meeting*, pages 95–99, 2015.

[FBLS07] Martin Fuchs, Volker Blanz, Hendrik P.A. Lensch, and Hans-Peter Seidel. Adaptive sampling of reflectance fields. *ACM Transactions on Graphics (Proceedings of SIGGRAPH 2007)*, 26(2):10, 2007.

[FCJ07] Jeppe Revall Frisvad, Niels Jørgen Christensen, and Henrik Wann Jensen. Computing the scattering properties of participating media using lorenz-mie theory. *ACM Transactions on Graphics (Proceedings of SIGGRAPH 2007)*, 26(3):60, 2007.

[FCJ12] Jeppe Revall Frisvad, Niels Jørgen Christensen, and Henrik Wann Jensen. Predicting the appearance of materials using lorenz–mie theory. In *The Mie Theory*, pages 101–133. Springer, 2012.

[FDA03] Roland W Fleming, Ron O Dror, and Edward H Adelson. Real-world illumination and the perception of surface reflectance properties. *Journal of Vision*, 3(5):3–3, 2003.

[FFG12] Adria Fores, James Ferwerda, and Jinwei Gu. Toward a perceptually based metric for BRDF modeling. In *Color and Imaging Conference*, volume 2012, pages 142–148. Society for Imaging Science and Technology, 2012.

[Foo97] Sing Choong Foo. A gonioreflectometer for measuring the bidirectional reflectance of material for use in illumination computation. Master's thesis, Cornell University, 1997.

[FV14] Jirí Filip and Radomír Vávra. Template-based sampling of anisotropic BRDFs. *Computer Graphics Forum (Proceedings of PG 2014)*, 33(7):91–99, 2014.

[GAHO07] Abhijeet Ghosh, Shruthi Achutha, Wolfgang Heidrich, and Matthew O'Toole. BRDF acquisition with basis illumination. In *Proceedings of ICCV 2007*, pages 1–8, 2007.

[GHP+08] Abhijeet Ghosh, Tim Hawkins, Pieter Peers, Sune Frederiksen, and Paul Debevec. Practical modeling and acquisition of layered facial reflectance. *ACM Transactions on Graphics (Proceedings of SIGGRAPH Asia 2008)*, 27(5):139, 2008.

[HDCD15] Eric Heitz, Jonathan Dupuy, Cyril Crassin, and Carsten Dachsbacher. The SGGX microflake distribution. *ACM Transactions on Graphics (Proceedings of SIGGRAPH 2015)*, 34(4):48, 2015.

[HF13] Michal Haindl and Jiri Filip. *Visual texture: Accurate material appearance measurement, representation and modeling.* Springer, 2013.

[HFM16] Vlastimil Havran, Jiri Filip, and Karol Myszkowski. Perceptually motivated BRDF comparison using single image. *Computer Graphics Forum (Proceedings of EGSR 2016)*, 35(4):1–12, 2016.

[HHA+10] Matthias B Hullin, Johannes Hanika, Boris Ajdin, Hans-Peter Seidel, Jan Kautz, and Hendrik Lensch. Acquisition and analysis of bispectral bidirectional reflectance and reradiation distribution functions. *ACM Transactions on Graphics (Proceedings of SIGGRAPH 2010)*, 29(4), 2010.

[Hot33] Harold Hotelling. Analysis of a complex of statistical variables into principal components. *Journal of educational psychology*, 24(6):417, 1933.

[HS03] Aaron Hertzmann and Steven M Seitz. Shape and materials by example: A photometric stereo approach. In *Proceedings of CVPR 2003*, volume 1, pages 533–540. IEEE, 2003.

[HTSG91] Xiao D He, Kenneth E Torrance, Francois X Sillion, and Donald P Greenberg. A comprehensive physical model for light reflection. *Computer Graphics (Proceedings of SIGGRAPH 91)*, 25(4):175–186, 1991.

[IRM+12] Ivo Ihrke, Ilya Reshetouski, Alkhazur Manakov, Art Tevs, Michael Wand, and Hans-Peter Seidel. A kaleidoscopic approach to surround geometry and reflectance acquisition. In *2012 IEEE Computer Society Conference on Computer Vision and Pattern Recognition Workshops*, pages 29–36. IEEE, 2012.

[JAM+10] Wenzel Jakob, Adam Arbree, Jonathan T Moon, Kavita Bala, and Steve Marschner. A radiative transfer framework for rendering materials with anisotropic structure. *ACM Transactions on Graphics (Proceedings of SIGGRAPH 2010)*, 29(4):53, 2010.

[JdJM14] Wenzel Jakob, Eugene d'Eon, Otto Jakob, and Steve Marschner. A comprehensive framework for rendering layered materials. *ACM Transactions on Graphics (Proceedings of SIGGRAPH 2014)*, 33(4):118, 2014.

[JM12] Wenzel Jakob and Steve Marschner. Manifold exploration: a markov chain monte carlo technique for rendering scenes with difficult specular transport. *ACM Transactions on Graphics (Proceedings of SIGGRAPH 2012)*, 31(4):58, 2012.

[JMLH01] Henrik Wann Jensen, Stephen R. Marschner, Marc Levoy, and Pat Hanrahan. A practical model for subsurface light transport. In *Proceedings of SIGGRAPH 2001*, pages 511–518. ACM, 2001.

[JN16] Rasmus Ramsbøl Jensen and Jannik Boll Nielsen. Atomic stretch: Optimally bounded real-time stretching and beyond. In *SIGGRAPH Asia 2016 Posters*. ACM, 2016. To appear.

[JNLP15] Rasmus Ramsbøl Jensen, Jannik Boll Nielsen, Rasmus Larsen, and Rasmus Paulsen. Anatomically correct surface recovery: A statistical approach. In *Scandinavian Conference on Image Analysis*, pages 212–223. Springer International Publishing, 2015.

[Kaj86] James T Kajiya. The rendering equation. *Computer Graphics (Proceedings of SIGGRAPH 86)*, 20(4):143–150, 1986.

[KM99] Jan Kautz and Michael D McCool. Interactive rendering with arbitrary BRDFs using separable approximations. In *Rendering Techniques' 99*, pages 247–260. Springer, 1999.

[Lew94] Robert R Lewis. Making shaders more physically plausible. *Computer Graphics Forum*, 13(2):109–120, 1994.

[LF97] Paul Lalonde and Alain Fournier. A wavelet representation of reflectance functions. *IEEE Transactions on Visualization and Computer Graphics*, 3(4):329–336, 1997.

[LFTG97] E Lafortune, S Foo, K Torrance, and D Greenberg. Non-Linear Approximation of Reflectance Functions. In *Proceedings of SIGGRAPH 97*, pages 117–126. ACM, 1997.

[LKYU12] Joakim Löw, Joel Kronander, Anders Ynnerman, and Jonas Unger. BRDF models for accurate and efficient rendering of glossy surfaces. *ACM Transactions on Graphics*, 31(1):9, 2012.

[LLSpS03] Hendrik P. A. Lensch, Jochen Lang, Asla M. Sá, and Hans peter Seidel. Planned sampling of spatially varying BRDFs. *Computer Graphics Forum*, 22(3):473–482, 2003.

[MAA01] Michael D McCool, Jason Ang, and Anis Ahmad. Homomorphic factorization of BRDFs for high-performance rendering. In *Proceedings of SIGGRAPH 2001*, pages 171–178. ACM, 2001.

[MN+95] Jan R Magnus, Heinz Neudecker, et al. Matrix differential calculus with applications in statistics and econometrics. 1995.

[MPBM03a] Wojciech Matusik, Hanspeter Pfister, Matt Brand, and Leonard McMillan. A data-driven reflectance model. *ACM Transactions on Graphics (Proceedings of SIGGRAPH 2003)*, 22(3):759–769, 2003.

[MPBM03b] Wojciech Matusik, Hanspeter Pfister, Matthew Brand, and Leonard McMillan. Efficient isotropic BRDF measurement. In *Proceedings of EGSR 2003*, pages 241–247, 2003.

[MWL+00] S Marschner, S Westin, E Lafortune, K Torrance, and D Greenberg. Image-Based BRDF Measurement including Human Skin. In *Rendering Techniques '99*, pages 131–144, 2000.

[NDM05] Addy Ngan, Frédo Durand, and Wojciech Matusik. Experimental analysis of BRDF models. In *Proceedings of EGSR 2005*, pages 117–126, 2005.

[NEK+15] Jannik Boll Nielsen, Eythor Runar Eiriksson, Rasmus Lynbgy Kristensen, Jakob Wilm, Jeppe Revall Frisvad, Knut Conradsen, and Henrik Aanæs. Quality assurance based on descriptive and parsimonious appearance models. In *Proceedings of the Third Workshop on Material Appearance Modeling: Issues and Acquisition*, MAM '15, pages 21–24. Eurographics Association, 2015.

[NFCA14] Jannik Boll Nielsen, Jeppe Revall Frisvad, Knut Conradsen, and Henrik Aanæs. Addressing grazing angle reflections in Phong models. In *SIGGRAPH Asia 2014 Posters*, page 43. ACM, 2014.

[Nic63] Fred E Nicodemus. Radiance. *American Journal of Physics*, 31(5):368–377, 1963.

[Nic65] Fred E Nicodemus. Directional reflectance and emissivity of an opaque surface. *Applied optics*, 4(7):767–775, 1965.

[Nic77] Fred E Nicodemus, editor. *Self-Study Manual on Optical Radiation Measurements*. National Bureau of Standards, 1977.

[NJNL+13] Morten Nobel-Jørgensen, Jannik Boll Nielsen, Anders Boesen Lindbo Larsen, Mikkel Damgaard Olsen, Jeppe Revall Frisvad, and J Andreas Bærentzen. Pond of illusion: interacting through mixed reality. In *SIGGRAPH Asia 2013 Posters*, page 26. ACM, 2013.

[NJR15] Jannik Boll Nielsen, Henrik Wann Jensen, and Ravi Ramamoorthi. On optimal, minimal BRDF sampling for reflectance acquisition. *ACM Transactions on Graphics (Proceedings of SIGGRAPH Asia 2015)*, 34(6):186, 2015.

[NSKR13] Tobias Noll, Didier Stricker, Johannes Kohler, and Gerd Reis. A full-spherical device for simultaneous geometry and reflectance acquisition. In *Proceedings of Applications of Computer Vision*, WACV, pages 355–362. IEEE Computer Society, 2013.

[PEAH16] David Bue Pedersen, Eyþór Rúnar Eiríksson, Henrik Aanæs, and Hans Nørgaard Hansen. In-situ monitoring in additive manufacturing using contact image sensors. In *Proceedings of the ASPE/EUSPEN 2016 Summer Topical Meeting on Dimensional Accuracy and Surface Finish in Additive Manufacturing*. ASPE – The American Society for Precision Engineering, 2016.

[Pho75] Bui Tuong Phong. Illumination for computer generated pictures. *Communications of the ACM*, 18(6):311–317, 1975.

[PR12] Thiago Pereira and Szymon Rusinkiewicz. Gamut mapping spatially varying reflectance with an improved BRDF similarity metric. *Computer Graphics Forum (Proceedings of EGSR 2012)*, 31(4):1557–1566, 2012.

[RH01] Ravi Ramamoorthi and Pat Hanrahan. A signal-processing framework for inverse rendering. In *Proceedings of SIGGRAPH 2001*, pages 117–128. ACM, 2001.

[Rus98] Szymon Rusinkiewicz. A new change of variables for efficient BRDF representation. In *Rendering Techniques '98*, pages 11–22, 1998.

[RVZ08] Fabiano Romeiro, Yuriy Vasilyev, and Todd Zickler. Passive reflectometry. In *European Conference on Computer Vision*, pages 859–872, 2008.

[RWP+95] Holly Rushmeier, Greg Ward, Christine Piatko, Phil Sanders, and Bert Rust. Comparing real and synthetic images: Some ideas about metrics. In *Rendering Techniques' 95*, pages 82–91. Springer, 1995.

[RWS+11] Peiran Ren, Jiaping Wang, John Snyder, Xin Tong, and Baining Guo. Pocket reflectometry. *ACM Transactions on Graphics (Proceedings of SIGGRAPH 2011)*, 30(4):45, 2011.

[RZ10] Fabiano Romeiro and Todd Zickler. Blind reflectometry. In *European Conference on Computer Vision*, pages 45–58. Springer, 2010.

[SAWG91] Françis X Sillion, James R Arvo, Stephen H Westin, and Donald P Greenberg. A global illumination solution for general reflectance distributions. *Computer Graphics (Proceedings of SIGGRAPH 91)*, 25(4):187–196, 1991.

[Sch94] Christophe Schlick. An inexpensive BRDF model for physically-based rendering. *Computer Graphics Forum*, 13(3):233–246, 1994.

[SCN+16] Jonathan Dyssel Stets, Alessandro Dal Corso, Jannik Boll Nielsen, Rasmus Ahrenkiel Lyngby, Sebastian Hoppe Nesgaard Jensen, Jakob Wilm, Mads Emil Brix Doest, Carsten Gundlach, Eythor Runar Eiriksson, Knut Conradsen, Anders Bjorholm Dahl, Jakob Andreas Bærentzen, Jeppe Revall Frisvad, and Henrik Aanæs. Digitizing scenes with glass objects. *Journal TBA*, 2016. Not yet published.

[SS95] Peter Schröder and Wim Sweldens. Spherical wavelets: Efficiently representing functions on the sphere. In *Proceedings of SIGGRAPH 95*, pages 161–172. ACM, 1995.

[SSW+14] Christopher Schwartz, Ralf Sarlette, Michael Weinmann, Martin Rump, and Reinhard Klein. Design and implementation of practical btf measurement devices focusing on the developments at the university of Bonn. *Sensors*, 14(5):7753–7819, 2014.

[TFG+13] Borom Tunwattanapong, Graham Fyffe, Paul Graham, Jay Busch, Xueming Yu, Abhijeet Ghosh, and Paul Debevec. Acquiring reflectance and shape from continuous spherical harmonic illumination. *ACM Transactions on Graphics (Proceedings of SIGGRAPH 2013)*, 32(4):109, 2013.

[TR75] TS Trowbridge and KP Reitz. Average irregularity representation of a rough surface for ray reflection. *Journal of the Optical Society of America*, 65(5):531–536, 1975.

[TS67] Kenneth E Torrance and Ephraim M Sparrow. Theory for off-specular reflection from roughened surfaces. *Journal of the Optical Society of America*, 57(9):1105–1112, 1967.

[War92] Gregory J Ward. Measuring and modeling anisotropic reflection. *Computer Graphics (Proceedings of SIGGRAPH 92)*, 26(2):265–272, 1992.

[WAT92] Stephen H Westin, James R Arvo, and Kenneth E Torrance. Predicting reflectance functions from complex surfaces. *SIGGRAPH Computer Graphics*, 26(2):255–264, 1992.

[WK15] Michael Weinmann and Reinhard Klein. Advances in geometry and reflectance acquisition. In *SIGGRAPH Asia 2015 Courses*. ACM, 2015.

[WLT04] Stephen H. Westin, Hongsong Li, and Kenneth E. Torrance. *A Field Guide to BRDF Models*. Cornell University, 2004. Manuscript.

[WMLT07] Bruce Walter, Stephen R Marschner, Hongsong Li, and Kenneth E Torrance. Microfacet models for refraction through rough surfaces. In *Proceedings of EGSR 2007*, pages 195–206. Eurographics Association, 2007.

[WMP+05] Tim Weyrich, Wojciech Matusik, Hanspeter Pfister, Jinho Lee, Addy Ngan, Henrik Wann Jensen, and Markus Gross. A measurement-based skin reflectance model for face rendering and editing. Technical Report TR2005-071, Mitsubishi Electric Research Laboratories (MERL), 2005.

[WSB+98] D White, Peter Saunders, Stuart J Bonsey, John van de Ven, and Hamish Edgar. Reflectometer for measuring the bidirectional reflectance of rough surfaces. *Applied optics*, 37(16):3450–3454, 1998.

[WW07] Andrea Weidlich and Alexander Wilkie. Arbitrarily layered microfacet surfaces. In *Proceedings of GRAPHITE 2007*, pages 171–178. ACM, 2007.

[WWZ16] Hongzhi Wu, Zhaotian Wang, and Kun Zhou. Simultaneous localization and appearance estimation with a consumer rgb-d camera. *IEEE Transactions on Visualization and Computer Graphics*, 22(8):2012–2023, Aug 2016.

[WZ15] Hongzhi Wu and Kun Zhou. Appfusion: Interactive appearance acquisition using a kinect sensor. *Computer Graphics Forum (Proceedings of PG 2015)*, 34(6):289–298, 2015.

[WZT+08] Jiaping Wang, Shuang Zhao, Xin Tong, John Snyder, and Baining Guo. Modeling anisotropic surface reflectance with example-based microfacet synthesis. *ACM Transactions on Graphics (Proceedings of SIGGRAPH 2008)*, 27(3):41, 2008.

[XNY+16] Zexiang Xu, Jannik Boll Nielsen, Jiyang Yu, Henrik Wann Jensen, and Ravi Ramamoorthi. Minimal BRDF sampling for two-shot near-field reflectance acquisition. *ACM Transactions on Graphics (Proceedings of SIGGRAPH Asia 2016)*, 35(6), 2016. To appear.